**Mid-infrared
E-ELT Imager and
Spectrograph**

METIS Science Case

E-REP-ETH-MET-1014
1
09-03-2019
Work package: SCI

	Signature and Approval		
	Name	Date	Signature
Prepared	Sascha P. Quanz, MST	09-03-2019	
Checked	MST	09-03-2019	
Approved	B. Brandl, F. Bettonvil	09-03-2019	
Released	F. Bettonvil	09-03-2019	

TABLE OF CONTENTS

LIST OF FIGURES

METIS

METIS

LIST OF TABLES

1   INTRODUCTION AND SCOPE OF THE DOCUMENT

The Mid-infrared ELT Imager and Spectrograph (METIS) covers the thermal/ mid-infrared wavelength range (3 - 19 μm) on the ELT. Focusing on highest angular resolution and high spectral resolution, METIS will provide outstanding observing capabilities, which are complementary to ALMA, MATISSE, JWST and the other ELT instruments. It is obvious that the ELT will open up new parameter spaces for optical/infrared astronomy and enable observations in the thermal/mid-IR range, which have never been possible before. While being a general-purpose science instruments serving a wide range of science cases (cf. Figure 1-1), METIS is expected to excel in particular in research related to circumstellar disks and extrasolar planets. These are the two science themes that mainly drive the science and technical requirements. In particular enabling state-of-the-art high-contrast exoplanet imaging in the L, M and N bands and the related requirements on the achievable contrast performance are technically challenging and led, to some extent, to an increase in instrument complexity that was not foreseen in Phase A. Still, as further detailed below, the scientific prospects of doing mid-infrared exoplanet science with a 39-m telescope more than justify the extra efforts - at least from a scientific perspective.
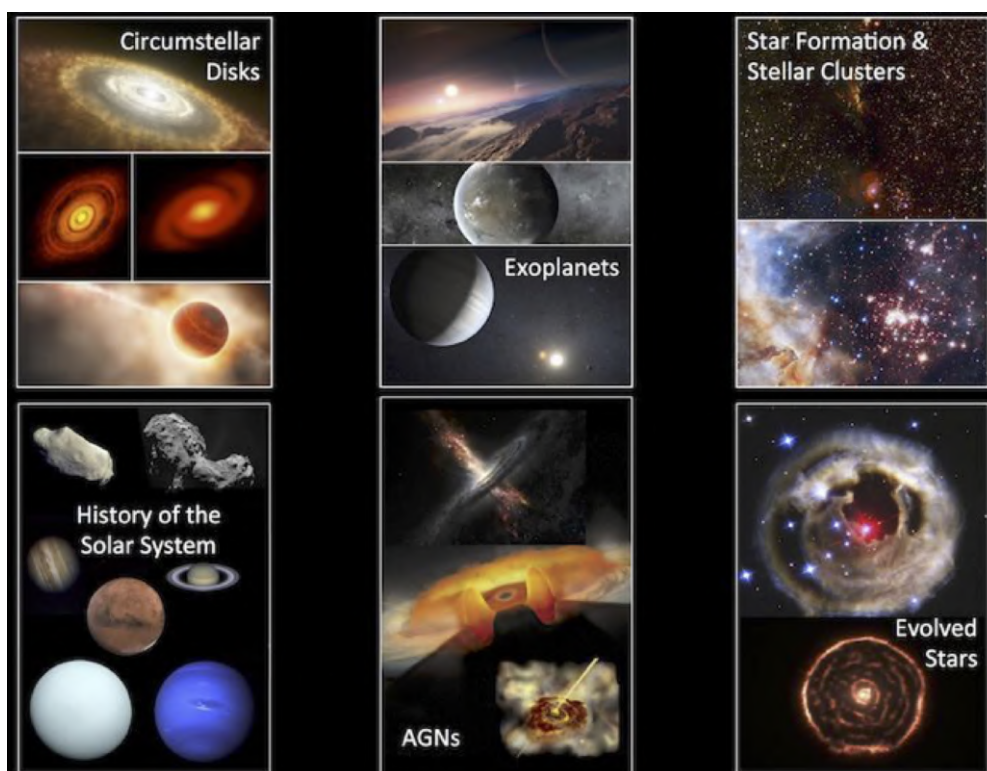
Figure 1-1: Overview of key areas of METIS science spanning from Solar System research over galactic sources to extragalactic targets. Circumstellar disks, i.e., the formation sites of planets, as well as exoplanet detection and characterization are the driving science themes.

METIS' unique contributions to astrophysics in the 2020s will likely be in science areas where high spatial or high spectral resolution, or a combination of both, is crucial. The METIS science case, as conceived around the time of PDR, covers the following science topics:

- Protoplanetary disks and the formation of planets

- Detection and characterization of exoplanets[1]

- The formation history of the Solar System

---

[1] Some of the science cases discussed for exoplanets are also applicable to Brown Dwarfs (as an extension towards more massive objects); hence, there is no dedicated section of Brown Dwarfs.

- Massive stars and cluster formation

- Evolved stars and their circumstellar environment

- The galactic center

- Physics of galaxies

- Active galactic nuclei

While not all science topics are likely to use all observing modes in equal amounts, prioritizing observing modes by expected scientific benefit is a non-trivial task in the case of METIS as it is exactly its versatility, coupled with the diffraction limited performance, that makes this instrument so powerful and attractive for science questions ranging from Solar System science to distant AGNs and galaxies. While powerful for bright targets, which certainly represent the majority of typical METIS targets, the brightness constraints for the guide stars of the SCAO system do represent a natural limit for METIS' discovery space. In particular Solar System science, massive stars and cluster formation as well as extragalactic science would benefit significantly from the addition of a laser-supported AO-system and increase the number of potential targets.

The objective of this document is to demonstrate both the unique capabilities of METIS in some science areas leading to breakthrough results and a significant advancement of the research field and – at the same time – the breadth of the science that METIS will be able to support covering a wide range of science topics. The instrument performance and capabilities on which the science cases described in the following sections are based, reflect the instruments baseline as conceived at PDR[2]. However, this document does not provide an overview of the technical specifications, the instrument baseline or the derivation of the science requirements for METIS and the reader is referred to other documents for these information. However, in Appendix A we provide for completeness an overview of METIS' observing modes.

---

[2]We note specifically that the baseline for the N-band detector is the Aquarius device and a laser-supported AO system is not part of the instrument baseline.

2 PROTOPLANETARY DISKS AND PLANET FORMATION

2.1 Scientific background and context

One of the most surprising findings in exoplanet research is the great diversity of exoplanetary systems, many of which bear little resemblance to our own Solar System. The Kepler satellite revealed at least 20% of Sun-like stars have Neptune-sized planets within 0.5 AU (Borucki et al. 2011a; Winn & Fabrycky 2015; Hatzes 2016), and many more planets are likely waiting to be discovered by operating and future missions (e.g., TESS, CHEOPS, JWST, PLATO, WFIRST). The implication of the exoplanet statstics is that essentially every disk around a young star must be forming planets. As our knowledge of exoplanetary properties expands, it becomes increasingly important to understand how planetary architectures depend on initial conditions by observing the evolution of protoplanetary disks.

The origin of the diversity of exoplanetary systems must lie in the structure and evolution of the disks out of which they form. The gas and solid components in these disks are inextricably connected and both are key players in the planet formation process. The gas controls the dynamics of dust particles and planetesimal growth, provides the main reservoir of material out of which giant planets form, and enables the migration of planets in the disk (both inwards and outwards) (Armitage 2011; Birnstiel et al. 2016). The solid component forms the basis for pebbles, planetesimals, large planetary cores – required for the formation of giant planets by core accretion (Johansen & Lambrechts 2017) – and rocky planets. Because condensable volatiles, such as water, contribute roughly half of the mass available for planetesimal formation, phase change, transport and concentration processes of ice/gas systems are an intricate part of planet formation (Ciesla & Cuzzi 2006; Hartmann et al. 2017). It is therefore critical to develop efficient observational tracers of both the solid and gaseous phases of protoplanetary disks on all scales from 1 to 100 AU.

Many of the planets detected to date are gaseous Jupiter-like planets, which are thought to form within 1-10 Myr after the formation of the parent star (Pollack et al. 1996; Dawson & Johnson 2018). In the core-accretion model, a few rocky cores with masses of 10-20 Earth masses must have formed quickly enough to attract gas to form a gas-rich planet. Over time – at most 20 Myr – the gas in the disk will dissipate and the small grains will coagulate or be blown away. This leads to the debris disk phase in which the disk is optically thin at UV and IR wavelengths and the grains are of secondary origin, replenished by collisions of larger objects: asteroid-sized bodies or planetesimals (Wyatt 2008; Hughes et al. 2018). In contrast with the giant planets, rocky planet embryos and planets with masses comparable to those of the Moon or Earth form by more gradual accretion of these planetesimals during the debris disk stage (Lissauer 1993; Morbidelli et al. 2012).

Gas-rich disks around Herbig Ae/Be stars (with ages of 1-5 Myr) are thought to be the immediate progenitors of the classical debris disks around A-type stars, like those around Vega (A0V, $\sim$100 Myr), β Pic (A5V, $\sim$20 Myr) or Fomalhaut (A3V, $\sim$100 Myr). But many more debris disks have now been detected thanks to Spitzer and Herschel, also around lower mass stars (Matthews et al. 2014). Moreover, transitional disks with large inner dust cavities, which may be the sites of currently forming giant planets, are found around stars from M to A type (van der Marel et al. 2018). The protoplanetary disk phase, the transition from gas-rich to gas-poor disks, and the debris disk phases are therefore key pivotal periods during which active planet-formation can be observed.

There are several recent lines of evidence that suggest that planet formation starts at even earlier stages than previously expected. This is demonstrated powerfully by the ALMA detection of gaps in the actively accreting Class I-II HL Tau disk (ALMA Partnership et al. 2015). Such gaps are now also detected in other young gas-rich protoplanetary systems (Fedele et al. 2018; Andrews et al. 2018) and they appear to be common. Further evidence of significant grain growth in an embedded Class I disk (Harsono et al. 2018) as well as the fact that only embedded Class 0 and I disks have enough solid material to build planetary systems with gas giant planets supports this view (Tychoniec et al. 2018; Manara et al. 2018).

A key science case for METIS is therefore to leverage the high spatial resolution of the ELT to observe,

and image, disk structures as well as the process of planet formation, in the primary planet-forming regions from 1–10 AU, at all evolutionary stages, from the embedded phase through the protoplanetary disk phase well into the debris disk phase. Specifically, METIS will have the potential to transform our understanding in five areas:

1. Observe the physical evolution of planet-forming material. This includes imaging the distribution of small grains (a few microns) for direct comparison with large grains (millimetre to centimetre) observed by ALMA, measuring the gas kinematics and amount of warm molecular gas down to 1 AU scales in disks, and quantifying molecular disk winds that affect disk evolution and dissipation.

2. Search for protoplanets embedded in gas-rich disks, either by direct imaging or through their kinematics reflecting dynamical interactions with gas and dust. This includes a search for molecular and atomic emission from circumplanetary disks around Jupiter-mass protoplanets. The physical properties of protoplanets can be directly compared to exoplanet demographics.

3. Measure the chemical composition of planet-forming gas and dust inside of 10 AU. This includes measuring the composition and distribution of warm molecular gas (organics, water) and PAHs in the innermost disk, observations of ices in scattered light and absorption, as well as the crystallinity and composition of small dust grains on 1-10 AU scales.

4. Image warm dust belts in nearby debris disks to determine their properties and radial distribution. This may reveal ongoing terrestrial planet formation and constrain models of the Earths origin.

5. Search for and image exozodiacal systems around nearby main-sequence stars to determine their demographics in comparison to those of exoplanets.

To achieve these objectives, METIS' unique combination of high spatial and spectral resolution will be crucial: a slice width of 18.3 milli-arcsec at 4.7 μm with the LMS corresponds to radii of around 1–2 AU in protoplanetary disks in the nearest star-forming regions (e.g., Ophiuchus, Chamaeleon or Lupus). The highest spectral resolution offered by METIS (R$\sim$100,000 in the L and M bands) matches the Keplerian velocity in a disk around a 0.3 M$_\odot$ star at 10 AU. The high spectral resolution is therefore needed to obtain kinematic information at the angular scales spatially resolved by the ELT 39 m aperture.

2.2   The physical structure and evolution of protoplanetary disks

2.2.1   Gas-dust dynamics and planet formation

METIS will image the thermal emission from micron-sized dust in protoplanetary disks, revealing inner holes and gaps, inner edges of dust walls as well as hot spots produced by local heating, all of which are diagnostics of the planet formation process (e.g., Liu et al. 2003). Recent scattered light studies at near-IR wavelengths tracing small sub-micron sized dust grains have begun to image the inner regions of disks (within 10–20 AU). With the advent of VLT-SPHERE, not only the brightest disks around A-type stars are probed but also the T Tauri star disks (e.g., Stolker et al. 2016; Avenhaus et al. 2018). These small grains may be present in regions where large mm-sized grains, imaged by ALMA, appear to be missing (Muto et al. 2012; Pinilla et al. 2018). This demonstrates that small dust particles, which are coupled to the gas, filtrate through the gap edge, while larger millimetre to centimetre-sized grains are trapped at larger radii (Garufi et al. 2013; Pinilla et al. 2016).

In addition to radial differences, azimuthal asymmetries of the small and large dust grains have been found. A spectacular example is the IRS 48 disk where the ALMA images reveal a strong azimuthal concentration of mm-sized dust (more than a 100-fold increase in surface density), while the VISIR 18 μm image shows a more complete ring of smaller dust grains (van der Marel et al. 2013) (Figure 2-1). Both radial and azimuthal asymmetries may be due to dust traps formed by the pressure-driven transport of solids in
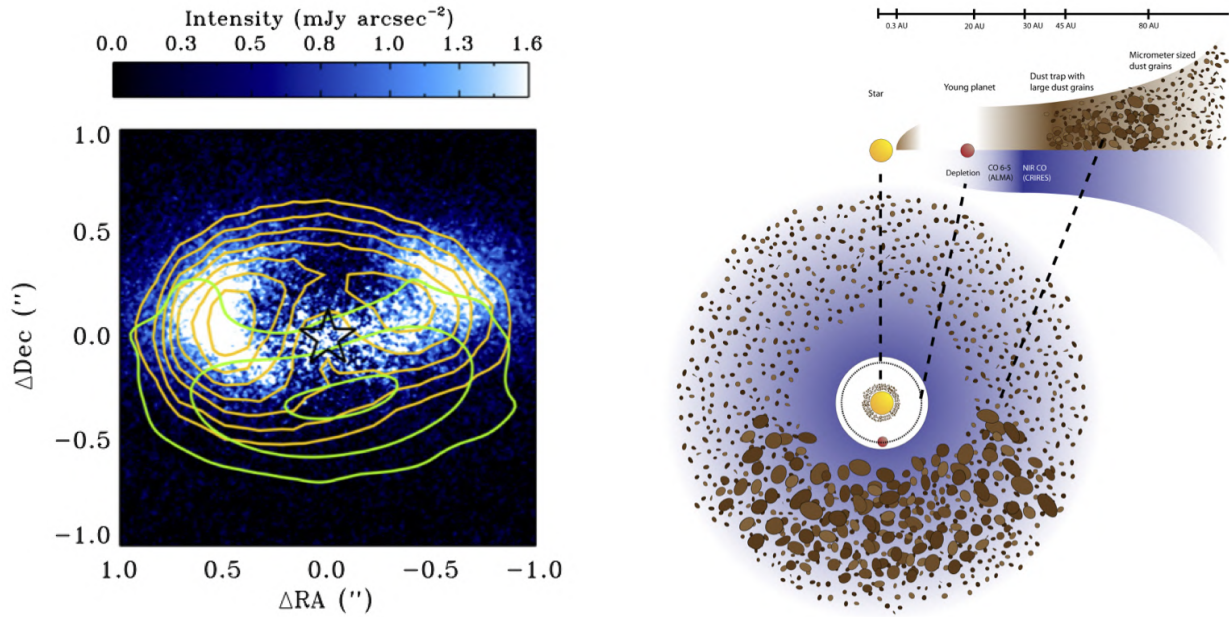
Figure 2-1: Left: VLT-VISIR image at 18 micron (orange) compared with ALMA 0.85 mm image (green) of the Oph IRS 48 transitional disk. The disk has an inclination of $\sim$50° and a $\sim$60 AU radius gap. The underlying image is of polarized light at near-infrared wavelengths (Follette et al. 2015). The mm-sized grains seen by ALMA are trapped on one side of the disk whereas the micron-sized grains are spread over the full ring. Such asymmetric dust traps can be caused by gas pressure bumps, likely induced by planets inside the disk (see cartoon on the right). For IRS 48, a 10-20 $M_{Jupiter}$ companion located at 20 AU has been suggested (van der Marel et al. 2013). METIS will open up such studies of a much larger sample of disks.

pressure maxima (Birnstiel et al. 2013). Within such dust traps, destructive collisions are diminished and small grains can grow rapidly to pebbles, rocks and planetesimals to form the seeds for the next generation of planets. However, while dust-trapping pressure-maxima may be induced by perturbing planets, they may also be the result of other processes such as zonal flows or pressure bumps at the edges of dead zones. It is the *combination* of images at near-infrared, mid-infrared and sub-millimeter wavelengths, mapping the relative spatial distribution of dust grains of different sizes, that is needed to distinguish between disk-sculpting mechanisms (Lyra & Klahr 2011; Rosotti et al. 2016; Pinilla & Youdin 2017).

Figure 2-2 shows simulated METIS N-band and ALMA 0.85 mm images of a disk with embedded planets of varying mass. The images result from a full hydrodynamic calculations, including a prescription for dust evolution and dynamics (de Juan Ovelar et al. 2013). As shown in this study, the separation between the micron- and mm-sized dust grains is very sensitive to the mass of the (unseen) embedded planet, and can be readily imaged by METIS for planets located at $\sim$5 AU or larger, the disk region where most giant planets are expected to form.

Similarly, the disk viscosity is a fundamental parameter governing many aspects of disk evolution, including the magnitude of local turbulence and dynamical time scales. Images of the location and sharpness of the gap wall at multiple wavelengths from near-IR to sub-mm constrain the viscosity by determining the efficiency with which dust grains of different sizes couple to the gas (Pinilla et al. 2012; Birnstiel et al. 2013; Mulders et al. 2013). METIS will have a spatial resolution of 50 mas at N-band, much higher than currently possible, and comparable to that achievable with sensitive ALMA continuum imaging. This opens the possibility of a strong ELT-ALMA synergy, with the combined data probing grains with sizes covering many orders of magnitude. Together with METIS and ALMA observations of the gas inside the dust gap (van der Marel et al. 2016), it will be possible to constrain most relevant physical parameters, including planet masses, disk viscosities, and even planet ages (Pinilla et al. 2015a). Many transitional disks with gaps located at $\sim$5 AU or larger are now known and will be accessible to combined METIS and ALMA studies.
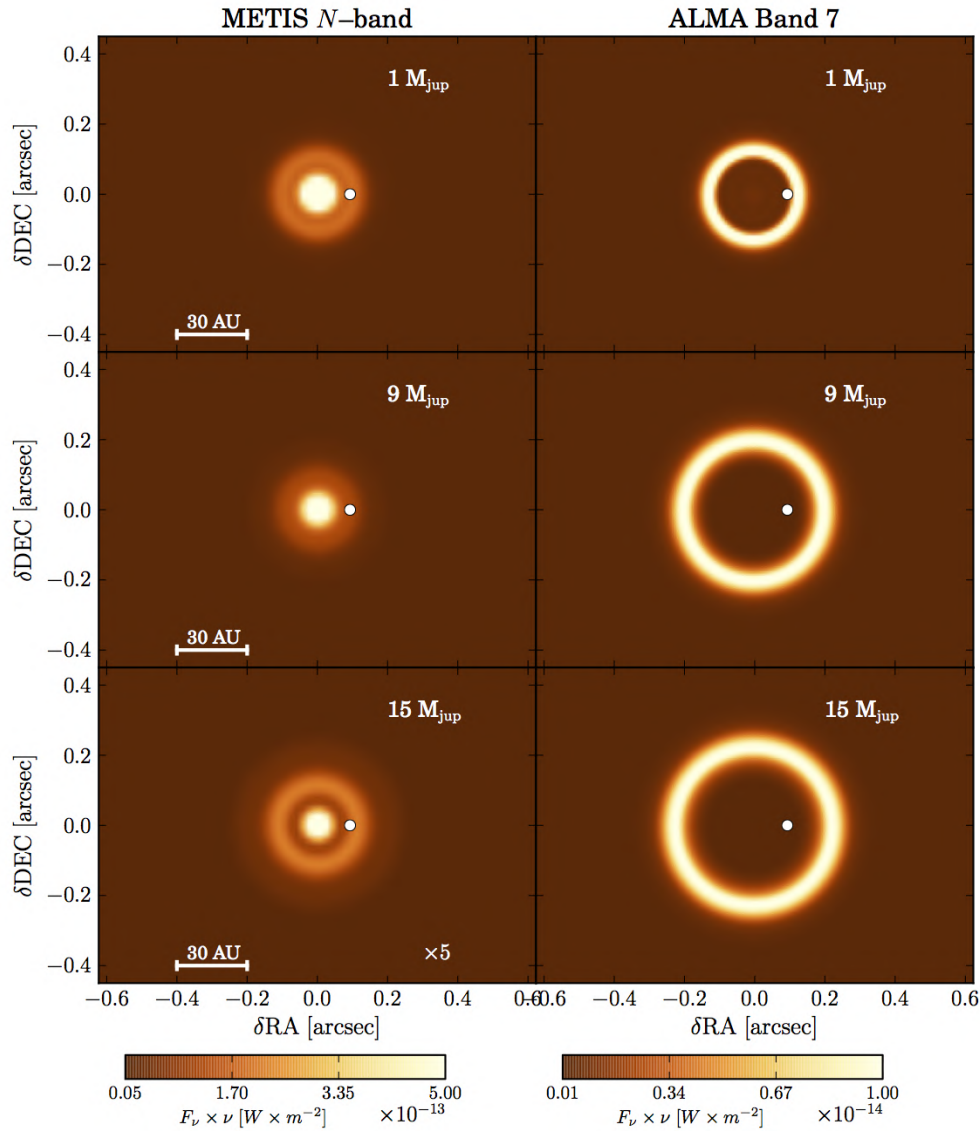
Figure 2-2: Simulated images of the disk-planet models for the case of an embedded planet orbiting at 13 AU (white dot) around a solar-mass star. The disk is assumed to be at a distance of 150 pc. Left and right columns correspond to METIS images at N-band and ALMA images at 0.85 mm, respectively. Top, middle and bottom rows show images obtained for planet masses 1, 9 and 15 M_{Jupiter}, respectively. The model images have been obtained following the procedure of de Juan Ovelar et al. (2013).

METIS may also detect structures carved by planets less massive than $\sim$1 M_{Jupiter}. Lower-mass planets will migrate in the disk without creating a deep gap. Figure 2-3 illustrates the capability of METIS to image planet-induced structures in a Herbig disk. Comparisons between the structures seen at mid-infrared wavelengths with METIS and at longer wavelengths with ALMA can put constraints on the mass of the perturbing planet.

2.2.2   Kinematic imaging of gas in planet-forming regions

While dust observations are critical for our understanding of planet formation, the gas component plays an equally important and complementary role. Gas not only drives dust dynamics, but also provides the necessary ingredient for giant planet formation. Moreover, the gas kinematics can probe a plethora of dynamical processes known to occur in disks such as : a) active accretion (viscous? disk wind driven?); b) active ejection (from the star? X-winds? or disk winds?) c) active planet-disk interaction (planet "weather":
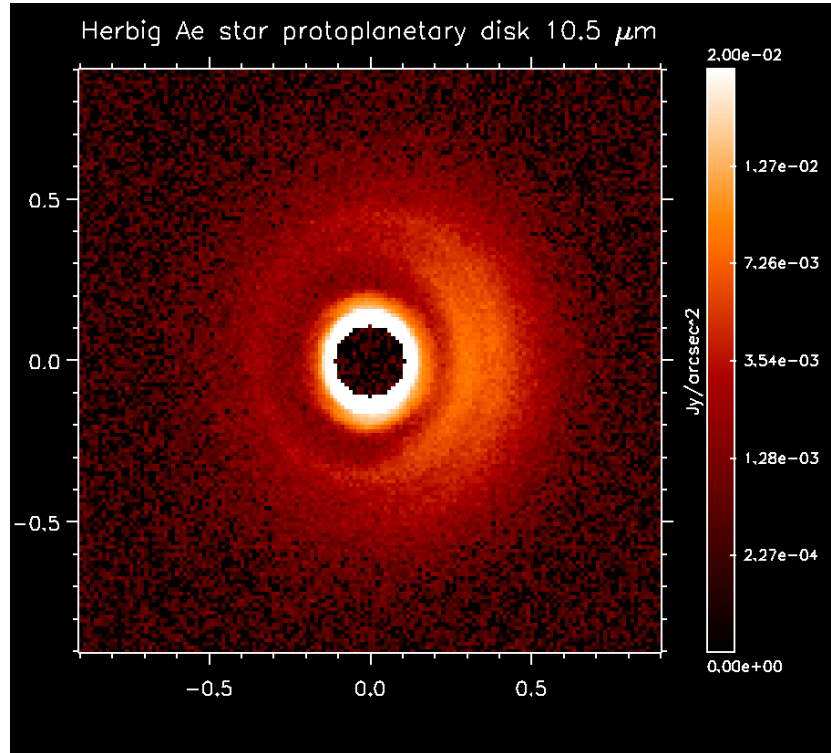
Figure 2-3: N band (10.5 μm) METIS simulated observation of a Herbig star protoplanetary disk at a distance of 140 pc. The structure of the disk has been computed using a SPH hydrodynamic code and assuming a giant planet (1 M_{Jup}) at a distance of 40 AU (Fouchet & Mayer 2008). The planet opens a gap and launches the observed spiral structures. The observing time is 1h on source and the high contrast imaging mode is assumed to be background limited beyond a radius of $2\lambda/D$.

accretion shocks? chromospheres?; disk perturbations (hydrodynamic? hydromagnetic? orbital?)) ; e) transient phenomena (variable accretion? local disk reorganization? variable irradiation?). METIS will allow probing these effects with roughly an order of magnitude larger angular resolution and two orders of magnitude larger SNR compared with the current state of the art. This critical combination of SNR and angular resolution is fundamental since emission in the line wings holds critical information, is faint and thought to originate in the innermost regions of the planet forming systems.

Gas is uniquely observable by METIS in the inner few AU, a region that ALMA cannot trace. On larger scales of a few 10s of AU, the power of spatially resolving molecular gas emission has already been demonstrated by ALMA. For instance, Casassus et al. (2013); Bruderer et al. (2014); Zhang et al. (2014); van der Marel et al. (2016) demonstrated the presence of gas inside the inner cavities of transition disks using spatially resolved line imaging, while Qi et al. (2013); Carney et al. (2017) imaged the CO snow line with molecular tracers, typically at 0.2–0.5″, resolution. In comparison to ALMA, METIS will produce full-aperture images of warm molecular gas in protoplanetary disks at angular scales of 0.05″, with high efficiency and sensitivity, allowing for direct imaging of large samples of disks. [3]

The most powerful tracer of this inner planet-forming disk region at 1–10 AU are the CO v=1-0 ro-vibrational transitions at 4.7 μm which trace gas at a few hundred K to about 1000 K (Najita et al. 2003; Blake & Boogert 2004a; Pontoppidan et al. 2008; Brown et al. 2013; Brittain et al. 2014). The transitions are excited by collisions, infrared pumping and by UV fluorescent excitation in environments where the UV field is strong (Thi et al. 2013). This leads to strong line emission from small disk radii within 1 AU, and lower, but significant, extended emission from several to 10s of AU, depending on the strength and hardness of the stellar spectrum.

The ro-vibrational CO lines trace the surface of the disk at early evolutionary stages during which the

---

[3]The ELT/METIS angular resolution is a factor 6-10× that of the JWST/NIRSPEC, precluding such studies with JWST.
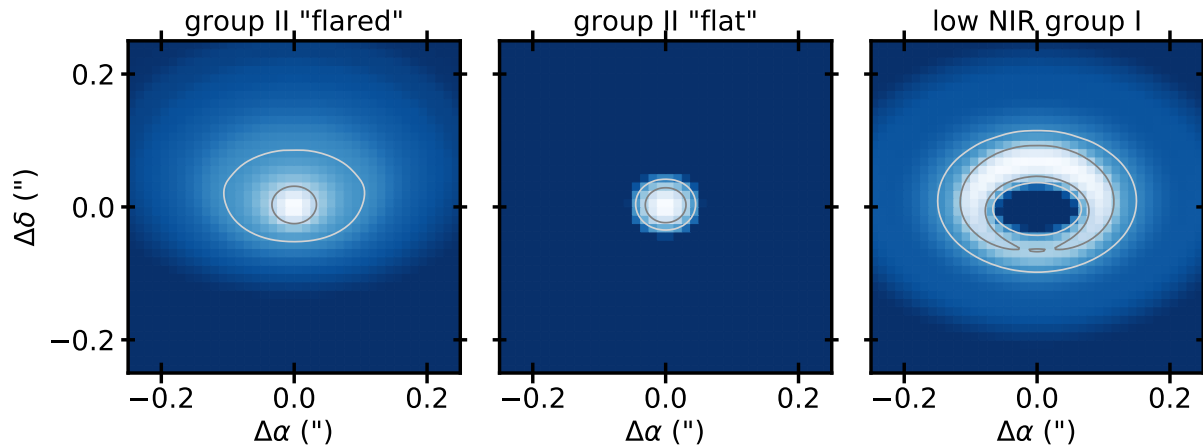
Figure 2-4: Simulated METIS CO spectral images for three proposed Herbig disk geometries. Normalised, continuum subtracted and velocity integrated maps of the CO v=1-0 P(10) line are presented. Flat and flared inner disks should be easily distinguished in a 1 hr integration based on these images and the holes inferred for the group I Herbig disks will be resolved in both line and continuum data. A logarithmic colour stretch is used, with the white and grey lines showing 1% and 10% of the peak flux. The model images have been convolved with a Gaussian with a 0.025 FWHM, representative of diffraction limited ELT-METIS observations. A distance of 150 parsec is assumed (from Bosman et al. 2019, subm.).

disk is optically thick in the vertical direction, but they may penetrate close to the mid-plane once the gas dissipates or is depleted by the dynamic action of a planet (Salyk et al. 2011). With current facilities, the infrared line emission has been spatially resolved in a number of disks using adaptive optics on scales of ∼10 AU, in particular those with partially cleared-out inner regions (Goto et al. 2006a; Brittain et al. 2009). With adaptive optics and the added use of spectro-astrometric techniques, CO gas has been partially imaged down to 0.1 AU scales for a few of the brightest sources (Pontoppidan et al. 2008, 2011a). Some sources show primarily Keplerian rotation of the gas, other disks have additional kinematical signatures superposed (Bast et al. 2011; Banzatti & Pontoppidan 2015). Figure 2-4 illustrates how METIS images can directly distinguish different models that have been proposed for the inner disk of Herbig stars with different spectral energy distributions. Overall, ro-vibrational CO is perhaps the best tracer of the structure, kinematics and dissipation of molecular gas in inner disks, and strong correlations are found between the properties of the CO emission and the presence of inner gaps (van der Plas et al. 2015; Banzatti et al. 2017).

In summary, it is well-known that CO ro-vibrational line emission from most disks exhibits extended and complex structures on 1–10 AU scales, but progress is limited by a lack of spatial resolution and sensitivity. The METIS integral field unit (IFU) will directly image the kinematics of protoplanetary disks with a spatial resolution 5-10 times better than that offered by current 8m telescopes or line imaging with ALMA. The CO emission extends over 2–32 spaxels with 8-10 m telescopes in favorable cases. The 4–5 times higher spatial resolution with the ELT will, in combination with higher surface brightness sensitivity, lead to spectrally resolved CO line cubes over as many as 82 spaxels or more (see, Figure 2-5). METIS will resolve moving gas structures as small as 2 AU in size at typical distances of 120 pc and as little as 1 AU for the closest disks, with spectro-astrometry providing even higher resolution. Furthermore, the high sensitivity of METIS will ensure that the entire variety of disks will be available to such studies, including faint disks around brown dwarfs and those in transition to the debris disk phase.

Optically thin ^{13}CO and C^{18}O isotopologues can be imaged as well, probing deeper into the disk. A large sample of at least a hundred protoplanetary disks across the stellar mass range, from brown dwarf disks to disks around young A-stars, can potentially be targeted. As stellar mass is thought to be a key variable in predictive models of disk evolution and planet formation (e.g., Mordasini 2018), observations across the mass spectrum will be a powerful discriminant between models of disk evolution and planet formation.

The high spectral resolution is essential to classify the observed spatial structures; is the emission coming

CO gas with METIS   **Dust continuum with ALMA**
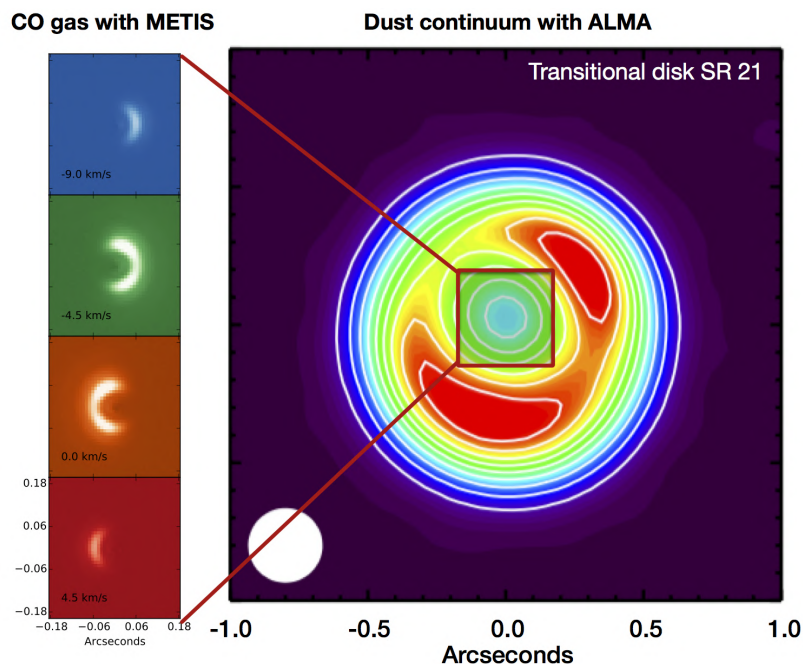
Figure 2-5: Model of a METIS observation of CO ro-vibrational emission at 4.7 μm in the transitional disk around SR 21 in Ophiuchus (left panels), compared to the ALMA dust continuum (0.88 mm) image (right panel) from Pinilla et al. (2015b). Note that it is already known from CRIRES spectroastrometry observations (Pontoppidan et al. 2008) that the CO gas traces an inner ring at ∼7 AU (corresponding to the orbits of Jupiter and Saturn in the Solar system), separate from the outer dust ring at ∼35 AU as seen with ALMA. METIS can now directly image this ring and provide further constraints on any embedded planets sheparding the rings. The CO images represent a two-dimensional non-LTE model with gas/dust thermal decoupling using RADLite/RADMC.

from gas in Keplerian motion, or does it trace an outflow process (see below)? If a localized "hot spot" is detected, is that related to the presence of a compact object, or is it just a disk density or temperature enhancement? High spectral resolution also ensures that the maximum line sensitivity is reached in all cases and that telluric features can be well removed. For instance, the CO lines from the face-on TW Hya disk are 7 km/s wide, and therefore only resolved at R>50,000. R=100,000 probes radii of 1–10 AU for a Keplerian disk around a Solar-type star, matching the METIS imaging regime.

2.2.3 Disk winds

The upper layers of the disks traced by METIS gas observations provide the connection between the underlying Keplerian disks and the surrounding radial flows, including various types of disk winds (evaporative and magnetically driven centrifugal). Currently, such flows are thought to be observed in CO ro-vibrational lines, but not yet understood (Pontoppidan et al. 2011a; Salyk et al. 2014), including how they are linked with the [Ne II] 12.8 μm or [O I] 6300 Å kinematic signatures (Alexander et al. 2014; Banzatti et al. 2019). By directly imaging the flows and their extent in CO (and other species), METIS will allow mass loss rates to be quantified and is therefore likely to dramatically enhance our understanding of disk dissipation and the timescale available to form gas-rich planets.

Take as an example the case of HL Tau. This source drives a collimated jet (e.g., Movsessian et al. 2012). It is currently accepted that jet engines are magnetically mediated and originate from the star-disk interaction region or the disk itself (now seen by ALMA), a region that METIS can probe. Direct evidence of a molecular disk wind is found with ALMA towards the Class I source TMC1A, launched from radii out to 25 AU (Bjerkeli et al. 2016). The current state of the art models address jet engines via simulations in the non-ideal MHD regime present in the weakly ionized gas (e.g., Béthune et al. 2017; Yvart et al. 2016). It is found that multiple states (e.g., with disk accretion, disk ejection, non-accreting, non-ejection, one disk side

only ejection, transient effects) can be present, some of them in the same disk. Because magnetic effects are known to alter disk structure, they directly impact of planet formation.

Evidence of strong disk winds and/or outflows has already been seen in spatially unresolved VLT-CRIRES CO 4.7 μm spectra of a dozen embedded protostars (Herczeg et al. 2011). The model predictions have spatial signatures on 1–30 AU scales that can be directly probed by METIS: a) a wind onion-like structure with lower excitation emission originating further out; b) centroid offsets of the molecular emission from the continuum; c) spatial resolved rotation detected in the molecular emission outflowing from the disk. This is one science case that would greatly benefit from a single laser AO by opening up many more embedded sources for study.

2.3   Signatures of protoplanets

The unique combination of high spectral and spatial resolution offered by METIS allows spectro-imaging of the distribution of material on AU scales. One of the most exciting prospects, given this capability, is the detection, imaging and kinematic characterization of warm dust and gas directly sculpted by the presence of still-forming Jupiter-mass planets. This may be accomplished in at least four different ways:

1. Thermal continuum emission from warm protoplanets and their circumplanetary disks (CPDs) may be detected using high contrast imaging.

2. Unseen planets may be detected using spatio-kinematic departures from Keplerian motion, including infall of gas toward the planet from the protoplanetary disk.

3. Detected accreting giant planets may be confirmed and characterized by measuring the Keplerian motion in the circumplanetary disk using CO ro-vibrational lines.

4. Dust imaging, in combination with ALMA, as a function of dust grain size to search for indirect evidence of dynamical sculpting by newly formed planets and dust gaps (Section 2.2.1, Fig. 2-2 and 2-3).

2.3.1   Continuum detections of forming protoplanets

Circumplanetary disks surround giant planets during the protoplanetary disk phase. For instance, it is likely that a Jovian circumplanetary disk was responsible for the formation of the Galilean moons (Canup & Ward 2002; Mosqueira & Estrada 2003). The local Hill sphere of the giant planet sets the radius of a circumplanetary disk ($R_{\mathrm{CPD}} \sim 0.3 - 0.5\ R_{\mathrm{Hill}}$), which can be as large as a few AU beyond 10 AU (e.g., Ayliffe & Bate 2009), and local heating is the primary excitation for disk emission.

Depending on the, as yet poorly known, properties of protoplanets, METIS may be able to detect them in thermal emission (in contrast to local colder material in the circumstellar disk). Based on high-contrast imaging techniques several candidates for still-embedded young protoplanets were published in recent years including LkCa 15 b, HD100546 b, HD169142 b, and MWC758 b (e.g., Kraus & Ireland 2012; Quanz et al. 2013, 2015a; Reggiani et al. 2014, 2018). However, in most cases follow-up observations cast some doubts on the true nature of the detected signals (e.g., Thalmann et al. 2016; Rameau et al. 2017; Huélamo et al. 2018; Cugno et al. 2019). In addition, in many other circumstellar disks with prominent morphological or kinematic structures different groups searched for embedded planets (e.g., HL Tau, HD163296 (see also below); Testi et al. 2015; Guidi et al. 2018), but without success. At the moment the most promising candidate for a young planet orbiting within the disk gap of its host star is PDS70 b (see, Figure 2-6; Keppler et al. 2018; Müller et al. 2018).

METIS' high sensitivity and spatial resolution will allow us to probe much deeper and much closer to the star than currently possible. This is important as theory would form planets closer in more rapidly than further out - if the orbital timescale is driving the planet accretion timescale - so we expect many more
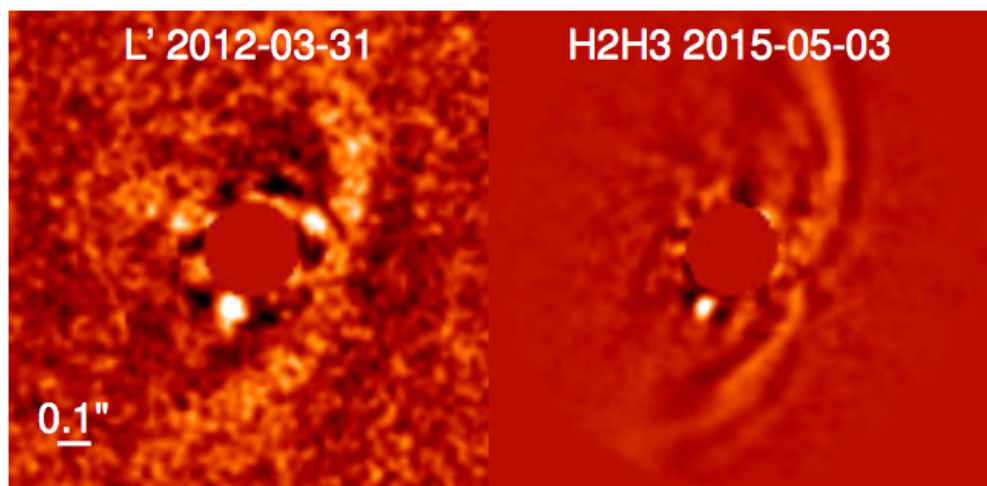
Figure 2-6: PDS70 b as seen in the L′ band with Gemini/NICI (left) and in the H band with VLT/SPHERE (right) (Keppler et al. 2018). The separation from the central star (which is located in the center and masked out in these images) is ∼22 AU. In particular in the H band image some scattered light from the circumstellar disk is seen on the right hand side.

candidates closer in than further out. Thus, METIS will allow for (a) a much more robust assessment of the true nature of the known objects and (b) search for additional objects in particular located within the gaps of transition disks (see also, Figure 2-7). Constraining the luminosity and temperature could place powerful constraints on models of gas giant planet formation. Indeed objects, at orbital separations >10 AU, present challenges to standard formation scenarios. METIS will provide a resolution that enables the detection of objects within 3 AU compared to current limits at >15 AU (for a distance of 100 pc) probing the physical scales where the bulk of the giant planets in our own solar system are thought to have formed.

In addition to significant uncertainties regarding the luminosity of young, forming gas giant planets, also the properties of the suspected CPDs are largely empirically unconstrained. While some analytical models for CPDs suggest that these objects should be particularly bright at wavelengths >3 μm (Eisner 2015; Zhu 2015), the complex 3D morphology of the gas flow onto and around the CPD suggest that more elaborate models are needed to make predictions for the expected MIR SEDs (Szulagyi et al. (subm.)). It is clear, however, that a large wavelength coverage will be essential to disentangle the flux contribution from the young planet from that of the CPD. METIS with its spectroscopic capabilities in the L, M and N band will play a key role here and help constraining the luminosity, and hence temperature and size, of CPDs.

2.3.2 Kinematic detections of planets

Continuum or narrow-band detections of protoplanet candidates with METIS are likely to lead to exciting discoveries. However, to fully confirm and characterize protoplanets, spectroscopy is needed. Specifically, attributes such as the planet mass, accretion properties, chemistry and other interactions with any circumplanetary disk may be reachable with spectro-imaging in the 3–5 μm regime.

The kinematic action of an embedded giant planet will not only clear gaps in the protoplanetary disk, but will also perturb the Keplerian motion of disk gas by inducing eccentric gas orbits (Regály et al. 2010), as well as local perturbations near the planet, by as much as 1-2 km/s across a few AU region (Perez et al. 2015). Recently, ALMA detected the kinematic signature of protoplanet candidates in the disk around HD 163296 through CO sub-mm channel maps, which are consistent with perturbations by Jupiter mass planets at ≈ 83, 137 and 260 AU (Pinte et al. 2018; Teague et al. 2018). The METIS wavelength range allows to access the inner disk (warm CO gas inside 30 AU) and is thus highly complementary to ALMA.

The detection of such kinematic signatures may not only confirm the presence of a compact object in a "hot spot" detected by METIS in 10 μm continuum imaging, but will also measure its mass. Detecting and measuring the masses of protoplanets while they are forming will provide a transformative comparison to
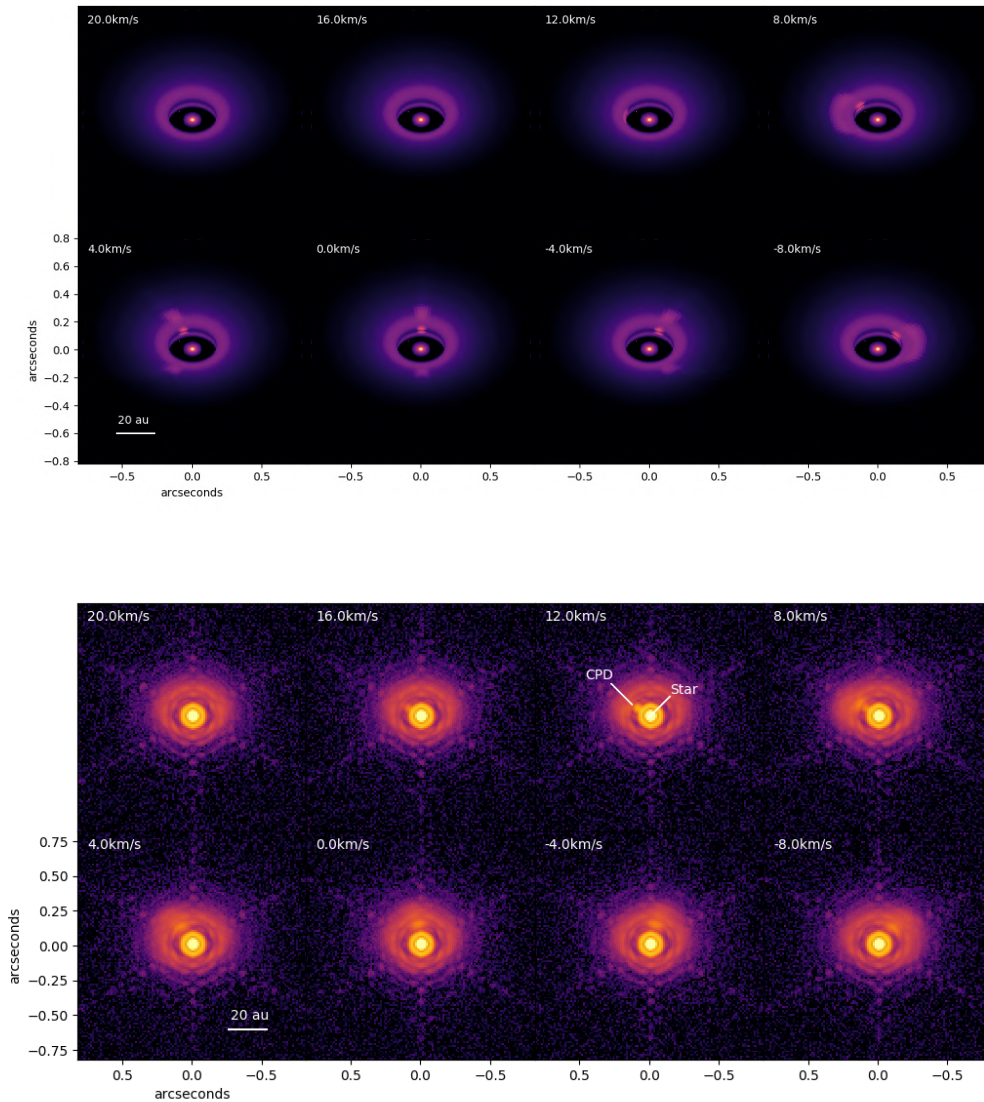
Figure 2-7: Top: Synthetic channel map of CO v(1-0)P08 emission at 4.7 μm in the HD100546 system (PPD disk model from Hein Bertelsen et al. 2014) detailing the 4-13 au annular gap and an embedded planet candidate. The star has mass $M_\star = 2.4 M_\odot$ and luminosity $L_\star = 27 L_\odot$. The planet candidate HD100546 c (Brittain et al. 2013, 2014) here has an assumed mass $M_p = 5\ M_J$, temperature $T_{\rm eff}$ = 1000K, and luminosity $3.7 \times 10^{-5} L_\odot$. The planet orbit has $a = 12$ au, $i = 42°$. The CPD has a mass of $5 \times 10^{-2} M_J$ and a dust-to-gas ratio of 0.01. It has an inner radius of 0.004 au, and tapers off beyond 0.36 au to an outer radius of 0.38 au. The circumplanetary disk line FWHM is 4.5 km/s and at the specified orbital phase the planet has a radial velocity of 10 km/s. Bottom: The same model as above, but now run through the METIS LMS simulator (10 exposures, each 360 s). The signature of the CPD can be clearly detected.

mature exoplanetary systems. Furthermore, the orbital parameter space covered by METIS will match that relevant for giant planets in solar system analogs.

2.3.3   Kinematic signatures of circumplanetary disks

Circumplanetary disks are key for the formation of gas giant planets and their potential moon systems. To test various proposed formation scenarios (Canup & Ward 2009; Szulágyi et al. 2014) the gas kinematic signatures in the vicinity of forming protoplanets need to be measured (see also, Section 2.3.2). METIS may also be able to detect warm CO gas in local Keplerian motion in a circumplanetary disk. Such a

scenario is modeled in Figure 2-7 for a 5 Jupiter mass planet in a transitional disk around a Herbig star. A key property of the gas signature from a circumplanetary disk in such a gap is that it will be offset from the local disk velocity by up to 5–10 km/s due to the planets own motion around the star, thus avoiding interference from ambient disk gas.

Detections of circumplanetary disks in near-Keplerian rotation may also provide the first evidence for the origin of pro-grade moon systems in disks, such as that of the Jovian system. As the physics of circumplanetary disk accretion may be crucial in limiting planet masses (Morbidelli et al. 2014; Lee & Chiang 2015), these studies are of fundamental importance for constraining models of planet formation.

2.4   The chemical composition and evolution of planet-forming material

2.4.1   Water and organics in the innermost disk

In addition to providing direct clues concerning the formation of gas giant planets, molecular studies of gas-rich disks can be used to constrain the potential composition of such objects. The bulk chemistry of inner protoplanetary disks - the primary carriers of carbon, oxygen and nitrogen drive the structure and composition of planets (e.g., Madhusudhan et al. 2014). METIS can therefore link the properties of exoplanets to those of disks, by observing a wide range of abundant gas-phase molecules that are detectable using high resolution spectroscopy, like NH_3, HCN and CH_4, as well as water and OH, in the 3–5 μm region (Mandell et al. 2012; Banzatti et al. 2017, Figure 2-8). Most of these key molecules are not observable by ALMA, which is in any case limited to probing volatiles at > 5 AU (e.g., Bruderer et al. 2015).
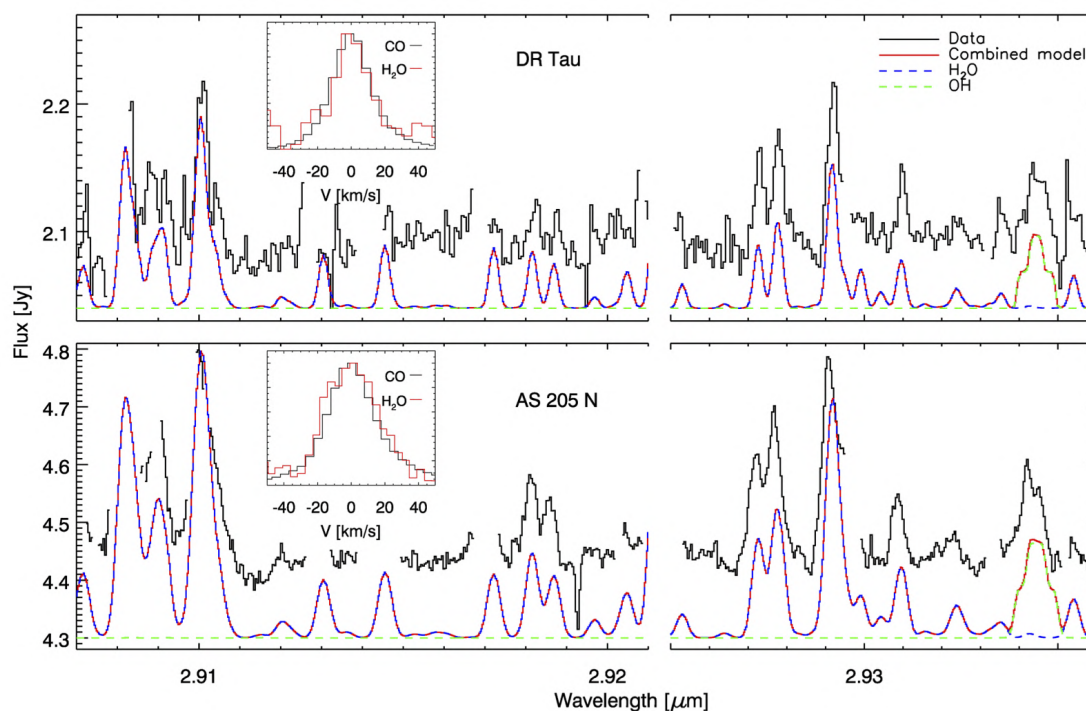
Figure 2-8: Keck-NIRSPEC R=25,000 L-band observations of vibration-rotation lines of H2O and OH in two proto-planetary disks (Salyk et al. 2008). The inserts indicate the similarity in CO and H2O line profiles. These lines arise from the hot inner disk (within ~1 AU); lines further out in the disk will be significantly narrower.

The high sensitivity of METIS can reach disks across the stellar mass-spectrum, down to young brown dwarfs. This is of particular importance, since inner disk chemistry is known to be a strong function of stellar type. Indeed, disks around Herbig Ae stars have an apparently poor chemistry (Pontoppidan et al. 2010; Fedele et al. 2012), while those around solar type stars are rich in both water and organics (Salyk et al. 2011) and brown dwarf disks are rich in organics, but poor in water (Pascucci & Sterzik 2009; Pascucci

et al. 2013). Spectrally resolving the line profiles in the inner disk allows us to determine whether lines from different molecular species are tracing the same gas or entirely different disk regions. This is critical for completing molecular budgets as a function of disk radius. As an example, Banzatti et al. (2017) used high resolution VLT-CRIRES spectra of OH and H_2O at 2.9 μm to infer an inside-out depletion of water within the water snow line during disk dispersal. Thus, METIS spectroscopy is expected to be highly complementary to the lower resolution spectroscopy offered by JWST, which probes the slightly cooler and deeper parts of the disk at mid-infrared wavelenghs but lacks the kinematic and spatial information to determine the molecule's location (Antonellini et al. 2015; Bosman et al. 2017; Woitke et al. 2018). Together, they may probe overall C/O and C/N elemental abundance ratios in the gas as function of disk radius across major snow lines (Pontoppidan et al. 2014). The ultimate goal is to link the composition of mature exoplanets to their formation sites in their natal protoplanetary disks (e.g., Öberg et al. 2011; Helling et al. 2014; Mordasini et al. 2016; Booth et al. 2017; Cridland et al. 2019).

2.4.2   Imaging of the water ice distribution in disks

The combination of high spatial resolution and high sensitivity makes METIS a unique tool for imaging certain important solid species in the surfaces of protoplanetary disks. One such species is water ice - a dominant solid mass carrier beyond the snow line, thought to be critical for driving the efficient formation of planetesimals. Consequently, measuring the distribution of water in disks is currently a highly active area of research, but one that is nearly entirely focused on the vapor phase (Hogerheijde et al. 2011; Du et al. 2017; Banzatti et al. 2017, and see above). It is only possible to observe water ice in *emission* in the far-infrared. This was done both by ISO (Malfait et al. 1998) and Herschel (McClure et al. 2015; Min et al. 2016). However, current-technology far-infrared spectral imaging does not resolve protoplanetary disks and there is no approved future far-infrared space mission yet.
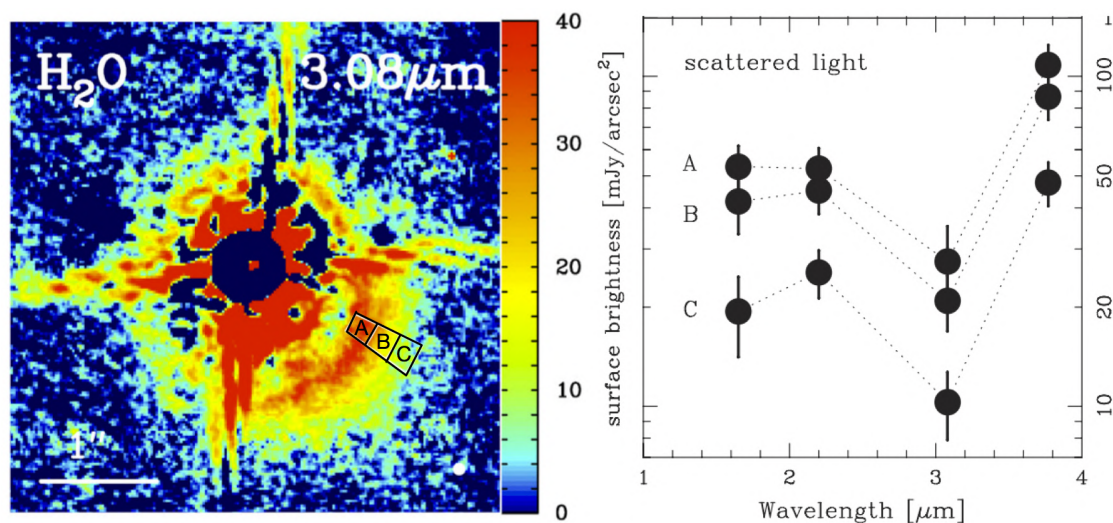
Figure 2-9: Narrow-band scattered light observation investigating the water ice band at 3.08μm in three different locations (A,B and C) in the HD142527 disk. Figure adapted from Honda et al. (2009).

In contrast, it is possible to measure the 3 μm water ice band from the ground either in absorption for near edge-on disks in scattered light at high spatial resolution for more face-on systems, as has been done successfully for a number of disks (Terada et al. 2007; Terada & Tokunaga 2017; Honda et al. 2009). Figure 2-9 shows the imaging detection of the 3 μm water ice band in scattered light in one disk (HD 142527) using narrow-band imaging. Leveraging this observational method with METIS at much higher angular resolution will allow to directly detect water ice in disks, resolve the surface snow line region around solar-mass stars (3 AU $\sim$ 30 mas), and image the distribution of water ice on small dust grains at great detail in more luminous systems.

2.4.3 Isotopic fractionation as a probe of early solar system formation

Isotopologue abundance ratios in Solar System objects provide a key probe of the physical and chemical conditions in the disk out of which our Solar System formed. The ro-vibrational lines of the CO isotopologues – ^{13}CO, $C^{18}O$ and $C^{17}O$, all of which have been detected in disks and young stellar envelopes through infrared spectroscopy at 4.7 μm with VLT-CRIRES are prime targets of METIS (see Figure 2-10) (Pontoppidan et al. 2008; Brown et al. 2013).

The oxygen isotopes are particularly interesting because solar system rocks show an anomalous mass-independent distribution that has defied conclusive explanation since its discovery (Clayton et al. 1973). One leading explanation is isotope selective photodissociation of CO in the upper layers of the disk, followed by vertical mixing and incorporation into water and rocks (e.g., Lyons & Young 2005; Visser et al. 2009). METIS will be able to determine the CO isotopologue ratios for a much larger number of disks than the couple of disks that were accessible with VLT-CRIRES (Smith et al. 2009b), thus directly tracing the origin of water in the inner solar system and formation history of rocks. This case requires high spectral resolution to fully resolve the line profiles, and thus measure accurate optical depths and isotopologue ratios. JWST lacks the high resolution, and rotational emission lines observed by ALMA are affected by systematic errors driven by complex radiative transfer and excitation processes (e.g., Miotello et al. 2014).

2.4.4 Distribution of PAHs and related carbonaceous species

Another set of prominent features seen in many infrared sources are those at 3.3, 6.2, 7.7, 8.6, 11.3 μm (Geers et al. 2006; Maaskant et al. 2014). They are thought to arise from the cooling of transiently-heated polycyclic aromatic hydrocarbons (PAHs) excited by the intense stellar UV radiation. These macro-molecules are important tracers of complex carbon chemistry and control the amount of photoelectric heating in disk surface layers (e.g., Woitke et al. 2009; Bruderer et al. 2012). Measuring the distribution and chemistry (e.g., charge state, amount of dehydrogenation) of PAHs will be an important contribution toward constraining thermo-chemical models.

PAHs also play an important role by providing a source of significant UV opacity in the inner disk, thus affecting the disk structure (e.g., amount of flaring). For a flaring disk, the PAHs at the surface of the disk are in direct view of the central star and their emission bands therefore trace the geometry of the disk surface, even at large distances from the star, beyond that probed by dust mid-infrared thermal emission. Because 8
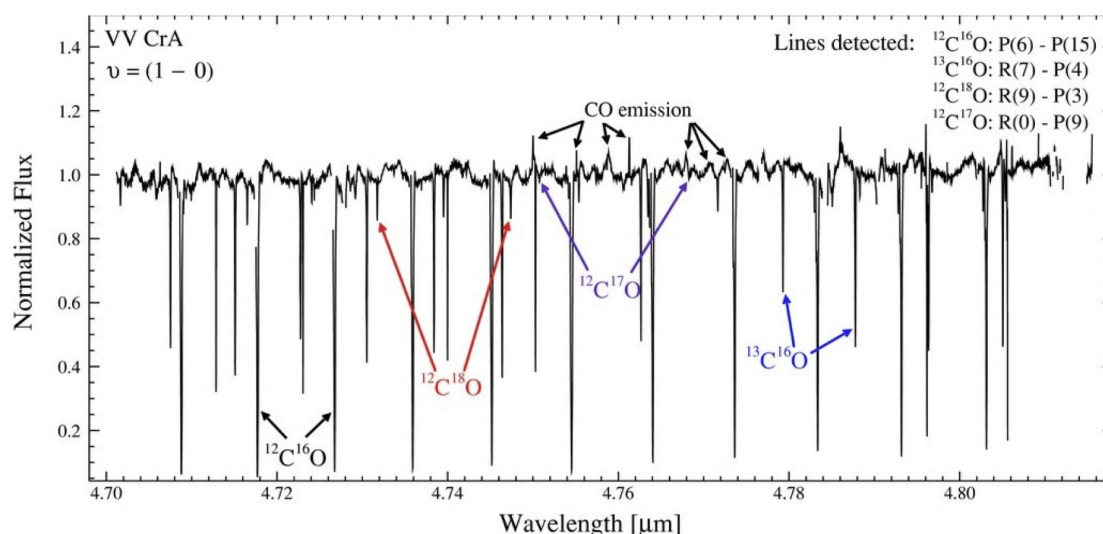
Figure 2-10: Infrared absorption spectra of the CO fundamental ro-vibrational bands toward the VV CrA binary object. The line of sight from the primary star passes through the outer cooler part of the disk around the secondary star in which the gas is seen in absorption. Note the detection of lines of all CO isotopologues, down to $C^{17}O$ (Smith et al. 2009b).

METIS

m telescopes typically only marginally resolve disks around even luminous young stars (Geers et al. 2007b), the geometry, as traced by PAH emission, of only a few protoplanetary disks has been determined. With an angular resolution 5 times better than that of VLT-VISIR, and greatly increased sensitivity, ELT-METIS will be able to image the surfaces and distribution of PAHs for a large disk sample. These METIS observations of disk structure are highly complementary to ALMA dust imaging. Since the latter predominantly traces large grains in the disk midplane, disks such as that of HD 97048 appear symmetric at mm wavelengths (Walsh et al. 2016) but highly asymmetric when observed in PAH emission (Lagage et al. 2006). Thus, only the combination of ALMA and METIS imaging will constrain the vertical stratification and flaring geometry of protoplanetary disks.

METIS observations of PAHs also open up the exciting possibility to understand the evolution of possible carbonaceous building blocks for forming planets or for the parent bodies of meteorites or cometary particles where they are found to be a major component (e.g., Wirick et al. 2009). Indeed, an interesting segregation between PAHs and large grains has been observed at mid-IR for the Oph IRS48 disk, with PAHs present in a gap or inner hole, potentially cleared out by a planet (Geers et al. 2007a; Schworer et al. 2017) (see Figure 2-11). METIS will be able to image the PAH vs. large grain emission down to a few AU resolution, both through the 3.3, 8.6 and 11.2 μm PAH features, and provide insight into their origin. Moreover, METIS will extend the detailed imaging of PAHs in disks around bright Herbig Ae stars to lower-mass, solar-type stars. PAHs are known to undergo chemical changes due to UV radiation, including ionization, hydrogen loss and photodestruction to C_2H_2 as a function of disk radius (e.g., Visser et al. 2007; Zhen et al. 2015; Bouwman et al. 2019). At the other extreme, large PAHs can transform under the influence of UV to fullerenes C_{60} and C_{70} in a 'top-down' interstellar chemistry (Berné & Tielens 2012; Zhen et al. 2014). All of these carbonaceous molecules, from the smallest C_2H_2 to the largest C_{70}, can only be observed at mid-IR wavelengths. The combination of ELT-METIS and JWST-MIRI will provide both the necessary sensitivity, wavelength coverage and spatial resolution (for ELT) to study their distribution across the planet-forming zones of disks.

2.4.5   Crystallization of silicates: when and where?

It is still unclear where and how grain growth and the annealing of silicates take place in protoplanetary disks. In contrast to silicates in the general interstellar medium (e.g. Kemper et al. 2004; Min et al. 2007), a fraction of the silicates in disks is known to be in crystalline form (e.g. Waelkens et al. 1996; Sargent et al. 2009). Thus, the amorphous silicates must be crystallized inside the disk. The most common explanation is annealing at high temperatures (>800 K) in the inner (typically <1 AU) disk (e.g. Gail 1998; Bouwman et al. 2001), but the presence of crystalline silicates in comets (see Solar System section) argues either for
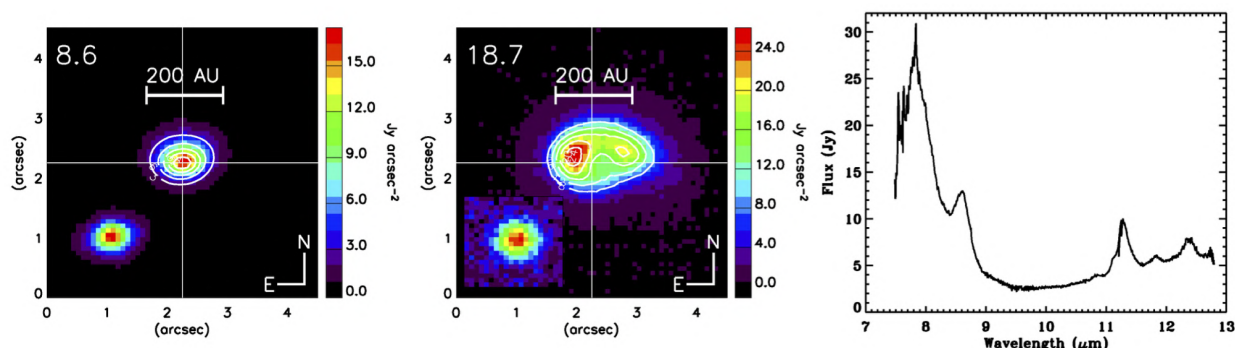
Figure 2-11: VLT-VISIR mid-infrared images of the transitional disk around the young Herbig Ae star IRS 48, showing strong centrally peaked PAH emission at 8.6 μm as well as a 60 AU radius gap devoid of large grains emitting at 19 μm. The inserts show the PSF of a standard star. The 813 μm spectrum with the strong PAH features is included. ELT-METIS will be able to provide spatially resolved integral field spectroscopy of the material (gas + dust) present inside and outside gaps down to the terrestrial planet- forming region (figure based on Geers et al. 2007b).

strong mixing or for alternative crystallization processes, such as shocks or planetesimal destruction, which take place at large disk radii (e.g Harker & Desch 2002), or transient thermal processing during accretion outbursts in which the central object temporarily becomes many times brighter than in quiescence, heating the disk surface (Ábrahám et al. 2009).

The N-band contains the resonance of the Si-O stretching mode, which is widely observed in low-resolution disk spectra (e.g. Kessler-Silacci et al. 2007; Oliveira et al. 2011). The shape of this band is particularly sensitive to both grain growth (e.g. van Boekel et al. 2003) – the first step in planet formation – and to crystallization (e.g. Bouwman et al. 2001). Pioneering spatially resolved VLT-MIDI spectroscopy has opened up the completely new field of mineralogy as a function of position in disks (e.g. van Boekel et al. 2004), but this has been possible for only a handful of sources (e.g. Schegerer et al. 2009). Although METIS does not have the ultimate spatial resolution of VLTI/MIDI and MATISSE, it is more than three orders of magnitude more sensitive, and will enable the observation of a statistically relevant sample of disks, and will constrain the amount of growth and crystallization in the inner versus the outer (>5 AU) disk.

The most prominent example is HD 100546, a transition disk with a large gap possibly carved by a young giant planet (see section 2.3.1), with the inner rim of the outer disk located at ≈ 11 AU (e.g. Garufi et al. 2016) and with a small inner disk of $\lesssim 1$ AU (Panić et al. 2014). In this disk large amounts of cold crystalline silicates are present (e.g. Bouwman et al. 2003; Mulders et al. 2011) but their spatial distribution could so far only be indirectly inferred through SED fitting and is thus poorly constrained. The radius of the outer disk rim is about 4×5 AU along the minor $\times$ major axis; thus, METIS can take high SNR spectra of rim with ~ 15 independent azimuthal samples along the ring, separately from the inner disk.

Another set of interesting targets are binary young stars (e.g., Ratzka et al. 2005; Duchêne & Kraus 2013), especially those with separations in the interesting 3–30 AU range. With its much higher spatial resolution, METIS will be able to obtain images and spectra of individual circumstellar disks, rather than an unresolved composite of these disks or the circumbinary disks around wide binaries probed with current generation telescopes (Ratzka et al. 2009). Do the indvidual disks have similar silicate composition and crystallinity fractions or not? This may provide insight into their formation history, in particular whether they formed through disk fragmentation or cloud core fragmentation. Another aspect is the mass ratio between the two components, which alters the evolution of a binary just like the separation does. The more the mass ratio deviates from unity, the more the influence of the companion is reduced. A 'normal' binary then turns into some kind of a 'star-planet-system', and there are indeed many examples where (substellar) companions influence the circumstellar disk around the primary.

2.5   Debris disks around nearby main-sequence stars

The debris disk stage, which follows the gas-rich protoplanetary disk stage, is a phase of planet formation and evolution that is characterized by growth of terrestrial planets and dynamical interactions between planetesimals and giant planets. This leads to the production of belts of debris as planetesimals collide and are ground down to observable amounts of dust. Debris disk belts are known to be located at several distinct radial regions. Cold dust at large distances (> 50 AU) was the first to be discovered and characterized by IRAS (Backman & Paresce 1993) and subsequently imaged by ground-based submm telescopes, Herschel (Matthews et al. 2014) and ALMA (Hughes et al. 2018). Interestingly, recently more and more detections of warm (~ 150-300 K) dust, located between the habitable zone and the snow line at a few AU, and of hot (> 300 K) dust, within 1 AU, are appearing in the literature, largely driven by mid-infrared surveys in space using Spitzer (Lawler et al. 2009), WISE (Lawler & Gladman 2012) and AKARI (Fujiwara et al. 2013).

The presence of large amounts of warm dust around main sequence stars is likely related to the presence of asteroid belts, or, for young disks, to the formation of terrestrial planets. METIS will be the first instrument to provide detailed images of warm debris disk belts inside the terrestrial planet region at a couple of AU. Two main goals can be identified which are discussed in more detail: (i) detailed study of the properties of particularly bright warm debris disks, and (ii) exploration of the faint end of the brightness distribution of warm debris disks (also known as exo-zodiacal disks).

2.5.1 Terrestrial planet formation in warm debris disks

About 1% of all main sequence stars have detectable warm debris dust in the terrestrial planet region (Morales et al. 2012; Patel et al. 2014), with a higher fraction around younger stars (Meyer et al. 2008b). While a few dozen examples are currently known, this number is likely to increase with higher sensitivity observations. Some of the most well-studied nearby debris disks have dust at < 3 AU, including HD 69830, β Pictoris, and HR 8799, all of which are also famous for hosting planetary systems. Because of the short dynamical/collisional lifetime of dust at such distances from the star, theoretical models show that these warm dust populations must be transient (Wyatt et al. 2007). Possible explanations for their presence range from the late formation of terrestrial planets and major collisions between planetesimals to the delivery of dust by asteroids and comets in episodes of heavy bombardment.

With METIS, the increase of a factor 4 in spatial resolution over current mid-infrared single-dish imaging facilities, along with an even greater increase in sensitivity, promises truly spectacular continuum images of some nearby warm debris disks, as well as the possibility to measure the sizes of a larger sample of more distant disks. The spatial structure, and perhaps even variability, of warm/hot debris disk dust will constrain the fundamental properties (mass, composition, frequency) of asteroid belts and terrestrial planets in other planetary systems, and thereby bring much-needed constraints on the origin of warm dust populations. It should also be possible, in some cases, to infer the presence of a hidden (low-mass) planet by revealing structures in the debris dust from high-angular resolution METIS continuum observations at $10\,\mu$m. Finally, METIS may also reveal terrestrial planets in formation by observing debris dust distributed asymmetrically in the disk, generated in recent collisions (Lisse et al. 2009; Olofsson et al. 2012; Jackson et al. 2014) or even the resulting hot protoplanet collision afterglows (Mamajek & Meyer 2007; Miller-Ricci et al. 2009).

One example of a particularly bright warm debris disk is the F-star eta Crv located at a distance of ~ 18 pc. It has been observed with mid-IR interferometry at the Keck Interferometer and at the Large Binocular Telescope Interferometer (LBTI). Based on these measurements, the location of the dust could be constrained (Lebreton et al. 2016b). One of the most probable disk geometries for this object, for which the dust distribution extends down to 0.8 AU (~ 45 mas), was used to test METIS capability to obtain a resolved image of a warm debris disk. This is illustrated in Figure 2-12, which showcases the capability of METIS to probe in the dust distribution when using the vortex coronagraph, assuming residual PSF subtraction in post-processing based on the observation of a reference star. The disk is only detectable in N band, where the total flux of the disk is about 0.4 Jy (at $10\,\mu$m). This results in a flux ratio between the integrated disk flux and the star of around 20%, but the maximum disk flux in any detector pixel is only about 0.1% of the stellar flux. The disk does not produce much thermal emission at shorter wavelengths due to the dust temperature. For instance, at L band, the contrast between the star and disk is about 1000 times higher, which makes it just out of reach of METIS. The disk would be detectable at M band within an hour of integration time, though, thanks to the onset of thermal emission at that band (see Fig. 2-12). Some other prominent nearby debris disks with warmer dust populations, such as those around ζ Lep, HD 69830, or HD 172555, could potentially also be detected at L band.

2.5.2 Exozodiacal dust

It is expected that most planetary systems harbor small bodies (asteroids and comets). Exozodiacal dust is then supposed to be produced by asteroid collisions or out-gassing of comets. The observational search for exozodiacal radiation is a very active field, not only for its own intrinsic interest but also because this information is needed for any future space mission aimed at the spectroscopic characterization of terrestrial planets in the habitable zone around nearby stars. Indeed, the photon noise of exozodiacal disks with densities 100 times higher than that of the zodiacal disk in our Solar System would dramatically limit the sensitivity of such missions. Furthermore, if asymmetric, an exozodiacal disk 10 times brighter than that of the Solar System could prevent the characterization of an Earth-like planet (Roberge et al. 2012; Defrère et al. 2010, 2012).

Currently, the study of exozodiacal disks with spatially unresolved mid-infrared spectro-photometry is lim-
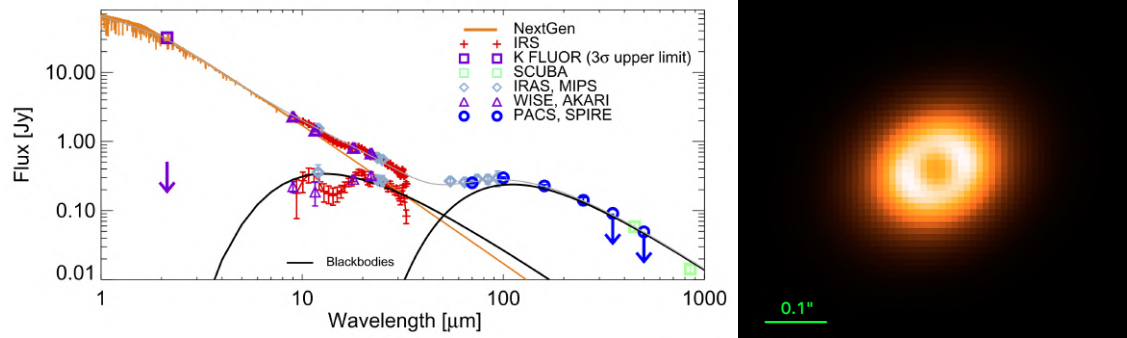
Figure 2-12: *Left.* Spectral energy distribution of the eta Crv debris disk (Lebreton et al. 2016a). *Right.* The eta Crv debris disk as seen by METIS in N band in 1 hour of integration time, using standard PSF subtraction based on the observation of a reference star (RDI) of similar type and magnitude, observed under similar conditions. The simulation was performed with the HEEPS end-to-end simulation tool, using the vortex coronagraph, taking into account a representative 1-h sequence of AO residual phase screens. Disk model courtesy of J. Lebreton (pers. comm.).

ited to disks about 1000 times brighter than the zodiacal disk ("1000 zodis"); the limiting factor is not photon noise, but the precision to which the disk emission can be separated from the overwhelming stellar light. This in turn is limited by the photometric precision (currently around 1%), as well as the precision of modeling the stellar photosphere (Beichman et al. 2006). Only spatially resolved observations can probe fainter exozodiacal disks. The minimum required angular resolution for direct imaging of exozodiacal systems is 100 mas (1 AU for a star at 10 pc). This requirement immediately sets the need for a telescope diameter greater than 20 meters when observing at N band[4]. Note that JWST, with its aperture of 6.5 m, is far from providing such high angular resolution.

Imaging exozodiacal systems has been one of the main goals of the Keck Interferometer Nuller (Millan-Gabet et al. 2011; Mennesson et al. 2014) and of the LBTI (Ertel et al. 2018a). In particular, the recent results of the LBTI exozodi survey in the northern hemisphere have shown a detection rate of 23% for a sample of 34 nearby main-sequence stars (Ertel et al. 2018b). These results put a strong constraint on the median dust level to 16 zodis (95% confidence). While very sensitive, such interferometric observations provide very sparse spatial information, compared to what is achievable with the full aperture imaging promised by the ELT.

Thanks to its increased sensitivity (point-source sensitivity around 50 μJy in 1h at N band), combined with its high angular resolution ($\lambda/D = 50$ mas at N band), the ELT is *the* machine to study exozodiacal emission in the 1 AU region around nearby stars (<10 pc). Based on the predicted point-source sensitivity and achievable contrast of METIS at N band with its vortex coronagraph, we estimate that 100-zodi disks, boasting a total flux of about 20 mJy at N band and an integrated contrast of about 0.1% with their host star, will be within reach. While METIS on the ELT is probably not the most appropriate instrument to extend blind N-band exozodi surveys to the southern hemisphere (unless combined with a planet-hunting research program), METIS could be used to better characterize the dust distribution in the handful of exozodis previously detected with the Keck Interferometer Nuller or the LBTI, or to follow up some nearby WISE detections. METIS observations of exozodiacal light will be complementary to ALMA observations of the cooler dust in exo-Kuiper belts located at a few tens of AU from the star (Hughes et al. 2018). Combining ELT/METIS and ALMA will give a complete picture of debris disks around nearby stars and allow to study, in a statistical way, the link between planet formation and debris disks, as well as the connections between the inner and outer parts of forming planetary systems.

---

[4]Blackbody dust at 1 AU heated by a solar-type star would reach an equilibrium temperature of 270 K and thus have its peak emission around 10 μm

3 DETECTION & CHARACTERIZATION OF EXTRASOLAR PLANETS

3.1 Scientific context

How unique is the Solar system, and Earth in particular? What range of atmospheres do planets have, and why? What are their climates, and what determines whether they are habitable or not? Is there life on other worlds? Excitingly, answers to these existential questions about humanity's place in the Universe will soon be within reach of astrophysical investigations and they are close to the heart of the science case of the ELT, and METIS in particular.

Within the time scale of one generation, the plethora of exoplanet discoveries in our part of the Milky Way has shown that planets and planetary systems are very common, often complex, and very diverse (e.g Dressing & Charbonneau 2015). In addition, ground-based radial velocity surveys (e.g., with ESO's HARPS spectrograph), transit surveys (e.g., by the NASA's Kepler mission from space), and high-contrast imaging surveys on 8m-class telescopes have revealed new classes of planets unknown to the Solar System. These include hot Jupiters, gas giants very close to their host stars, super-Earths or mini-Neptunes, which together represent the majority of exoplanets, and massive gas giants on very wide orbits (e.g., >30 AU), which, are, however, rare. In addition, transit surveys have revealed small rocky planets that are so close to their star that they are disintegrating, showing highly variable tails of dust evaporating off their planet surfaces (Rappaport et al. 2012). One of the great goals of exoplanet science is to link this wide variety of planets to formation and evolution theory, including migration scenarios, aided by the ground-breaking observations of protoplanetary disks. The demographics of planets within a few AU of their parent stars is already relatively well known, with about one in ten of the solar-type stars harbouring gas-giants, one in four harbouring Neptune-mass planets, and most stars having rocky planets (e.g., Petigura et al. 2013).

The ubiquity of Earth-size planets is most evident around cool red dwarf stars for which the radial velocity and transit methods are most sensitive. Combined, they have made the two most exciting discoveries in recent years. These include Proxima b, a planet in an 11-day orbit around our nearest neighbour which could sustain liquid water on its surface (Anglada-Escudé et al. 2016), and the TRAPPIST-1 system of seven Earth-size planets, with two or three of these within the star's habitable zone (Gillon et al. 2017). This immediately raises questions about whether the atmospheres of small planets around late M-dwarfs are not eroded by the energetic flares of their host stars, and whether they have not lost all their water in the extended pre-main sequence phase during which their host stars where significantly brighter (Ribas et al. 2016; Turbet et al. 2016; Segura et al. 2010). In the coming years, leading up to ELT's first light, an almost complete census of the local exoplanet population will be achieved, in particular for planets on relatively close-in orbits around late-type stars (e.g., Ribas et al. 2018), by dedicated radial velocity machines (e.g., HARPS, NIRPS, HARPS-N, CARMENES, HARPS3), and transit surveys (e.g., TESS, PLATO, SPECULOOS).

3.1.1 Planet characterization

Giant leaps forward have also been achieved in the atmospheric characterization of extrasolar planets. While most planets are found without identifying a single photon from the planets themselves, atmospheric studies require separation of planet light from that of the star. To understand habitability, and to be able to unambiguously identify potential biomarker gases in the future, a deep understanding of atmospheric processes and evolutionary histories of planets is necessary, over a wide range of planet orbit, mass, and stellar host star characteristics. What are the main constituencies of a planet atmosphere? Do we understand its chemistry? What are the main atmospheric circulation patterns? What is its climate like? Can we link its abundances to formation processes? How important are photochemical processes? Is there any evidence for atmospheric loss?

The first successful studies of extrasolar planetary atmospheres were obtained from transmission and secondary eclipse spectroscopy of transiting hot Jupiters using the Hubble Space Telescope (HST) and the

Spitzer Space Telescope (e.g., Charbonneau et al. 2002; Deming et al. 2005). Such studies have now revealed atomic absorption from atmospheric sodium, and hydrogen, oxygen, and carbon in extended exospheres of hot Jupiters - and recently from helium (e.g., Nortmann et al. 2018). In addition, molecular signatures from water have been revealed for a dozen or more planets as well as evidence for Raleigh scattering at UV and optical-blue wavelengths (Sing et al. 2016). Extension of such studies to cooler and smaller planets have been hampered by the apparent prevalence of clouds that strongly dampen potential transmission features (Kreidberg et al. 2014). Secondary eclipse spectroscopy and phase curve measurements in the near- and mid-infrared have constrained the dayside temperatures and thermal structures - both vertically and longitudinally - for some of the hottest planets. They provide the first insights in how stellar energy is absorbed by such planet atmospheres and distributed to the night side as a first test for global circulation models (Showman et al. 2009).

The James Webb Space Telescope (JWST), which is expected to be launched a few years prior to METIS first light, will provide another leap forward in planet atmospheric studies, in particular using transmission and secondary eclipse spectroscopy. Its ability to observe a large part of the near-infrared spectrum simultaneously (a factor four increase compared to HST), its increased stability by being at L2, its five times larger collecting area than HST, and in particular its ability to observe at much longer MIR wavelengths will be unique. It is expected to provide detailed spectral signatures of the most important spectroscopically active molecules of hot and warm Jupiters, and push towards smaller and cooler planets - in particular by observing at long wavelengths where clouds and hazes are expected to be less invasive (e.g., Morley et al. 2017). JWST/MIRI will probably be able to detect thermal emission from the hottest planet in the TRAPPIST-1 system and determine whether it has an atmosphere - a first step towards the general assessment of habitability on planets around red dwarf stars (Ribas et al. 2016).

3.1.2   Ground-based techniques

In parallel to space-based observations, ground-based techniques are playing an increasingly important role, and are now generally recognized as the fasted route to the first characterization of temperate rocky planets[5], a goal that from space will only be achieved by large direct imaging missions such as LUVOIR or HABEX, possibly in the 2040s. High-contrast imaging, through the continuing development of advanced adaptive optics and coronagraphic techniques (e.g., VLT/SPHERE, Gemini/GPI), has now discovered about a dozen planetary systems. In direct imaging, detection means immediately characterization, with multi-wavelength observations revealing molecular absorption signatures from, e.g., water and methane. Direct imaging observations are currently restricted to young (< 100 Myr) systems in which the (gas giant) planets still radiate significant heat left over from their formation. While micro-lensing surveys, radial velocities, and incoming astrometry from GAIA all play an essential role in creating a statistical synopsis of planet occurrence and mass distrbution at relatively wide orbital separations (> 5 AU), only direct imaging gives access to information about the atmospheres of these long-orbit planets.

Another powerful technique developed over the last decade is high-resolution spectroscopy (R~100,000; Snellen et al. 2010a; Brogi et al. 2012). The high resolving power is used to separate out the much stronger contribution from the star and the Earth atmosphere from that of the targeted planet, allowing unambiguous detections of atomic and molecular species, and at the same time being sensitive to Doppler effects from the orbital motion of the planet, atmospheric winds and circulation, and the spin-rotation of the planet (Snellen et al. 2015). Particularly powerful is the combination of the two methods - high-contrast imaging and high-resolution spectroscopy (e.g., Sparks & Ford 2002; Riaud & Schneider 2007; Kawahara et al. 2014; Snellen et al. 2015; Lovis et al. 2016). Although this technique is still in its infancy, it has already led to exciting results (Snellen et al. 2014; Hoeijmakers et al. 2018b), and is being implemented with high priority on the VLT, Keck, Subaru, and LBT telescopes - and now with METIS on the ELT.

---

[5]Exoplanet Science Strategy Report 2018; National Academy of Sciences

3.1.3   The power of METIS

METIS will be transformational in exoplanet studies for several reasons:

- The increase in telescope diameter from the VLT to the ELT results in an improvement in angular resolution of a factor 5. At the same wavelength, it can probe planets five times closer to their host star.

- The mid-infrared wavelength range opens up the way to significantly older and cooler planets - down to mature planetary systems in the direct vicinity of the Sun.

- The integral field spectrograph with a resolving power of R=100,000 is unique in the world, and the ideal tool to combine the high-resolution spectroscopic techniques with high-contrast imaging. Characterization of the temperate planet Proxima b will be within reach (see Section 3.3).

As detailed below, METIS will open up a whole new part of parameter space (cf. Figure 3-1), revealing, for instance, mature gas giant planets orbiting nearby stars. In addition, it can even reveal temperate rocky planets around our nearest neighbours with N-band imaging. Characterization of the hottest planets will result in atmospheric surface maps, detailed temperature structures as function of longitude, molecular abundance ratios, and even isotopologues (Mollière & Snellen 2018). Most excitingly, it is expected that basic characterization can be extended to temperate rocky planets in the habitable zones of our nearest neighbours, such as Proxima b, revealing whether it has an atmosphere, its dayside temperature, and whether its atmosphere contains carbon dioxide, methane, and/or water - a first assessment of the habitability of this enigmatic world.

The study of extrasolar planets will be one of the prime science goals of METIS and with its unique combination of spatial resolution, spectral resolution and unprecedented sensitivity from the ground, METIS will have a ground-braking impact in both extrasolar planet detection and characterization. Some key science cases are detailed in the following sections. It should be emphasized that the main focus in this chapter is put on mature exoplanets and that science cases related to planet formation and young (proto-)planets are discussed in chapter Protoplanetary Disks and the Formation of Planets. Also, the investigation of free-floating planetary mass objects is not discussed in the following, as neither high-spatial nor high-spectral resolution are necessarily required to characterize the infrared SEDs of such objects and JWST, with its unparalleled sensitivity, is better suited for that purpose.

3.2   Planetary demographics

Despite their high-performing AO-systems current high-contrast imaging instruments on 8-m class telescopes will always be limited by their – compared to the ELT – modest aperture size. In consequence they will never be able to systematically probe for cool, mature planets down to a few AU for a larger sample of stars. METIS has this capability and will open up completely new discovery space for exoplanet imaging studies.

3.2.1   The occurrence rate of long period gas giant planets

A key task for modern exoplanet research is to assess the frequencies and properties of wide-separation, Jovian-mass planets at the youngest ages. In addition to simply measuring occurrence rates, observing these low-mass companions as early as possible (e.g., Kraus et al. 2014) will largely eliminate any confusion about the initial locations of planet formation caused by subsequent dynamical processes (e.g., Scharf & Menou 2009; Chatterjee et al. 2008), and in turn, provide essential initial conditions to theoretical and numerical models of planetary formation. In addition to pinpointing the locations of the recently formed planets, observing the *luminosity* of these objects in the first few million years is essential to constrain models of their initial entropy and temperatures (e.g., Fortney et al. 2008).
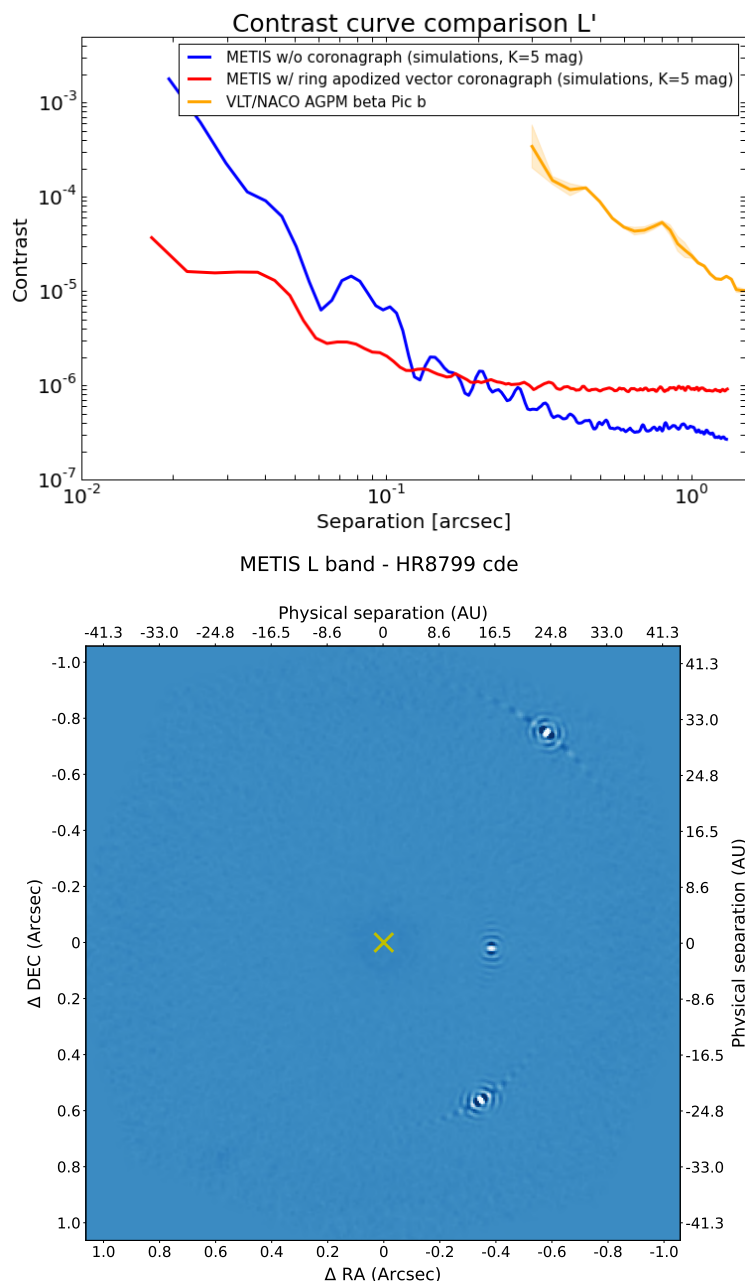
Figure 3-1: Illustrating the discovery space of high contrast imaging with METIS in the L band. Top: Comparison between a measured contrast curved obtained with VLT/NACO in the L band using the AGPM Vortex coronagraph on the planet hosting star beta Pictoris (Absil et al. 2013, yellow curve) and predictions for ELT/METIS in the same filter based on the end-to-end high-contrast simulator (blue curve w/o a coronagraph; red curve with a ring-apodized vector coronagraph (RAVC) for a 1h ADI sequence). Bottom: METIS simulations of the HR8799 planetary system in L band with the ring-apodized vortex (RAVC), in 1h of observing time. The four planets are within the METIS FoV, but our simulations stop at 1.2" and therefore only show the inner 3 planets. The SNRs are, respectively, 49, 21, and 19, and several diffraction rings can be seen around the planets.

.

To simulate the sensitivity to low-mass (planetary) companions using high contrast imaging with METIS, 35 early-type stars (spectral types A to F) were selected from the de Zeeuw et al. (1999) compilation of objects in the ~11-16 Myr Scorpius-Centaurus Star forming region (hereafter "Sco-Cen"). The selected targets have a mean distance of 130 pc, a membership probability of >95% as determined by Rizzuto et al. (2011), and were verified as single stars from the literature (i.e., no unresolved binary companions). An assumed age of 11 or 16 Myr, as well as the estimated L-band contrast (cf. Figure 3-1) was assigned

to each star to determine the sensitivity as a function of angular size from the host star for each target. The corresponding absolute magnitude was then converted into physical masses using evolutionary models (Baraffe et al. 2003) to provide an estimate of the sensitivity of METIS to low-mass companions for each star. Finally, the Multi-purpose Exoplanet Simulation System ("MESS") software (Bonavita et al. 2013) was used to derive a map of our completeness as a function of limiting mass and semi-major axis for the ensemble of 35 stars.
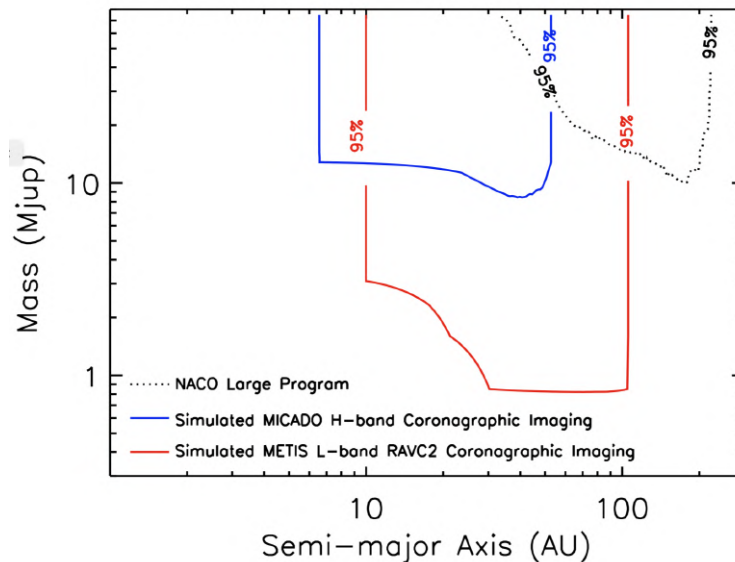
Figure 3-2: Simulated discovery space for low-mass companions expressed in terms of 95% completeness contours for a sample of 35 stars in the 11-16 Myr Sco-Cen star forming region using METIS L-band high contrast imaging with the RAVC coronagraph (red line). Also shown is the corresponding sensitivity for the same set of stars using MICADO in the H-band (blue). For reference, the corresponding 95% completeness contour for the recently completed VLT NACO Large Program survey (Vigan et al. 2017) is shown in black.

Figure 3-2 shows the results of this exercise, displaying the expected 95% completeness for METIS L-band high-contrast imaging using the RAVC coronagraph, combined with speckle removal at the post-processing stage (red line). For reference the 95% confidence contour for the NACO Large Program survey (Vigan et al. 2017, black curve) is also shown. To demonstrate how METIS operating in the L-band would compare to conventional high contrast imaging at a shorter wavelength with a different instrument, the estimated H-band contrast performance for MICADO, another first generation ELT instrument, was applied (Perrot et al. 2018) to this same set of 35 Sco Cen Stars. The H-band was selected for this comparison since this bandpass affords very small angular resolution on a 39m telescope ($\lambda/D \sim 8$ miliarcseconds at H-band), while still maintaining some level of significant AO correction (e.g., $\sim$20% Strehl). Completeness contours were then generated for this same ensemble of stars in the same was as above, and are plotted in blue in Figure 3-2. Given the enhanced brightness of planets from 3-4 μm (e.g. Barraffe et al. 2003), METIS operating in L-band can access very low mass planets ($\lesssim$0.5-1.0 $M_{\rm Jup}$), for a given contrast.

The goal of Figure 3-2 is merely to demonstrate the estimated performance of METIS in the context of other first-generation ELT instruments, rather than to suggest that such a survey would actually be carried out. An exoplanet imaging survey conducted at the ELT would certainly require the support of a large fraction of the community because of the significant investment of telescope time. However, the tremendous increase in imaging sensitivity afforded by METIS, combined with its access to small separations (down to a few AU) would allow us for the first time to probe for exoplanets on Solar System scales around hundreds of nearby stars.

3.2.2   Direct detection of known gas giant planets

Planets detected by RV or astrometry: While masses and brightness temperatures are known for nu-

merous hot Jupiters and Neptunes from transit and secondary eclipse studies, only for the directly imaged exoplanet β Pictoris b both its mass and luminosity are empirically measured (Snellen & Brown 2018). RV detected planets tend to orbit too close to their host star for current imaging instruments to spatially resolve them (e.g., Zurlo et al. 2018) or they are simply too faint (Mawet et al. 2018). Vice-versa, the known directly imaged bona-fide exoplanets orbit too far away from their host stars to create a detectable RV signal. In the case of the HR8799 system we have at least some dynamical constraints on the planets mass from stability arguments (Wang et al. 2018). With METIS, this situation will start to change.
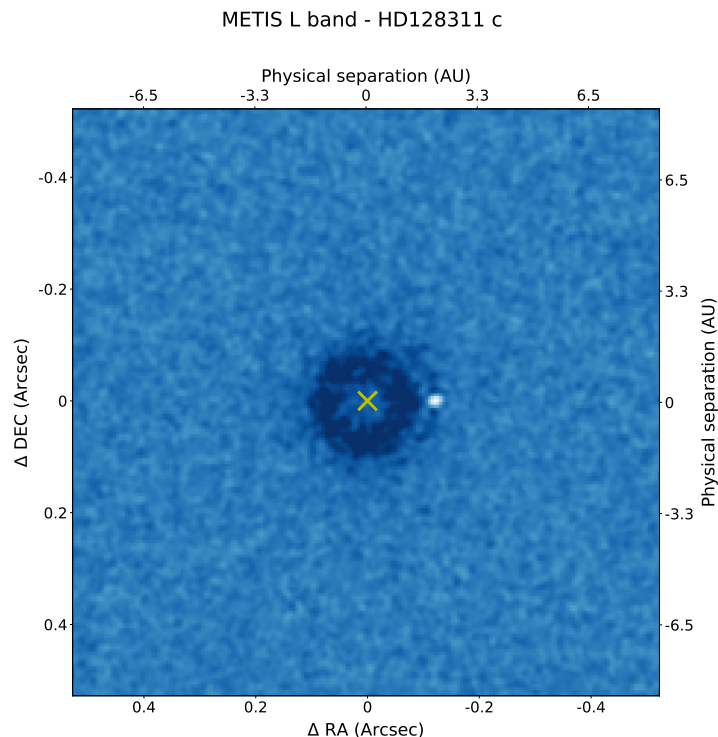
Figure 3-3: METIS high-contrast simulations of HD 128311 in the L' filter assuming a 1h ADI sequence with the ring apodized vortex vector coronagraph and a PCA-ADI based PSF subtraction scheme. The known radial velocity planet HD 128311 c (separation: ~0.12" (~2 AU); mass: ~3.2 M_{Jupiter}; contrast: ~5.2e-6) is clearly detected.

A first analysis to estimate how many of the known RV planets are accessible to METIS in at least one filter was presented in Quanz et al. (2015b). In Figure 3-3 we demonstrate, taking into account updated simulations concerning METIS' contrast and sensitivity performance, that the direct detection of radial velocity planets is indeed feasible. To further get an idea how many objects might be within the reach of METIS, we went through all RV planets listed in the exoplanet.eu database and computed the most favorable epoch for direct imaging observations based on the observed RV curve. For this specific location on its orbit we then determined the planet's effective temperature as the maximum of either its effective temperature predicted by evolutionary models based on its age and minimum mass or its equilibrium temperature given its separation and the luminosity of its host star and assuming a Bond albedo of 0.3. For at least 8 planets (including Eps Ind A b (Feng et al. 2018) and Eps Eri b (Mawet et al. 2018), which are both located close to or in the background-limited regime, where the contrast curves do not matter too much any more), METIS provides sufficient contrast and has a reasonable chance of detecting them in the L' and/or M' filter in 1-2 hours observing time. These gas giant planets cover a range of masses and temperatures making these measurements of utmost importance to confront theoretical models of planet formation and evolution as well as atmospheric models with empirical data. It is important to keep in mind that in the coming years the list of potential targets will continue to increase as longer time baselines of RV surveys will allow for the detection of additional long-period exoplanets. Also stars showing a long-term RV trend are potentially interesting targets.

In addition to RV surveys, ESAs GAIA mission promises to provide a number of additional targets where

the masses will have been determined from the astrometric wobble the planets induce on their host stars, in particular low-mass M stars (Sozzetti et al. 2014). First estimates on the final astrometric performance of GAIA, based on in-flight data, are available[6], but quantitative predictions for the expected METIS yield are still work-in-progress.

Highly Eccentric Jovian Planets: As discussed, METIS will possess the necessary angular resolution to directly image a collection of planets identified through previous radial velocity surveys. Imaging this population of planets will be exceedingly challenging, as nearly all such objects will have "solar" ages of $\sim$1-10 Gyr, and thus be vastly less luminous than those planets revealed from early direct detections of planets with typical ages of $\sim$10-100 Myr. However, a small subclass of RV-detected extrasolar planets may be significantly overluminous and therefore provide a "shortcut" to the path of direct imaging: highly-eccentric ($e \gtrsim 0.9$) exoplanets detected through previous RV-surveys.

A growing body of theoretical work has shown that these planets, which are in super-eccentric orbits possibly due to an external perturbing (third) body (e.g., Socrates et al. 2012; Dong et al. 2014) experience significant *tidal* heating as they pass through periastron. As a result, despite their roughly solar ages, the self-luminosity of these tidally heated planets is dramatically boosted by 2-3 orders of magnitude to star/planet contrasts of $\sim 10^4$-10^6. These vastly more favourable contrasts, combined with the angular separations from their host star of a few λ/D at apastron, places them within reach of the imaging capabilities of METIS at 3-5 μm (Dong et al. 2013).
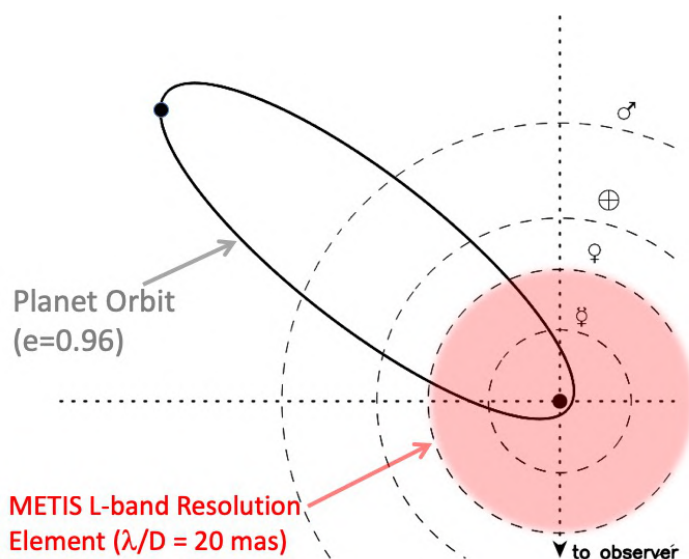
Figure 3-4: A figure adapted from Kane et al. (2016) showing the orbital architecture of HD 20782 b, the exoplanet with the highest known eccentricity ($e \sim 0.96$). Superimposed on the orbit of this exoplanet is the estimated size of the L-band resolution element (1 λ/D, red circle), indicating that this planet will have an angular separation of several resolution elements when the planet is at periastron. The close passage of the planet at periastron means that intense tidal heating of the planet will boost the intrinsic luminosity of the planet making it detectable with METIS, despite its roughly solar age (1-10 Gyr).

Importantly, imaging these super-eccentric planets will afford a host of scientific investigations, not accessible to the population of ordinary RV-detected planets with typically low eccentricities, nor to the planets detected through previous direct imaging efforts. The population of highly eccentric Jovian planets will place extremely powerful constraints on the interior structure and central concentration of planet interiors, such as the tidal "Q" factor and Love number (e.g., Batygin et al. 2009) which can, in turn, help to disentangle various models of planet formation.

Equally important, this class of super-eccentric Jovian planets are extremely powerful "laboratories" for studying the atmospheric *dynamics* of these exoplanets (e.g., Langton & Laughlin 2008). These exoplanetary atmospheres exist in conditions vastly different than the small number of exoplanets characterized so

---

[6]https://www.cosmos.esa.int/web/gaia/science-performance

far through direct imaging *and* transmission spectroscopy. Indeed, as these planets pass through periastron, they undergo a period of very intense "flash-heating". The rapidity with which an exoplanet is able to absorb (and perhaps advect) this burst of stellar energy after its periastron passage will provide extremely meaningful clues about the radiative, advective, and chemical timescales associated with energy transport in these exoplanetary atmospheres. Specifically, examination of the atmospheric properties of these super-eccentric exoplanets will ultimately reveal how the atmospheric dynamical and radiative timescales balance the timescales associated with achieving chemical equilibrium. Additionally, since the radiative timescales for planetary atmospheres may only be a few days, compared to a few months for the advective timescales (e.g., Showman et al. 2009; Mayne et al. 2014), these "flash-heated" exoplanets will likely undergo intense evaporation of atmospheric condensates during periastron passage, followed by rapid condensation back into clouds as the planet approaches its furthest distance from the star.

Fig. 3-4 shows an estimate of the orbital architecture of the planetary system HD 20782 b, a $\sim 2 M_{\text{Jup}}$ planet with the highest known eccentricity of any exoplanet (e=0.96), initially discovered through precision radial velocity monitoring. The orbital geometry suggests the planet will have a sky-projected angular separation at apastron of 50-70 miliarcseconds, corresponding to 3-4 METIS resolution elements (3-4 λ/D) operating in the *L*-band, making it within reach of METIS. Further, when METIS achieves first light, numerous radial velocity surveys will have completed nearly a decade of precise radial velocity monitoring of additional planetary systems, providing numerous more highly eccentric planets for characterization of their atmospheres and structures with METIS.

3.3　Atmospheric properties and climates

METIS will bring unparalleled instrumental power to the field of exoplanet atmospheric characterization. Its combined high spectral resolution and IFU capabilities make it a unique machine with the potential to deliver game-changing results, from the first atmospheric maps of giant exoplanets (exocartography) to the first detections of possible biosignatures in our nearest neighbouring rocky worlds, such as Proxima b.

At the spectral resolution of METIS (R=100,000), the dense forest of lines in molecular bands are individually resolved, revealing the line shape of the planetary spectrum (see Figure 3-5 and Birkby 2018). This probes not only the atmospheric composition and structure, but gives access to a full 3-dimensional view of the planet's atmospheric dynamics and global weather patterns, including day-to-night winds and jet-streams (e.g. Snellen et al. 2010b; Brogi et al. 2016; Flowers et al. 2018), as well as the length of the planet's day or its tidal-locking via rotational spectral broadening (Snellen et al. 2014; Schwarz et al. 2016; Brogi et al. 2016). Current instrumentation limits this work to hot Jupiters and the very brightest of the directly imaged planets. METIS opens the way to smaller, cooler worlds, including the bountiful yet enigmatic super-Earths and mini-Neptunes, and into the Earth-like analogues. Below we discuss these key advancements that METIS will bring by dividing the exoplanet population into short and long orbit systems. The latter requires both the high spatial and spectral resolution of the METIS IFU to disentangle the planet from its host star, while the former relies on the high resolution alone, using only the Doppler shift of the planet's spectrum to extract it from the glare of its host star.

3.3.1　Short-period planets

A major driving force behind the design of the METIS high-resolution (R=100,000) L and M band integral field spectrograph is the ground-breaking success of the high spectral resolution technique used with instruments such as CRIRES(+), to characterize the atmospheres of hot Jupiters. This includes the first unambiguous and ground-based detection of water in an exoplanet (Birkby et al. 2013), and the first atmospheric characterization of a non-transiting close-in planets (see Figure 3-5, Brogi et al. 2012). Both of these were key in optimizing METIS to search for biosignatures of the nearest exoplanets, as these are unlikely to transit their host stars. The technique has also found CO, TiO, Fe, Fe+, Ti+, and HCN in hot Jupiters indicating successful detection of chemical species, even in relatively low abundance (Snellen et al.

2010b; de Kok et al. 2013; Brogi et al. 2016; Birkby et al. 2017; Nugroho et al. 2017; Hoeijmakers et al. 2018a; Hawker et al. 2018). These detections are the result of integrated signals i.e. the sum of all the spectral lines in the molecular band. METIS' strong increase in sensitivity compared to present-day facilities promises to open a whole new range of measurements. For the first time we will have high signal-to-noise, high-resolution spectra of exoplanet atmospheres where we can measure the strengths of individual lines. This enables detailed atmospheric modeling, including probing the atmosphere as a function of both altitude and longitude, revealing dawn-to-dusk variations in the planet's chemistry.

Our calculations based on the METIS instrument design and the current sample of known exoplanets indicate that at least 10 short-period gas giants can be studied in this unprecedented detail, with S/N per line > 10 with just a 1-3 half nights of observation. A single planet studied with CRIRES+/VLT to this level would take a half year of observations (~ 185 nights). Moreover, a key sample of at least half a dozen smaller, mini-Neptune-like planets will become accessible with METIS with integrated signals at S/N> 5 for thorough inventories of their atmospheric constituents and studies of their atmospheric circulation. Again, it would take ~ 200 nights to achieve the same for just one mini-Neptune with CRIRES+. METIS will be the instrument to reveal details about this poorly understood class of exoplanet that are the most common outcome of the planet formation process. The calculated sample sizes for METIS do not include the upcoming onslaught of planet discoveries from TESS that will be found preferentially around bright stars.

For the brightest systems, METIS may even reveal molecular isotopologue ratios (Mollière & Snellen 2018). The high-dispersion IFU mode will also be highly promising for isotopologue studies of CO, CO_2, CH_3D and HDO, providing unique insights into the formation history, such as icy body enrichment, and atmospheric evaporation processes, for a wide range of exoplanets (Mollière & Snellen 2018). CH_3D can be best targeted at 4.7 microns, and may be detectable in planets below 600 K in equilibrium temperature. In this case, the sky background becomes the dominating noise source for self-luminous planets. HDO is best targeted at 3.7 microns, and is less affected by sky background noise. It may lead to its detection for planets with T_{equ} below 900 K. It could already be in the range of current 8m-class telescopes in the case of quenched methane abundances. If Proxima b is water-rich, the HDO isotopologue could be detected with the ELT in less than a few nights of observing time in its reflected-light spectrum (Mollière & Snellen 2018).

All this illustrates the enormous discovery potential for METIS, providing unique information on exoplanets and their atmospheres inaccessible to any other currently planned facility. It should be mentioned that, in particular for this observing mode, METIS will have strong synergies the ELT HIRES instrument that covers the near-infrared wavelength range. Combined, these instruments will deliver the most detailed probes of the atmospheres of short-orbit planets, covering a vast range of atmospheric pressures and scale heights, temperatures ranges, and molecular species. This will enable a far deeper understanding of the full range of systems possible as end-products of the planet formation process, and give insight into the commonality of other Earth-like worlds.

3.3.2   Long-period planets

While the exoplanets discussed in the previous section are likely tidally locked to their host stars, making the rotational period of these objects identical to their orbital periods, METIS will also contribute significantly to our understanding of longer period (gas giant) planets. One decade ago, astronomers believed that it would take a space interferometer of several kilometers in size to resolve structures on exoplanets – beyond the dreams of even the biggest optimists. However, work with CRIRES/VLT indicated that Doppler-imaging, a technique regularly used to map star spots on stars, can also be used to map the atmospheric features of field brown dwarfs, as shown in Figure 3-6 (Crossfield et al. 2014). Crossfield (2014) further show that there are at least 10 more brown dwarfs that could be mapped with METIS' IFU using the SCAO. Even more excitingly, simulations by Snellen et al. (2014) show that METIS has the power to map features e.g. large storms like Jupiter's Great Red Spot, in the atmosphere of beta Pic b, one of the brightest directly
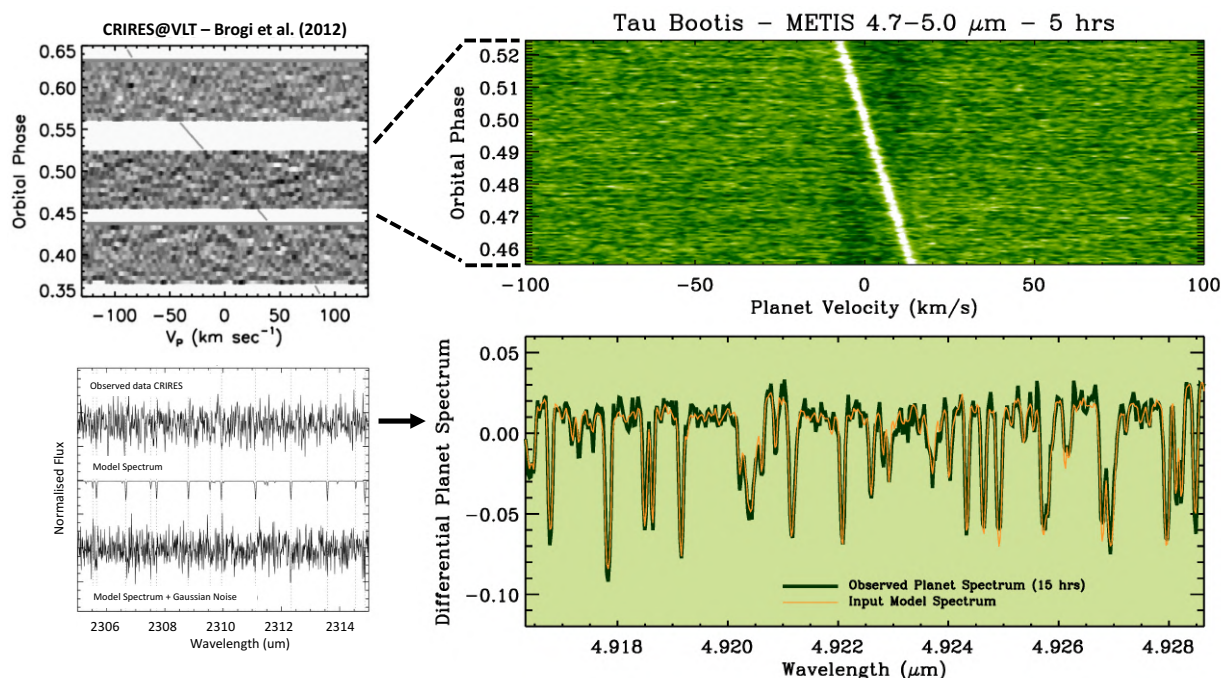
Figure 3-5: METIS IFU simulations of dayside spectroscopy of the hot Jupiter Tau Bootis b. The upper and lower left panels show the planet planet cross-correlation signal as function of orbital phase and the integrated planet spectrum as obtained with CRIRES at 2.3 micron (Brogi et al. 2012). Individual planet lines were visible at about 1 sigma, making the planet detectable only by integrating over time and over all observed lines. The right panels show the same for simulated METIS observations at 4.7-5 micron. The individual planet lines are detected up to 10 sigma, allowing for detailed atmospheric characterization.

imaged planets. This could be done twice as fast as it took to map the brown dwarf with the VLT, despite the nearby bright host star. This is thanks to the powerful combination of both high-resolution spectroscopy and high spatial resolution the METIS IFU design.

In addition to mapping the 2D appearance of exoplanet atmospheres, high-resolution spectroscopy showed that another new observable has emerged helping to constrain planet evolution planetary spin. Observations with CRIRES show that the exoplanet β Pictoris b spins with an equatorial velocity of almost 100.000 km per hour, implying an 8 hour day on this world (Figure 3-6; Snellen et al. 2014). Interestingly, the fact that β Pictoris b spins so fast is well in line with the trend of spin rotation with planet mass seen for the solar system planets, and is likely a relic of the planet formation process during which mass and angular momentum are accreted. METIS will determine the rotation of dozens of exoplanets for a range of masses an exciting new science case. These planets are also highly suited for dawn-to-dusk and seasonal studies, monitoring throughout their days and along a large part of their orbits, tracing the seasonal as well as rotational changes in molecular signals.

The design of METIS affords one further key advantage in the understanding of the planet formation process. Spectroscopic observations in the L and M band with METIS' long-slit modes provides a spectral resolution of $R \approx 1500$-2000 over the whole spectral windows, allowing constraints on dozens of giant planet atmospheric compositions and cloud properties (e.g., Lee et al. 2013) and the search for chemical non-equilibrium (e.g., Fortney et al. 2008; Skemer et al. 2012). Until now atmospheric studies of long-period gas giants in the 3-5 μm range was restricted to a small sample of objects and largely based on narrow band photometry (e.g., Skemer et al. 2014, 2016). Chapman et al. (2017) demonstrated that a wavelength coverage from 0.5-5 μm is better, by about an order of magnitude, at constraining atmospheric abundances than coverage limited to wavelengths <2.5 μm. This is largely due to features of $CH_4/CO_2/CO$ at 3.6/4.3/4.8 μm, respectively. Possibly even more exciting are the prospects of obtaining an N-band spectrum of the brightest directly imaged exoplanets, such as β Pic b and, depending on the final N-band sensitivities, po-
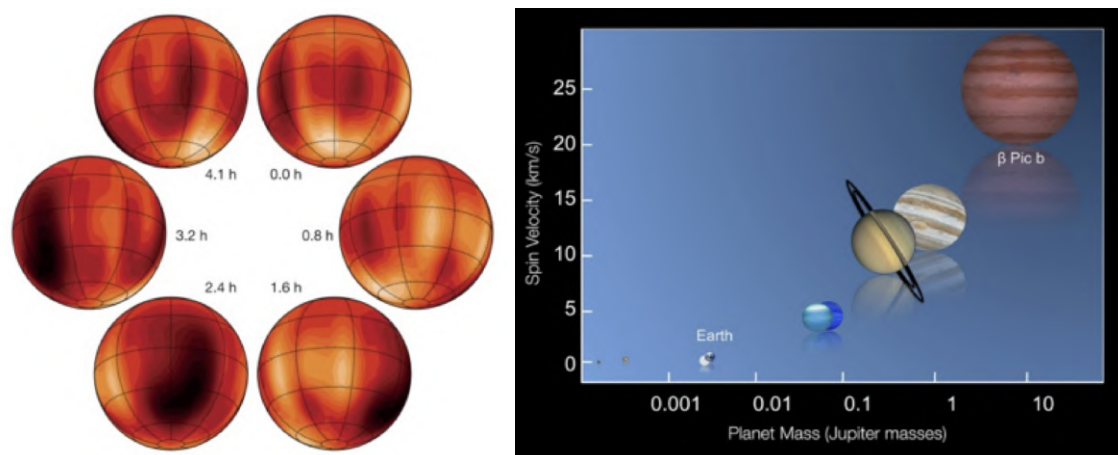
Figure 3-6: Left: Illustration of the Doppler Imaging technique with VLT/CRIRES showing a 2D map of the nearby brown dwarf Luhman 16 B (Crossfield et al. 2014). Right: Comparing the spin velocity of the exoplanet β Pictoris b, as measured from high-resolution spectroscopy, with the spin of the Solar System planets (Snellen et al. 2014).

tentially also HR8799 e and d. JWST/MIRI has the potential to obtain high-quality MIR SEDs for a large number of ultra-cool field objects and wide-separations companions in the background limited regime (e.g., Danielski et al. 2018), but for closer-in companions METIS' superior spatial resolution is key.

METIS spectroscopy will hence provide a new look at the properties of atmospheres of (young) long-period gas giant planets (e.g., C/O ratios, metallicity), which can then be compared to those of hot and warm gas giant planets studied, by for instance JWST, in transmission and secondary eclipse spectroscopy (Todorov et al. 2016). This will enable comparative exoplanetology, such that we may be able to begin an in-depth assessment from a statistical vantage as to the connection between these present day atmospheres and to what extent they can trace back to how and where the planet formed in its protoplanetary disk (e.g., Thiabaud et al. 2015; Eistrup et al. 2018).

3.4   Towards other Earths

NASA's Kepler mission revealed that small planets with radii <4 R_{Earth} are abundant (e.g., Borucki et al. 2011b; Rowe et al. 2015; Hsu et al. 2018) and the detection of small planets around Proxima Centauri (Anglada-Escudé et al. 2016) and Barnard's star (Ribas et al. 2018) indicates that also in the immediate Solar neighborhood small planets orbit other stars[7].

At the moment potential future space-based missions to image Earth-like planets and characterize their atmospheres are still in their definition phase and will likely not fly at least until a decade or so after METIS' first light. Also, unless even more favorable small, transiting planets are found, the James Webb Space Telescope will only provide limited characterization capabilities to study the atmospheres of the TRAPPIST-1 planets, GJ 1132b and LHS 1140b via primary transit and/or secondary eclipse (Morley et al. 2017). Theoretically, small, warm planets around the nearest stars emit both enough thermal radiation and reflected light for METIS to detect them (Quanz et al. 2015b) and if they exist METIS may indeed directly image small, warm planets orbiting stars in the vicinity of the Sun – potentially even habitable planets.

This is further illustrated in Figure 3-7 where we compare the expected flux of an Earth-twin[8] orbiting α Cen A to the expected contrast and sensitivity achievable with METIS in the N2 filter. This analysis re-emphasizes two important points: (a) the habitable zone around α Cen A lies in the background-limited and not contrast-limited regime; hence observations need to be optimized for throughput and not contrast if the search is focused on habitable zone planets. (b) METIS would indeed be able to image an Earth twin if

---

[7]The detection of a small, hot planet around Alpha Cen B (Dumusque et al. 2012) has been disputed in the literature (Rajpaul et al. 2016)

[8]An Earth-sized planet receiving the same amount of flux as Earth and emitting the same spectrum.
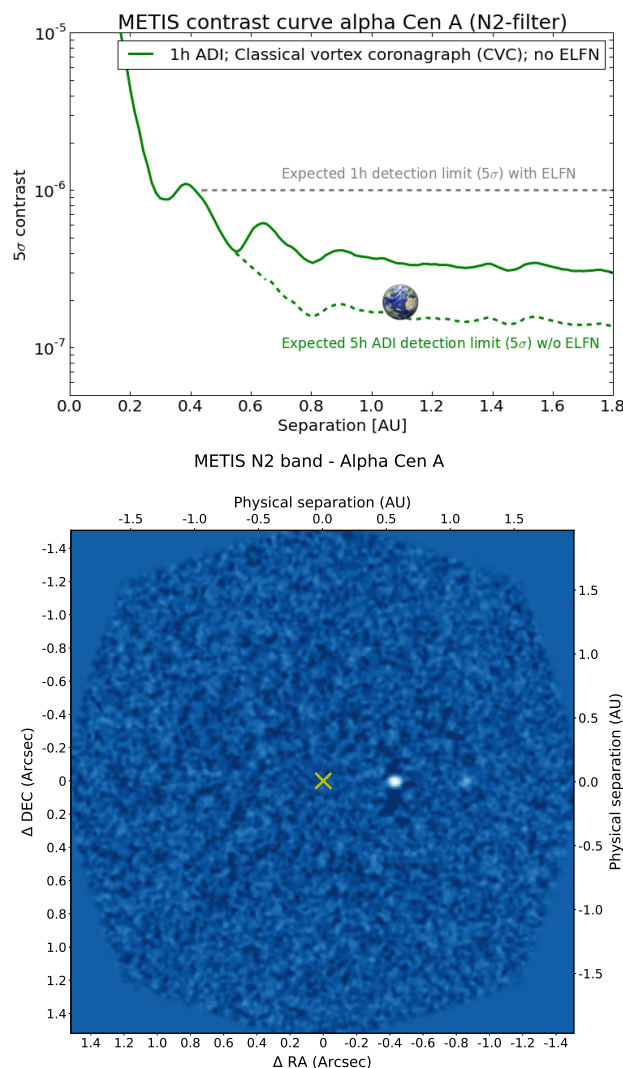
Figure 3-7: Feasibility study to investigate if METIS can detect an Earth-twin around α Cen A at quadrature. Given the higher luminosity of the star an Earth twin (i.e., same size and emission spectrum) would be located at $\sim$1.1 AU around alpha Cen A. Top: The green solid line shows the 5-σ contrast (in the N2 filter) achievable with the classical vortex coronagraph in a 1h ADI sequence according to simulations with the end-to-end METIS high-contrast simulator. These simulations assume an ELFN-free Aquarius detector. In this case a 5h ADI sequence would provide sufficient sensitivity to detect an Earth-twin as it is located in the background limited regime (green dashed line). With the ELFN the 1h detection limit would correspond to the grey dashed line and significantly longer integration times are required to achieve sufficient sensitivity to detect the planet. Bottom: Corresponding simulations (5h observing time; no ELFN) carried out with the METIS end-to-end high-contrast simulator. In this case, 2 Earth-like (i.e., Earth radius and albedo) were inserted, one at 1.1 AU and one at 0.55 AU. Both planets are detected with an SNR of 6.3 and 10.6, respectively.

it existed. With the currently baselined Auqarius detector this would require combining 5-8 nights of data to reach sufficient sensitivity. First tests to optimize the technology, observing strategy and data analysis (e.g., combining data from several nights) for high-contrast N band observations will be carried out in the context of the NEAR experiment in mid 2019 (Kasper et al. 2017).

In addition to the specific example of an Earth-twin orbiting α Cen A, we show in Fig. 3-8 the results from Monte Carlo simulations for the nearby stars α Cen A and B, Sirius A and Procyon A. These simulations are based on the Monte Carlo tool presented in Kammerer & Quanz (2018) which simulates planetary systems around a given set of target stars based on the statistics for planetary sizes and orbital periods derived from the Kepler mission. The planets' are randomly put on circular orbits and also their Bond and geometric albedo are randomly drawn from an allowed range of possible values. The host star's luminosity,
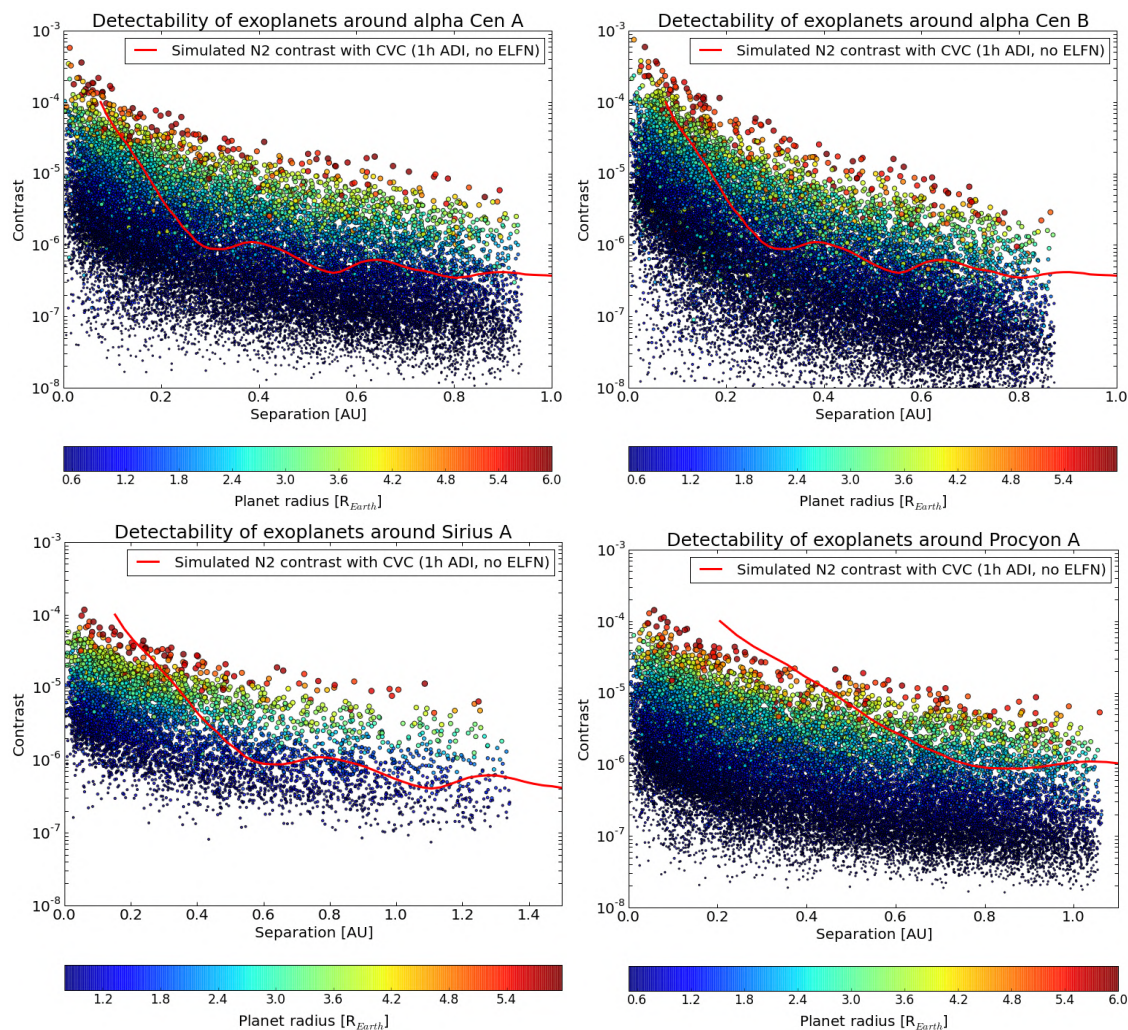
Figure 3-8: Monte Carlo simulations of 5000 randomly drawn planets orbiting nearby stars based on Kepler statistics (top row: α Cen A and B; middle row: Sirius A and Procyon A). 5000 randomly chosen planetary systems were created with radii between 0.6 and 6 R_{Earth}. The red curves are based on end-to-end high-contrast simulation with the classical vortex coronagraph in the N2 filter assuming 1h ADI sequence. ELFN is not taken into account, but the corresponding effect, as well as the effect of increasing the integration time, is illustrated above in Figure 3-7. The color of the points indicates the planet radius. As Sirius A is an A star the underlying planetary distribution is different than that of the other targets shown here (cf. Kammerer & Quanz (2018)).

the Bond albedo and the star-planet separation determine the planets' equilibrium temperature. Knowing the distance to the star and assuming black-body emission for the planets' SEDs the expected fluxes can be easily computed and compared with METIS' expected performance for senstivity and/or contrast. Figure 3-8 shows that for the selected group of very nearby stars deep imaging with the N2 filter allows for the detection of small, terrestrial planets in the background-limited regime, which can be reached at separations smaller than 1 AU in these cases (cf. Figure 3-7). The time it will take to achieve the required sensitivity will depend on the final choice of the N band detector.

At this point in time it is not known if any of the stars considered here does indeed harbor a terrestrial planet in the simulated parameter space and from follow-up studies of Kepler detections it is known that binarity (and all the stars above are members of binary systems!) seems to have a negative impact on the occurrence rate of (small) planets (Kraus et al. 2016). However, it is very exciting to know that there is a realistic possibility that METIS might be able to take a picture of a terrestrial planet orbiting one of the nearest stars to the Sun *if it exists* and in principle this planet could even orbit in the habitable zone. To what extent METIS might be able to detect terrestrial planets also in the L and M band, depends crucially on the final contrast performance, and is part of ongoing investigations.
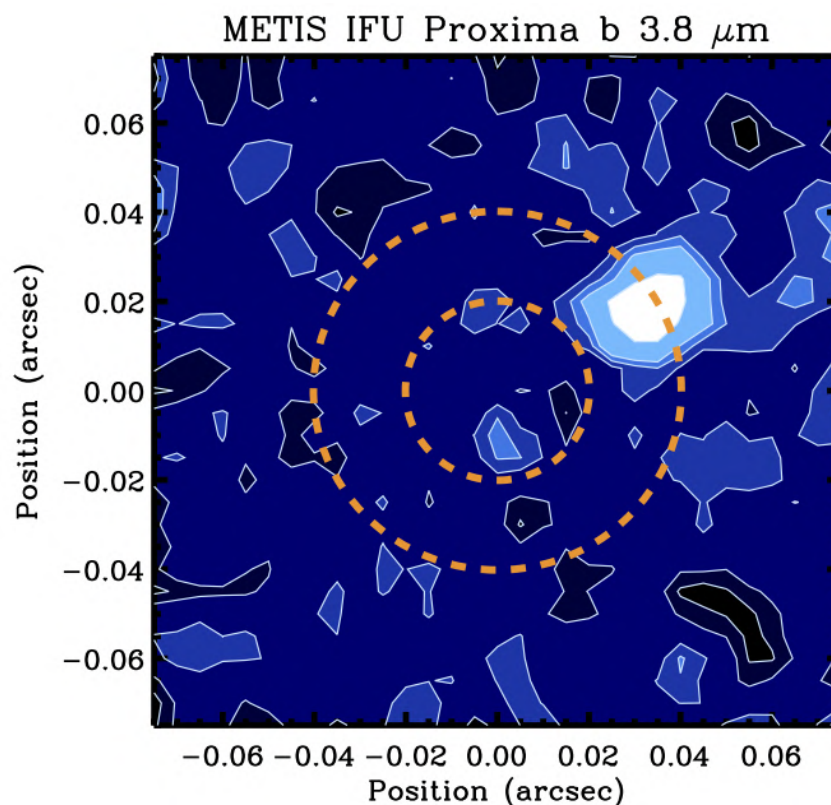
Figure 3-9: Simulations of the METIS IFU performance on the Proxima system at 3.8μm. Assuming a 1.1 R_{Earth} planet radius, 0.3 albedo, 50% illumination, and a achieved coronagraph-aided contrast of 1:500 at 2 λ/D, and 10 hours of observing time, the planet is clearly detected in reflected light.

In that context, METIS offers an additional interesting possibility: time differential, high-resolution spectroscopy has already shown to be able to separate out planet signals in the time and spectral domain at the 1e-4 level. As shown above, high-contrast direct imaging spatially separates planets at even more extreme contrast levels. Simulations show that the METIS IFU can combine these techniques and detect and characterize planets simultaneously in the time, spectral and spatial domain reaching contrast levels of 1e-9 or better bringing even the characterization of rocky planets around nearby stars within reach (Snellen et al. 2015). We illustrate with simulations of Proxima b in reflected light as shown in Figure 3-9. A planet with a radius of 1.1 R_{Earth} and an atmosphere identical to that of Earth is observed in the combined high contrast imaging, high spectral resolution IFU mode around 3.8 μm to clearly detectable significance in just 10 hours. Therefore, it becomes clear that METIS offers us the next step in planetary science - a ground-based mission to image the nearest world outside our Solar System. Such an image in the public mind may be comparable to Cassini's Pale Blue Dot looking back at Earth from Saturn, only METIS will be looking out to Proxima Centauri, perhaps making the first image of a far and distant but future home.

E-REP-ETH-MET-1014

4   THE FORMATION HISTORY OF THE SOLAR SYSTEM

4.1   Scientific background and context

The bodies in the planetary system were formed 4.6 billion years ago in an extended disk, and the formation took only a few ten million years. The physical conditions and the chemical composition of the planetary formation disk at that time is hardly constraint except that strong radial gradients in temperature and density are suggested, ranging from the inner edge close to the Sun, where the terrestrial planets originated, to the region of the gas giants, where the icy bodies like comets and Kuiper Belt objects accreted. The asteroid belt may represent the transition region between the terrestrial and icy environment in the disk. The physical and chemical processing of that formation disk material is at least partially reflected in the atmospheres of the planets and in properties of the most primordial bodies in the solar system that are accessible to observations today, i.e. in minor bodies like comets, asteroids and Kuiper Belt objects. Of particular interest here is how these objects connect to the Earth and its environment for the formation of life.

4.2   Scientific Goals

Scientific goals for the exploration of the formation era in our planetary system can be accomplished by:

- Establishing a composition and temperature profile of the planetary formation disk,

- Determining isotope ratios in cometary volatiles, namely the D/H ratio of cometary water as well as the ratios of $^{12}C/^{13}C$ and $^{14}N/^{15}N$, important elements in organic compounds,

- Constraining the large-scale radial mixing of material in the disk,

- Determining the ice composition and the organics in Kuiper Belt objects,

- Constraining the internal constitution of asteroids and comets by estimating thermal inertia of the bodies,

- Searching and estimating trace species in the atmospheres of the outer gas giant planets

It is also noted that despite the detailed view of space missions in the vicinity of planets, ground-based observations of atmospheric species of for instance Mars can provide the synoptic picture that is necessary for global modeling of the planetary atmosphere and that is essentially not achievable from spacecraft orbit.

4.3   Composition and temperature profile and isotopic ratios in the formation disk

The ices in comets are expected to reflect best the gaseous composition in the formation disk of the Sun around the time when the gas giants were formed. Sublimation of the ices when a comet gets closer to the Sun, releases volatile species. The richest wavelength domain for studies of these ice volatiles is the IR region between 3 and 5 μm (Cochran et al. (2015)). Using high-dispersion spectroscopy, a number of parent gas species from cometary ices including organic compounds can be measured from the ground, for instance H_2O, CO, NH_3, CH_4, C_2H_2, C_2H_6, CH_3OH, HCN (see Fig. 4-1). Beyond known molecules, emission lines from so far unidentified species are seen in high dispersion 3-5 μm spectra of bright comets. The Rosetta mission has identified further species of organic and inorganic nature (Altwegg et al. (2017)) that provide an so far unexplored sample of species for search and quantitative measurements using the high-dispersion spectroscopy option of the METIS instrument.
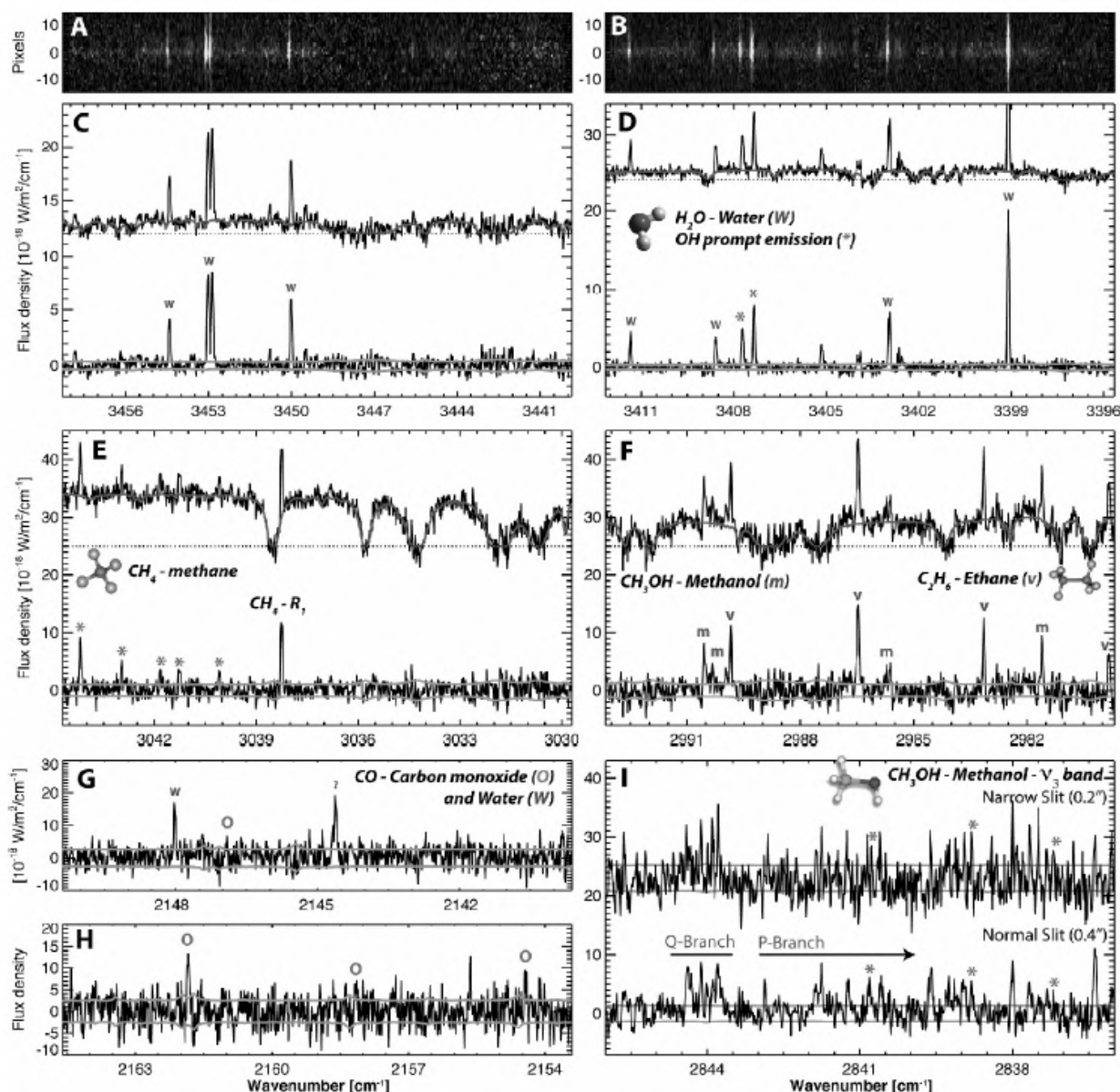
Figure 4-1: CRIRES spectra of the coma gases seen in comet 8P/Tuttle (Böhnhardt et al. (2008)). Panels A and B show examples of flux calibrated 2D spectra of the comet in the wavelength range of H_2O, panels C to I show extracted 1D spectra for various coma species (H_2O, OH, CH_4, CH_3OH, C_2H_6, CO; dust reflected sunlight removed) as indicated in the various subpanels. Panel G displays also emission (marked by symbol '?') from an yet unidentified species in the coma.

Considering evolutionary effects of cometary nuclei, the production rates of the known molecules allow to conclude on the ice composition in the outer planetary formation disk. Moreover, through the known sublimation temperatures, they provide a first, coarse idea on the likely temperature in the region where the respective comets were formed. A far better indicator of the temperature domain comes from measurements of the ortho-to-para ratios of parent molecules like H_2O and NH_3 (Mumma & Charnley (2011)) in the 3-5 μm region, since it allows determining the spin temperature of these species that is considered a good proxy for the formation temperature of the respective ices. Temperature models of the formation disk can then provide the link to the likely formation distance of the comet in the proto-planetary disk.

The radial profiles of both the gas composition and the temperature regime in the disk evolve from measurements of a statistically significant and also representative sample of short- and long-periodic comets. Here, over the past ten years, a starting point is already achieved through observations of a few, mostly

long-periodic comets from the Oort Cloud. However, progress is slow since the objects must be bright (for CRIRES at VLT brighter than 11 mag in K band) in order to be measurable with existing instrumentation and are thus rare. In particular, short-periodic comets are not well represented in the small sample of measured objects, which can only be overcome by the usage of a high-dispersion L and M band spectrograph like METIS at the ELT.

The same instrumentation is very much suitable to assess the isotopic composition of cometary ices using mostly the same wavelength region as for gas production rate estimations. Here, the D/H ratio in cometary water is of particular interest since it is suspected that terrestrial water may at least in parts originate from cometary impacts on the early Earth, for instance during the late heavy bombardment by likely Kuiper Belt objects when the Earth surface was already solidified. The existing D/H measurements (Mumma & Charnley (2011), Paganini et al. (2017)) provide a diverse picture that is best compatible with a mixture of impactors with different isotopic compositions and thus from different formation regions. Combining isotopic ratio values in comets not only D/H, but also $^{12}C/^{13}C$ and $^{14}N/^{15}N$ as important elements in organic molecules with compositional and temperature radial profile of the formation disk will allow addressing the question of isotopic enrichment and attenuation processes in the disk. The key contribution for the isotopic analysis can only come from measurements of more objects: In particular, short-periodic comets are difficult since they require mostly telescope with apertures larger than currently available.

Taking as reference the experience of observing programs on gas composition in comets using CRIRES at the VLT, one can expect of the order of one half to a full night duration per target of K=11mag objects (here referring to the brightness of the very inner coma of the comet) in order to achieve SNR of 5-10 in the dust continuum signal of the comet. The science goal requires a sample of 40-50 comets to be measured, of which about 15 are already done. The remaining 25-35 comets will have to be observed on an average pace of about 1-to 2 objects per year, the rate of comets that become within reach for the METIS AO system (limited to K=11mag), i.e. this program would last for about a decade or two. Moreover, due to their faintness Jupiter-family comets will be underrepresented in the achievable sample compared to long-periodic and Oort Cloud objects. For an AO system with limiting K magnitude around 15mag, an unbiased sample could be achieved in a much shorter time (since there will be a few comets within reach per night). Isotopic ratios require comet of total K=7mag brightness or brighter for which one can expect 1 object per year or two, observable for METIS at the ELT.

4.4   Large-scale radial mixing of disk material

The compositional mixing of gaseous species in the planetary disk follows from the above mentioned L and M band spectroscopy of gases in cometary comae. The solid, non-volatile component, namely the silicates, can be measured by N band spectroscopy at low resolution. A mixture of amorphous, space-weathered silicates and crystalline ones (Wooden et al. (2017)) were found in two long- and one short-periodic comet (Fig. 4-2). The parallel existence of amorphous and crystalline phases in cometary dust suggests that some of the silicates, i.e. the crystalline ones, may have been processed in a hot environment above melting temperature ($> 1500K$), most likely close to the Sun, just shortly before they got solidified and inserted into the cometary nucleus further away from the Sun. This scenario requires efficient radial mixing of material in the protoplanetary disk, a process that was initially not considered important in the formation scenario of our planetary system. At present, it is completely unknown to which extend the mixing took place and whether it affected the whole disk in a similar way.

Improvement of our knowledge will result from spectroscopic observations of cometary dust comae of a larger sample of comets in N band, an undertaking that given the relative faintness of most targets (in particular of the short-periodic comets) can be accomplished by a low-dispersion mid-IR spectrograph, i.e. METIS at the ELT. The situation is quite similar to the science case on gas and isotopic composition in comets (see section 4.3): required sample size is 40-50 of which about 5 objects have data measured. A comet of K=11mag for the inner coma will require about 1/2 to 1 night for low dispersion N band spectroscopy of the amorphous and crystalline silicate emissions of the cometary dust, i.e. sample completion
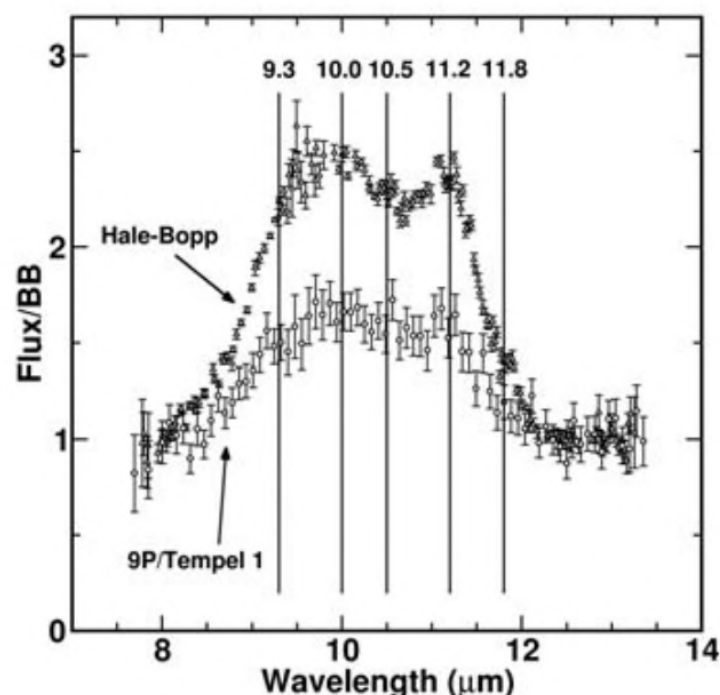
Figure 4-2: N band spectra of the dust comae of comets C/1995 Hale-Bopp and 9P/Tempel 1 (Harker et al. (2005)). The vertical lines indicate the presence of crystalline silicate grains (olivines and pyroxenes) in the dust comae of the comets, the emission shortwave thereof is produced by amorphous silicates. Dust grains collected at comet 82P/Wild 2 by the Stardust mission, showed examples of crystalline and amorphous dust components in the same grain aggregates.

depends on the availability of suitable targets with K=11mag or brighter and may need two decades or more. A fainter K=15 mag for the AO system will significantly speed up the program execution to about 5 to less than 10 years.

4.5   Ice and organics composition of Kuiper Belt objects

Kuiper Belt objects are considered building stones for the giant planets in the outer solar system. In particular, they are meant to have provided the volatiles of the atmospheres of the gas giants. Moreover, they may have contributed to the so called late heavy bombardment after the formation of the planetary system. During the latter period a significant amount of water and organics may have reached Earth via impacts of Kuiper Belt bodies (and comets), possibly scattered into the inner solar system due to the transient event of the 2:1 resonance passage of Saturn with Jupiter (Morbidelli et al. (2008)).

The ice and organics composition of Kuiper Belt objects is concluded mostly from low dispersion IR spectroscopy using existing large telescope facilities. In JHK bands various species like H_2O, CH_4, N_2 ices are found among the about 2-3 handful of objects measured so far, and a dichotomy between the large (like Pluto, Eris) and smaller bodies (radius below about 800km) in the belt is noted. Probably, the surface composition of the large objects is affected by rather recent and transient phenomena of atmospheric origin like re-condensation of ices from the vapor phase or aeolic transportation of surface material (Brown (2008)). The surfaces of smaller bodies on the other side seem only subject to space weathering and impacts.

Up to now, only a single object has the surface ice composition measured in L and M bands, i.e. Pluto-Charon. While Charon displays a unified water ice surface, Pluto itself shows a CH_4 ice dominated L band spectrum and an absorption around 4.6 μm that is tentatively identified as being due to CO ice and very likely Nitrile compounds and/or deuterated methane ice (Fig. 4-3; Protopapa et al. (2008)). The latter two interpretations have intriguing implications: It may either be the first indication of the existence of
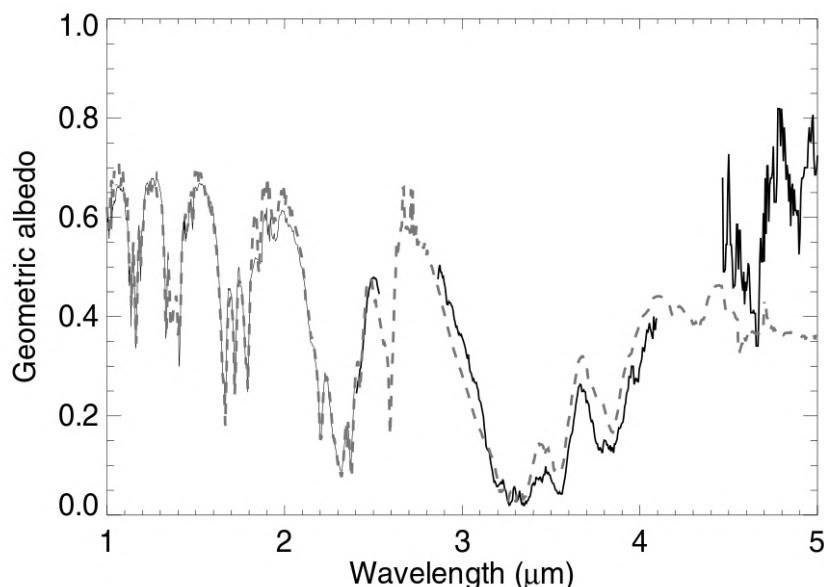
Figure 4-3: Near-IR spectrum of Pluto showing deep and wide absorption of methane ice on the surface of the dwarf planet (Protopapa et al. (2008)). The observed spectrum (continuous line) is a composite of a JHK band spectrum from the Keck telescope and a LM band spectrum from VLT. The absorption at $4.6\mu m$ is suspected to be produced by CO ice as well as Nitriles and/or deuterated CH_4 or both. The broken line shows the result of model calculations using a mixture of various surface ices including the mentioned species. Deviations from the observed spectrum beyond $3.5\mu m$ may indicated the presence of another, yet unidentified absorber material.

organic solids involving C-N bearing molecules in a Kuiper Belt object, i.e. of species that play a role in the formation of amino acids in space. Or it may allow for the first time measurements of D/H ratios in these objects that is out of reach for space missions like New Horizons.

Low dispersion IR spectroscopy with METIS at the ELT can open up a new domain for the surface exploration of Kuiper Belt objects. The task of *L&M* band spectroscopy will be the investigation of the presence of surface ices, namely (1) of the mixing of the expected abundant components like CH_4 (pure and diluted in N_2), CO, H_2O, (2) of organics components like Nitriles, and (3) of deuterated material like CH_3D. Of the order of 10 objects (Kuiper Belt members and relatives among the Centaur population) will become accessible for L and M band spectroscopy with ELT plus METIS, allowing to address at once the open issues of size-depending surface evolution of Kuiper Belt objects, of the presence of pre-biotic organic compounds and of the D/H ratio in ices at the edge of the known planetary system.

Since the objects to be measured (Kuiper Belt objects and Centaurs) are faint targets (V=13mag for Pluto), support of an AO system is considered a prerequisite for sensitive measurements in low dispersion spectroscopy mode of the L and M band of METIS. Long-duration appulses of the targets with bright enough background stars may open time windows of the order of one night for the anticipated measurements of a target. Alternatively, on-target AO are preferable provided that a sensitive AO system (about 16mag in K) will become available. then allowing also SNR improvements by extending the total integration time of the spectra to about 4 nights per target. In that case about 10-20 nights of ELT time will be required for the 5-10 targets within reach for this science goal.

4.6　Thermal inertia and the internal constitution of minor bodies

Continuous improvements in thermal modeling techniques allow meanwhile to estimate thermal properties of the surfaces of minor bodies from mid-IR photometry. The thermal emission of objects in Earth vicinity out to the asteroid belt and beyond peaks at mid-IR wavelengths and combined N-band (and Q-band, if available) measurements at different rotational phases over a range of phase angles are key ingredients for the determination of the thermal inertia of these bodies.
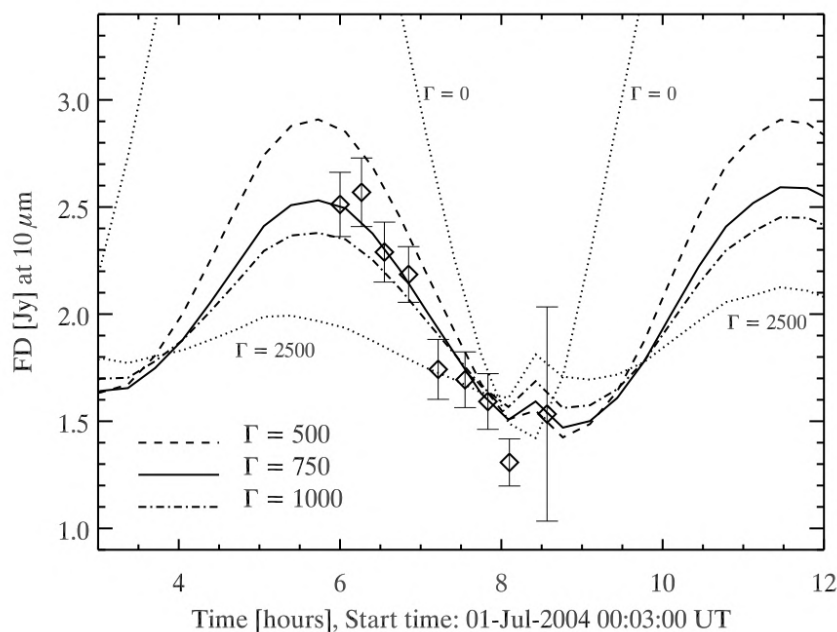
Figure 4-4: N band rotation lightcurve (diamond symbols) of asteroid 25143 Itokawa and thermal modeling results for various parameters of thermal inertia Γ (Müller et al. (2005)).

The thermal inertia of large, dust-covered main-belt asteroids is found to be very low, while monolithic bedrock objects have thermal inertia two orders of magnitude higher (Delbo et al. (2015), Scheeres et al. (2015)). Rubble-pile objects are expected to have values in between. Tidal forces during encounters with large bodies in the solar system cause regular reorganizations of such rubble piles (Richardson et al. (2002)), resulting in thermal properties, which are characteristic for a mixture of dusty and rocky surface regions. The approach of assessing the internal constitution of a body through its thermal inertia will also provide useful results for future interstellar visitors in the solar system like 1I/Oumuamua (Meech et al. (2017)) that may become observable more frequently for instance based upon LSST detections.

First indications on the internal constitution of a small body came from N-band observations at a 4m-class telescope (Müller et al. (2005)). The thermal inertia of 25143 Itokawa was found to be in the expected range for rubble-pile objects - which was later supported by results from the Japanese spacecraft Hayabusa when visiting this asteroid (Fig. 4-4). The principle capability of constraining the internal structure of minor bodies from the thermal properties is promising since it allows assessing the constitution of rather primordial bodies like cometary nuclei and C- and D-type asteroids as well as more evolved ones like S- and M-type asteroids. Related to this is the intriguing expectation that scenarios for the planetesimal formation in the proto-planetary disk as well as for the impact of the collision history on the body constitution may evolve. Both scenarios will then be constrained by observational results. The key point are accurate thermal measurements of minor bodies for which, given the faintness of the objects, N (and Q) band photometry with METIS at the ELT is required. It is noteworthy that for objects of 10 km and larger, surface resolved measurements will be possible. Terminator regions are of particular interest since they will allow very valuable refinements of the thermal and constitutional properties of the objects by measurement of the sunlit and the dark side of the bodies.

The detection limit of 0.1 Jy in N band at signal-to-noise of about 15 corresponds to a main belt asteroid diameter of order 20km. The observations require 3 filter settings in N band, each with about 2h integration time. I.e. the target needs one night of ELT time for the determination of its physical parameters size, albedo, thermal inertia. A sample of 100 objects covering different taxonomic asteroid classes and a wide size range (10 to several 100km) may be achievable for about 50 ELT nights, possibly including also several targets of km-size from the near-Earth asteroid population.
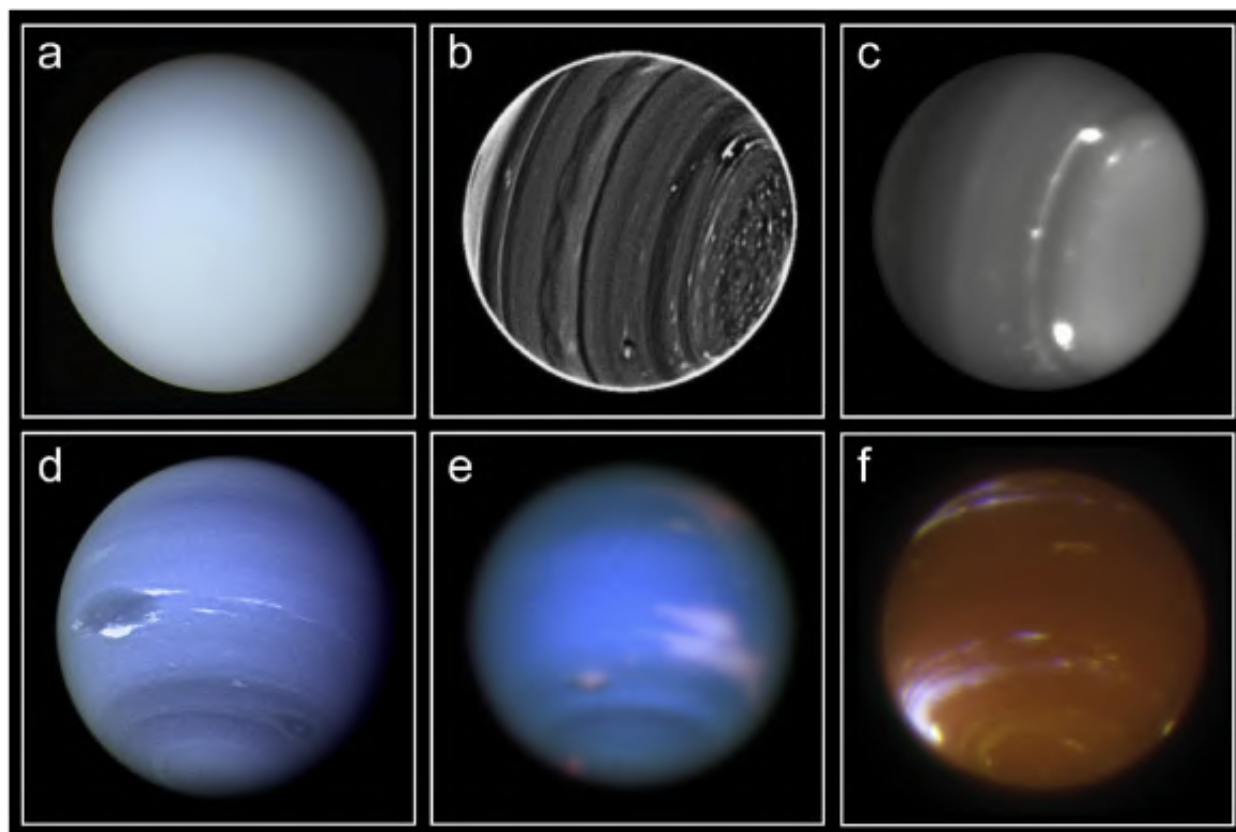
Figure 4-5: Uranus and Neptune - global views (Mousis et al. (2018)). Upper row Uranus: (a) visible from Voyager 2; (b) atmospheric structures in near IR (Fry et al. (2012)); (c) Bright near IR features (de Pater et al. (2014)). Bottom row Neptune: (d) visible from Voyager 2; (e) Visible with HST (image credits: NASA, ESA, and M.H. Wong and J. Tollefson from UC Berkeley); (f) near-IR (observations courtesy of I. de Pater).

4.7   Trace species in the atmosphere of Uranus and Neptune

The atmospheres of the giant planets are believed to be created from the small body population in the outer solar system. In parts, these bodies may have been collected by the planetary nucleus during the clean-up phase of the formation disk in its gravitational domain. In this respect they reflect the formation environment of the planet's neighborhood. Chemical reactions and mixing in the atmosphere and deeper interior may have altered the original composition (Lellouch et al. (2005), Orton et al. (2015)). Nonetheless, elemental abundances, in particular for the heavier species like phosphorus, should be unaffected. It is thus believed that elemental abundance in the giant planets can provide information on their interior and from those clues on their formation scenario.

PH_3 and CO, trace species in the troposphere of Uranus and Neptune, measured with high-dispersion in the 4-5 μm wavelength region, provide unique constraints on the internal mixing of these planets. Conclusions are drawn on the temperature domain of the planetesimals that created the atmospheric environment and brought in the molecule species when swallowed by the planet embryo from the surrounding planetary formation disk. Both gas giants, Uranus and Neptune (Fig. 4-5), are expected to be enriched in PH_3, but detection and measurement of this species was not yet successful. Since Uranus and Neptune will not be visited by spacecraft during the next decade or two, a challenging search and scientifically interesting detection option is left open for a high dispersion, high resolution spectrograph like METIS at the ELT.

A sensitive search for trace species in the two gas giants Uranus (V=8.3mag) and Neptune (V=9.5mag), using the high dispersion L and M band spectroscopy option of METIS at the ELT, may require 5h observing time for a single surface area under seeing limited conditions. Surface sampling may require repetition of the observations in about 4 locations. The total execution time for the trace species search is about 2 nights

per planet. It is noted that significant spatial improvement of the search will require AO corrections either during rare alignments of the planets with bright enough background stars or through a sensitive AO system that could make use of bright satellites of the gas giants, for instance of Ariel (V=14.5 mag, S=13 arcsec maximum separation from planet center) or Titania (V=14.0 mag S=30 arcsec) for Uranus and of Triton (V=13.5 mag, S=16arcsec) for Neptune.

4.8   The Martian atmosphere

The Martian atmosphere is the simplest possible example of a planetary atmosphere. It consists mainly of CO_2 with a few minor constituents (e.g. 2.7% N_2, 1.6% Ar, 0.2% O_2, 0.07% CO, 0.03% H_2O, 0.01% NO, 130 ppb H_2CO, 30 ppb O_2 and 10 ppb CH_4). The total pressure is 610 hPa and the scale height is 10km. The surface pressure is varying strongly, as due to the lower mass and gravity when compared to Earth, the Martian topography shows much larger excursions. Variation of the total pressure with time is characterized by minor seasonal effects.

As compared to Earth, understanding this atmosphere should be extremely simple, as there is no energy transport by ocean convection, hardly any by water vapor, apart from occasional dust storms, there are no clouds and there is no plate tectonics (Mangold et al. (2016), Villanueva et al. (2013)). Still the atmosphere of Mars is highly enigmatic, beginning with its sheer existence. Due to less gravity the atmosphere is much more weakly bound, and due to the absence of a magnetic field it is subject to the full erosion by the solar wind.

Mostly due to ground-based high-resolution infrared spectroscopy in the 3-5 μm range, many trace constituents could be constrained and e.g. for O_3, HDO and CH_4 high variability with time and location could be found, which, however, cannot be explained by present theory (Fig. 4-6). Explanations range from complex anorganic reactions on or below the Martian surface up to speculations about organic life. Apart from the highly spectacular explanation of the CH_4 origin or its variability involving organic life, the issue of understanding the Martian atmosphere is of extremely high relevance for climate research on Earth.

Observing the planet by an ELT with a diffraction limited beam ($\sim$ 25mas at $\lambda \sim 5\ \mu m$) will yield a spatial resolution of 7-10 km on Mars which is of order of the atmospheric scale height. This will enable limb observations of stable molecules or radicals in the Martian atmosphere, typically a factor of 100 amplified compared to an observation close to the sub-solar point. Molecules can now be observed in fluorescence without the thermal background radiation of the surface. As compared to the closer, more detailed, but very much localized spacecraft data, the telescopic observations can freeze the Martian rotation by measuring the whole limb in about 1h of observing time. Series of such observations to cover diurnal and seasonal variation will then lead to a new quality in the understanding of the chemical and photochemical processes. These observations will also allow us to constrain the 'erosion' processes of the Martian atmosphere and thus will lead to fundamentally new insights into the mechanisms that stabilize the atmospheres of all solar system planets (including the Earth).

Detection of the trace species in the Martian atmosphere from Earth (see for instance the CRIRES measurements of Villanueva et al. (2013)) is possible by sampling the planetary horizon at different latitudes within about 1h. For longitude coverage repetition (12 times or more) of the sampling is required. For the assessment of seasonal changes in the Martian atmosphere repetition of the whole monitoring observations is required (about 5 times). The challenges of these observations are the proper treatment of the high signal background from light scattered by the planetary disk and the best AO correction. For the latter the Martian moons Phobos and Deimos are available at 9 mag maximum K band brightness reaching maximum separation from the planet center of 25 and 30 arcsec, respectively. Alternatively, the planet horizon may be used (as was exercised with CRIRES at the VLT) for significant AO corrections. .
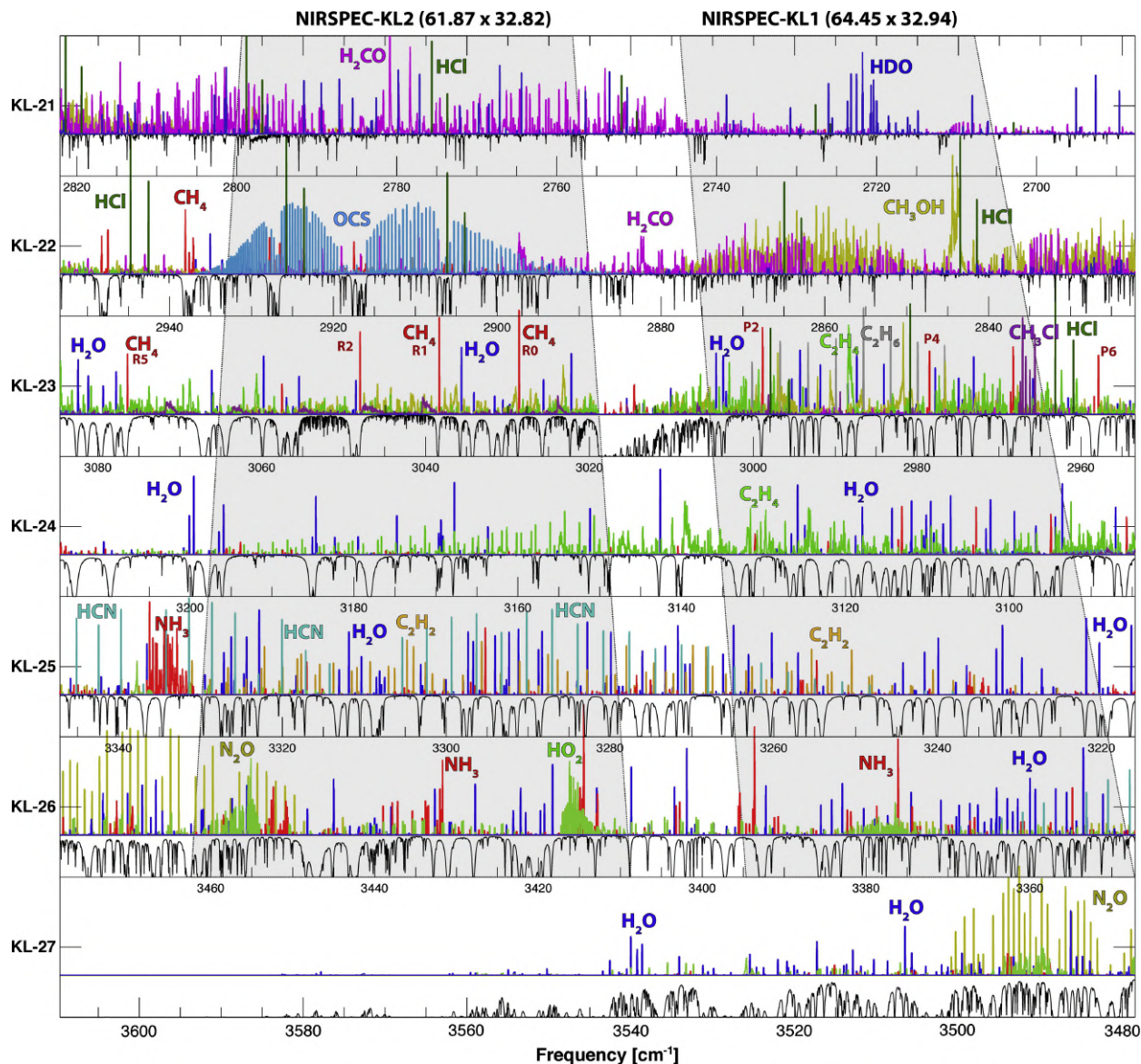
Figure 4-6: Trace species on Mars at infrared wavelengths (K and L bands) - simulation representing ground-based observations. Atmospheric transmittance from Mauna Kea (4200 m) is shown with a thin black trace. Grayed areas indicate the spectral coverage of the cross-dispersed NIRSPEC/Keck-2 KL1 and KL2 settings (Villanueva et al. (2013)).

5 MASSIVE STARS AND CLUSTER FORMATION

5.1 Scientific background and context

In many ways, massive stars (>8 $M_\odot$ and $>10^3$ $L_\odot$) shape the visible Universe. From the phase change of re-ionization (e.g., Bromm et al. 2009), to the formation of the trans-iron elements and the first solid materials in the early Universe (Dunne et al. 2003), as well as with their energetic sculpting of the interstellar medium, massive stars drive galactic evolution. High-mass stars also drive local feedback processes via O-star winds and supernovae. This feedback may trigger the formation of subsequent generations of both low and high-mass stars (e.g., Moore et al. 2007; Thompson et al. 2012), and also may contribute to the regulation of the star-formation efficiency (e.g., Elmegreen 2002; Dale et al. 2015). Understanding high-mass star formation is therefore fundamental to our knowledge of galaxy formation and evolution. Given this profound impact, it is crucial to understand the environmental conditions and processes involved in their

formation and the earliest stages of their evolution. Progress in understanding high-mass star formation lags behind the low-mass case, however. There are several reasons for this. Young, high-mass stars are rare and hence tend to be relatively distant. Most high-mass star-forming regions are located beyond 1 kpc and distances of 3 to 7 kpc are common. In addition, massive stars predominantly form in very opaque and highly clustered environments. A characteristic feature of massive star formation is that, in contrast to the low-mass case, the Kelvin-Helmholtz timescale for the onset of nuclear fusion is shorter than the accretion timescale. Thus the pre-main-sequence phase takes place deeply embedded within the dusty accreting envelope and the detection of the early phases of massive star formation mostly lies beyond the capabilities of optical and near-infrared instruments. Observations in the thermal infrared are far more suitable since the optical depth falls rapidly to longer wavelengths, and the spectral energy distribution of high-mass YSOs rises steeply in the mid-infrared (see, Figure 5-1). Consequently, thermal infrared observations at high spatial resolution are an essential means to study high mass star formation observationally.
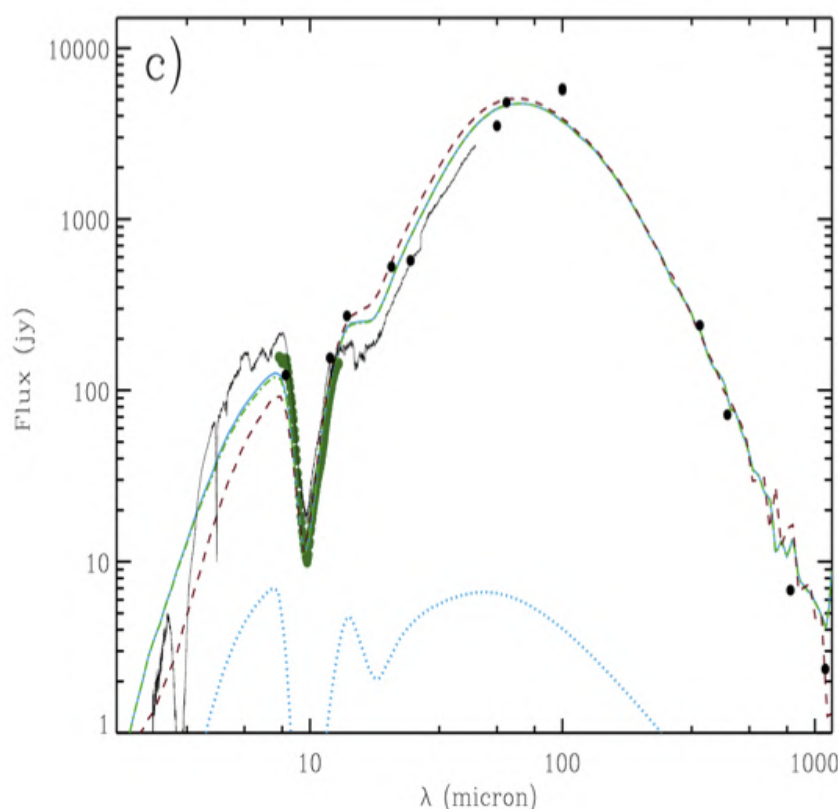
Figure 5-1: An example spectral energy distribution of a Massive Young Stellar Object. Most flux is emitted at mid- to far infrared wavelengths, and the object is extremely faint at wavelengths shorter than the L band. Figure: AFGL2136, taken from de Wit et al. (2011).

METIS on the ELT will answer key questions related to massive star formation. Its wavelength range and spatial resolution will provide the capability to penetrate high extinction columns, measure the spatial scales, and detect the spectroscopic tracers associated with massive star formation, resolving the cluster members within individual, IR-bright, massive young stellar objects (MYSOs) and their immediate environment, throughout the Milky Way. While ALMA will provide constraints on the physical conditions in the dense gas clumps from which the stars form, METIS will reveal the properties of the resulting protostars and clusters, at matching spatial resolution.

5.2   Science cases

5.2.1   Cluster formation and the universality of the IMF

There are theoretical arguments that the Initial Mass Function (IMF) in the early Universe should be weighted toward high mass stars (Bromm & Larson 2004). Early observational results seemed to support this, particularly to explain the evolution of IR and sub-millimetre galaxy luminosity functions (e.g., Lacey et al. 2008). However, this was subsequently put in doubt (Hayward et al. 2013). More recently, Conroy et al. (2013) presented evidence that massive elliptical galaxies exhibit bottom-heavy IMFs compared to that in the disk of the Milky Way (cf. Treu et al. 2010). While in most environments in which it is well measured, the IMF is invariant within the errors (e.g., Bastian et al. 2010), there are persistent suggestions that extreme environments such as the Central Molecular Zone of the Milky Way may produce top-heavy mass distributions (e.g. in the Arches cluster: Hosek et al. 2019). Understanding whether the IMF can vary is vital to the production of a predictive model of star formation and therefore to our comprehension of galaxy evolution and the star-formation history of the Universe. Some theories of massive-star and cluster formation (e.g., competitive accretion; Bonnell & Bate 2006; Bonnell & Smith 2011) require the latter to form already mass-segregated, i.e., high-mass stars form preferentially in the cluster centres. Experimental evidence for early-time mass segregation would not only constrain the sequence and therefore the process of star formation within clusters (high- or low-mass first or simultaneous) and hence the current models, but would also have fundamental implications for the general idea of a universal IMF on all scales. If the IMF can be position-dependent within a forming cluster then the latter principle will be shown to be invalid. Competing models, such as turbulent core formation, predict less fragmentation, more isolated MYSOs, and a different role for massive star feedback on environment and subsequent star formation (Krumholz et al. 2007). Observations of stellar clusters at visible and near-IR wavelengths show mass segregation, which is probably due to dynamical evolution on short timescales (Allison et al. 2009), so we need to probe the earliest possible evolutionary states to determine the primordial mass structure in clusters. ALMA results have produced mixed results on the mass function of the clumps in proto-clusters, e.g., apparent simultaneous formation of low and high masses but with relatively few low-mass clumps (Cyganowski et al. 2017), only low-mass clumps (Zhang et al. 2015; Sanhueza et al. 2017), and a mass function consistent with a standard IMF (Cheng et al. 2018). A key science project for METIS on the ELT, possibly in conjunction with, e.g., MICADO, is therefore to image the youngest embedded, IR-bright clusters within massive Galactic star-forming regions with sufficient spatial resolution to separate the individual young stars and measure the radial dependence of the luminosity function (see, Figure 5-2 for an example image). Using a sample of such regions, it would also be possible to search for variations in the star-formation rate and efficiency, vital inputs into semi-analytic models of galaxy formation and evolution, and determine the fraction of stars harboring circumstellar disks as a function of cluster age, mass and/or density.

For typical molecular gas densities and temperatures in massive star-forming regions, the Jeans length is of order 0.01 pc. This is equivalent to 0.2" at 10 kpc, requiring the spatial resolution of METIS to resolve the still-embedded members of young clusters, prior to significant dynamical relaxation and consequent mass segregation. ALMA observations of the pre-stellar stages of star formation are probing spatial scales of this order (e.g., Tan et al. 2013; Cyganowski et al. 2017). At comparable spatial resolution, METIS will measure the luminosity functions of embedded sources from 3 to 13 μm. Although coarse as a tracer of individual stellar masses via IR luminosities (estimates are good to within a factor of 2-3), thermal IR observations will enable the characterization of the full stellar populations down to sub-stellar masses observed through dozens of magnitudes of visual extinction. By studying multiple young clusters within 10 kpc of the Sun, we can then search for variations as a function of Galactocentric radius and the known radial variations in, e.g., metallicity, pressure, radiation field, and in unique environments (e.g., molecular ring, Galactic centre, sites of triggered star formation), representing a wide range of star-forming sites also relevant to other galaxies. Further, using multi-band photometry and low- to medium-resolution imaging spectroscopy, we can study gradients in the properties of barely resolved, but deeply embedded, massive clusters in the local group. While more evolved star clusters will be better studied in the near-infrared, many of the youngest ultra-

compact HII regions, most closely connected to their initial conditions of formation, will only be visible in the mid-IR. Pioneering studies of distant barely resolved embedded regions in the Milky Way conducted with the VLT can be extended with METIS to the LMC/SMC and perhaps M33, opening up unique studies of the IMF and star formation in diverse galactic environments. In the confusion-limit, METIS will be able to probe embedded star clusters in the local group not accessible with JWST.
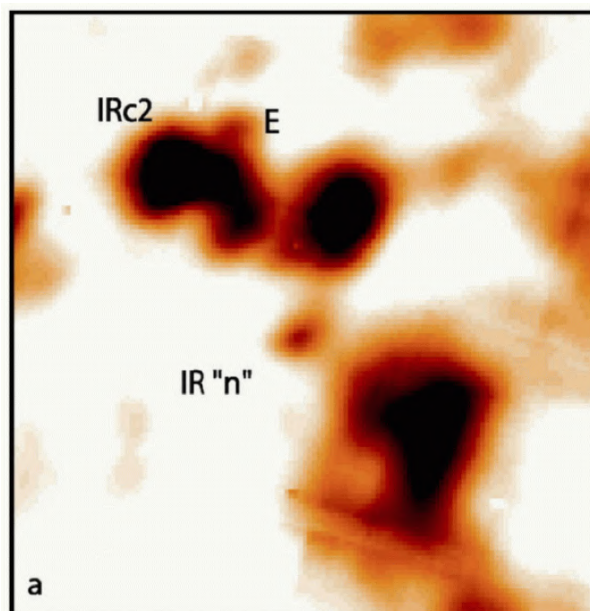
Figure 5-2: Keck telescope image of the KL region in Orion at 12.5 μm (Shuping et al. 2004). which breaks up into emission features caused by several embedded protostars. The cutout size is 10"×10". At 414 pc, Orion is the closest site of massive star formation but most of such regions are several kpc away. If we put Orion at a typical distance of 4.0 kpc, all the fine structure in this image would be contained within a 1" × 1" area.

5.2.2 Mapping the immediate environs around massive YSOs

Although theory (e.g., Zinnecker & Yorke 2007) and numerical simulations ((e.g., Kuiper et al. 2010, 2011; Rosen et al. 2016) suggest that high-mass stars may form by disk accretion, observational evidence for the existence of such disks, especially at smaller scales, remains scarce. Only recently, direct evidence for Keplerian rotating, flattened structures at sub-arcsecond scales has started to emerge (Johnston et al. 2015; Ilee et al. 2016, Zapata et al., in press), all based on mm data. The observations indicate the existence of long-lived large-scale, 100s to 1000 au, cool circumstellar disks, but the inner, hotter, accretion regions and the bases of outflows could not be revealed at these wavelengths. Radio interferometry (Shepherd et al. 2001; Reid et al. 2007) as well as MIR interferometry (Linz et al. 2009; Kraus et al. 2010; de Wit et al. 2011; Boley et al. 2013) also suggest that potential disks around several massive young stars have diameters smaller than 100s of au. Indeed, Frost et al. (2019, MNRAS submitted) are the first to find evidence for a disk with a cleared inner hole of 60 au in their MIDI interferometric data. This discovery provides intriguing evidence for transition disks around massive stars in analogy to lower-mass stars surrounded by forming planets. However, the mid-infrared interferometric studies are limited by sensitivity to only the brightest nearby sources, while extensive mapping of the uv-plane for the sources is prohibitively expensive and will remain so also with the next-generation VLTI instruments like MATISSE. A further complication is that any interferometric observations are constrained to the brightest objects only, and therefore studies are mostly limited to single objects. METIS will allow us to study a large sample of objects, moving away from the anecdotal and start studying statistically meaningful samples, such as the RMS survey that produced a catalogue of 100s of MYSOs, and is complete in the Galaxy for mid-IR bright MYSOs of 15 solar masses and higher (Lumsden et al. 2013). With METIS, we will be able to resolve the disks at sub-100 au scales, even for objects several kpc away, and begin to determine the structure of such disks and their

embedding into the envelope material. An additional bonus arising from these imaging observations is that close companions can be detected at high contrast ratios. Although the majority of massive main sequence stars are in binaries, with significant implications for their further evolution (Sana et al. 2012), the origin of multiplicity in high-mass stars is still unclear. Given that dynamic effects may alter the proto-binaries properties, we need to observe stars in their early phases to obtain observational constraints on binary star formation scenarios (e.g., Meyer et al. 2018; Lund & Bonnell 2018). Until recently, we hardly knew anything about the binary properties of MYSOs, with studies being limited to serendipitous detections of binary MYSOs at separations of 50 -100s of au and larger (e.g., Beuther et al. 2017; Kraus et al. 2017). Dedicated surveys had been lacking, A recent survey (Pomohaci et al. 2019) used adaptive-optics-assisted near-IR imaging and found a binary fraction of 30% in the 400 to 40,000 au range, suggesting a very high overall multiplicity. The next step is to complete the parameter space at smaller separations. Next to radial-velocity studies probing the closest sources, high-contrast METIS imaging will be excellent to fill the gap between RV studies, and 8m class images. Utilizing the powerful thermal-infrared imaging of METIS with a 39-m telescope, we finally can observationally address mechanisms to circumvent the radiation pressure problem for the infalling matter onto the central regions. Theorists have proposed outflow cavities, optically thick disks, and/or Rayleigh-Taylor fingers to reshape the radiation field and to beam it away from the bulk of the incoming matter (Tan et al. 2014). With the high spatial resolution imaging we will be able to look for such structures at the locations where they matter most for the accretion process: within the innermost hundreds of au. This will put us in a position to better assess the current and future numerical simulations of massive star formation (see, Figure 5-3). ALMA and EVLA will also make significant steps in the study of circumstellar structure (e.g., Krumholz et al. 2007), but sub-mm and cm-wave molecular lines trace mostly the low and intermediate temperature regime appropriate to cool outer-disk regions, pre-stellar objects, and more extended cloud cores, but will provide little information from the inner accretion. METIS, thanks to its high-dispersion IFU mode in the thermal infrared, is complementary to such facilities, rather than competing. Both approaches are needed to obtain a complete picture of the disks around massive YSOs.
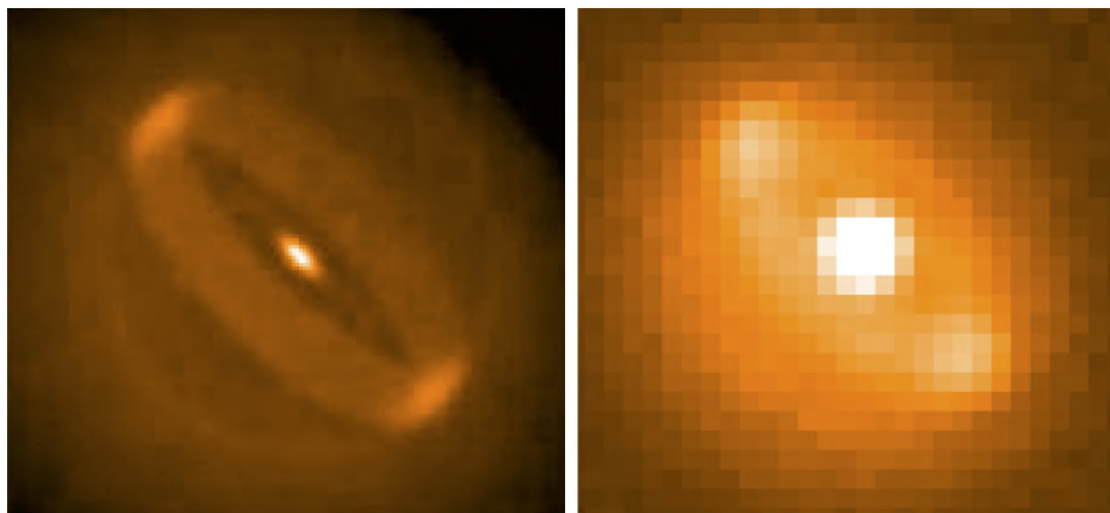
Figure 5-3: Left: Model image of the circumstellar environment of a MYSO which reproduced the limited uv-coverage MIDI data and the spectral energy distribution (de Wit et al. 2011). Right: How the object would look like using the ELT. Image computed using the METIS simulator. The image is about 0.25 arcsecond on a side

5.2.3   Physical conditions in the massive YSOs

The benefit of L and M band capability in METIS is twofold. At 3 - 5 μm we trace the hotter material close to the heating sources, which is of special interest when exploring mass transfer onto the central objects and in constraining parameters of continuum radiative transfer models. This is important since the number of free parameters increases drastically when going from one-dimensional models to 2D- or

even 3D-simulations (e.g., Indebetouw et al. 2006). Furthermore, the L and M bands contain important spectral lines and ice features, which provide data on disk structure and kinematics. Keplerian rotation is the ultimate evidence for a disk. In this wavelength range, both gaseous and solid-state CO can be detected, the former arises in the inner, warm disk regions (e.g., Blake & Boogert 2004b). Goto et al. (2006b) have spatially resolved the CO emission of the disk of a Herbig Ae star at 100 pc by means of AO-assisted high-resolution spectroscopy. However, in young massive stars, the spectra are dominated by more or less strong CO absorption lines. In order to disentangle these lines from CO emission, a resolution R>25000 is mandatory, and 50,000100,000 is ideal. Furthermore, one often has to resort to the line series of the weaker CO isotopologues in order to make a meaningful excitation analysis. Hence, the combination of high spectral resolution and large collecting power of ELT/METIS is mandatory for this research.

The Pfund-β and Brackett-α lines are also covered by the LM bands. These can arise in accretion flows or in a disk wind where the intense radiation from the YSO drives mass loss off the surface of the inner parts of its disk (Drew et al. 1998). Their emission-line profiles and line ratios when computed as function of wavelength already provide indirect evidence for the geometries involved (Lumsden et al. 2012; Pomohaci et al. 2017). However, spatially resolving these line-forming regions with METIS would be a breakthrough for investigating the dynamical structure of the interiors of the youngest massive YSOs, which are too deeply embedded to use near-infrared recombination lines.

Finally, with medium spectral resolution, the ices around massive YSOs can be studied, providing information on the outer disk structure, the composition and thermal history of the ice. Figure 5-4 gives examples for M-band spectra of massive YSOs and indicates important spectral features that are of interest for METIS spectroscopy.
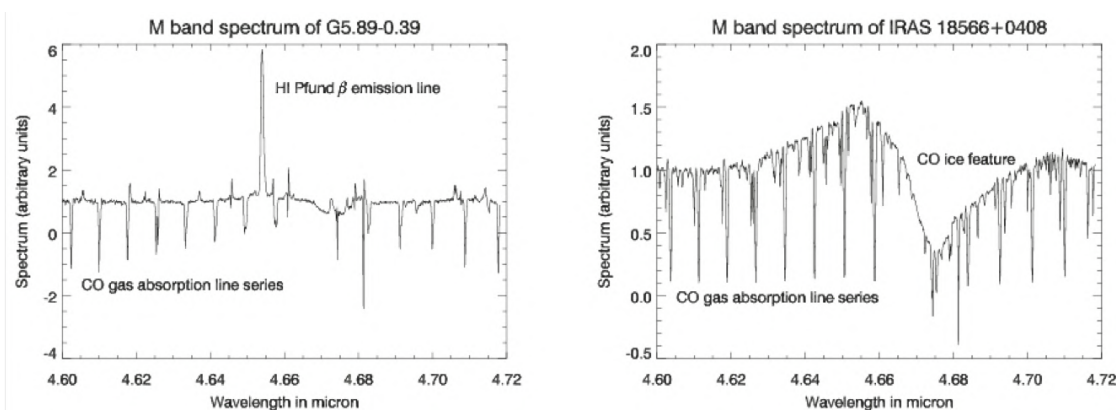
Figure 5-4: Examples for M-band spectra of massive YSOs. Left: The UCHII region G5.89-0.39; Right: The high-mass protostellar object IRAS 18566+0408. The most important spectral features accessible with METIS are labelled.

5.2.4   Accretion disks around massive YSOs

A major uncertainty concerning the formation of massive stars is how stellar mass is built up through accretion. This requires observations at the smallest possible scales to enable studying the accretion onto the star. A Keplerian circumbinary disk has been seen in the hot-core tracer CH_3CN at 0.4" resolution in G35.2-0.74 with ALMA (Sánchez-Monge et al. 2013). Evidence for a disk in this source was also seen in the 2.3-μm CO overtone bands by (Ilee et al. 2013). However, given the small scales involved, it is very hard to directly image the accreting material at inner disk radii. Spectro-astrometry, however, is able to measure the photo-center of a spectrum at sub-pixel scales, and both spectrally and spatially resolved spectra allow us to study the inner parts of the circumstellar disks and material. Here, METIS with its IFU for the L-M-band range will make 2D spectro-astrometry possible, a powerful extension of the original technique that has already been pioneered recently for some MYSOs (Davies et al. 2010; Murakawa et al. 2013; Caratti o Garatti et al. 2016, using IFU spectroscopy or using differential phases in VLTI;). Combining

such data with sophisticated models will allow us to derive the relevant astrophysical parameters (e.g., Wheelwright et al. 2012, Figure 5-5). Sub-milliarcsec scales have been probed with existing facilities and with METIS micro-arcsec precision can be achieved. This will render disks around a large sample of MYSOs available for study in various atomic (such as hydrogen recombination) and molecular (e.g., CO at 4.6 μm) lines. This will provide direct evidence for direct disk accretion for the formation of massive stars (see, e.g., Pontoppidan et al. 2011b), leading to measurement of accretion rates and key tests of rapid- and accelerating-accretion models of high-mass star formation (e.g., McKee & Tan 2003; Hosokawa et al. 2010).
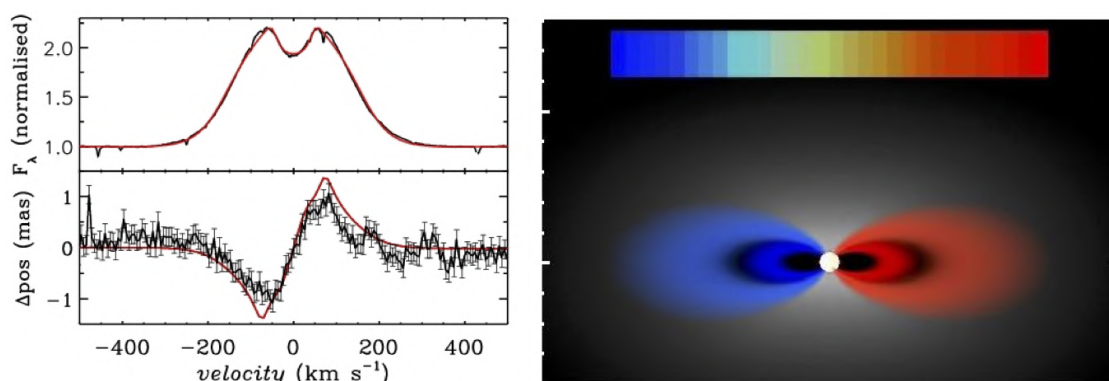
Figure 5-5: Left: Example spectro-astrometry of the Hα emission line of a Be star. The top panel shows the intensity spectrum, the double peaked profile indicates the presence of a rotating disk. The lower panel shows the offset of the light from the various parts of the disk. As can be seen from the right hand panel, the blue-shifted and red-shifted emission arise from opposite sides from the star. The solid line shows the fit from a 3D non-LTE model (Wheelwright et al. 2012). The precision in the positioning of the photo-centre is at the sub-milli arcsec level, with METIS, micro-arcsecond level should be reachable.

6   EVOLVED STARS AND THEIR CIRCUMSTELLAR ENVIRONMENT

6.1   Scientific background and context

The final evolution of low- and intermediate-mass stars is a rapid transition from the Asymptotic Giant Branch (AGB) over the post-AGB transit towards the Planetary Nebula Phase (PN), before the stellar remnant cools down as a White Dwarf (WD). In these late phases, it is the external mass-loss that governs the stellar evolution and one of the key ingredients is that in the cool circumstellar envelope (CSE) of AGB stars, dust grains are formed. It is well known that this accumulated mass-loss of lower mass stars is one of the major contributions to the ISM enrichment in gas, dust and chemical species like C, N and the s-process elements beyond the iron peak. This recycling of gas and dust between the ISM and stars is one of the strong evolutionary drivers of a galaxy's visible matter and its chemical and spectral characteristics (see e.g. Meixner et al. 2006; Gordon et al. 2011; Zhukovska et al. 2016; Kobayashi 2018).
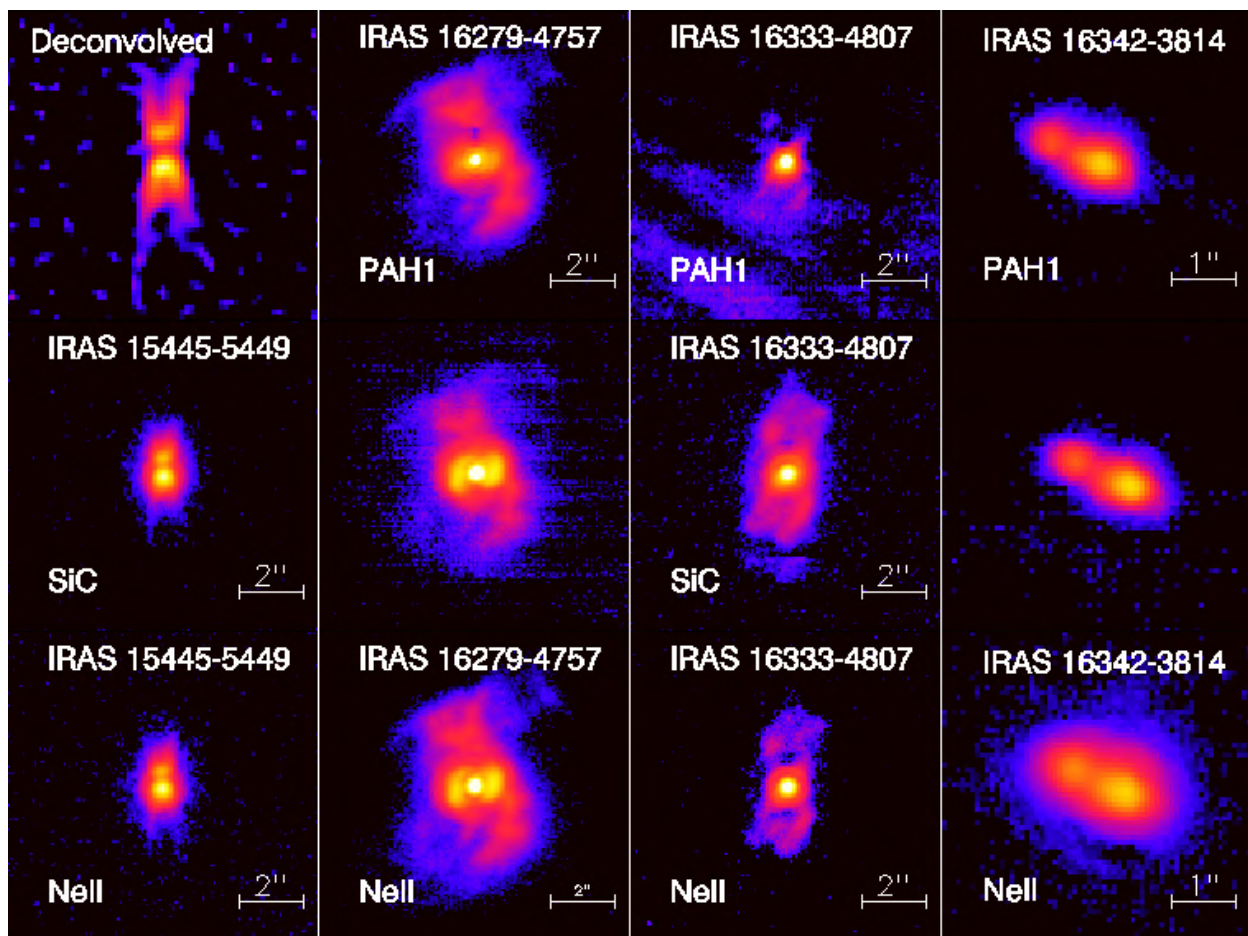
Figure 6-1: A small sample of mid-IR images of evolved objects obtained with the VISIR instrument on the VLT. Out of 96 objects observed in this survey, roughly 20 were spatially resolved, i.e. a few objects per evolutionary class (e.g., AGB, post-AGB, PN) (Lagadec et al. 2011).

Although the scheme of the late phases of low-mass stellar evolution may be generally acknowledged, there is no understanding from first principles of the mass-loss process and models still rely on many, rather ad-hoc assumptions. These important processes cover a wide range of scales, from the micro physical levels up to much larger scales, where poorly understood driving and shaping mechanisms work on the whole circumstellar envelope. On the micro scale, the chemical and physical processes in the interface region between the photosphere and the dust forming layers are crucial to generate a dust-driven wind (e.g. Nowotny et al. 2005; Bladh & Höfner 2012; Bladh 2018). In this region, a complex interplay between

non-equilibrium gas-gas and gas-dust interactions are strongly dependent on the local chemical and ther-modynamical conditions. Illustrations of our poor knowledge of this crucial part in the mass-loss process are legion. Oxygen-rich stars, for instance, suffer from the "acceleration deficit" dilemma, which states that predicted mass-loss rates due to the formation of silicate dust alone are orders of magnitude smaller than observed ones (Woitke 2006; Höfner 2008) demonstrated that Fe-free silicate grains of sizes larger than 0.1 μm may drive a wind and grains of this size have been detected by Norris et al. (2012).

The detection of AlO in the oxygen-rich mass-losing stars (Tenenbaum & Ziurys 2009; Decin et al. 2017) indicates that small amounts of metal oxides in the gas-phase form and survive the condensation phase of solids (Kamiński 2018), despite their key role as precursors in the nucleation of dust grains (e.g. Tielens 1990). However, the exact path for the formation and growth of oxygen rich grains is still a matter of ongoing research (e.g. Gobrecht et al. 2015). The formation of C-rich dust is better understood, but also here several uncertainties in the chemical paths exist (Cherchneff 2012). Tracing the molecular "left-overs" of dust formation can thus give crucial hints as to which path leads to carbon and silicate dust at which distance from the star.

On larger scales, our understanding of the processes driving and shaping the whole CSEs, is also very lim-ited. This is in part due to the high spatial complexity of many of these structures, as illustrated abundantly by the optical images of PNe in scattered light and in nebular optical emission lines by the Hubble Space Telescope (e.g. Balick & Frank 2002; Sahai et al. 2011). For the nearest ones, the thermal emission of the dust component is also resolved with current infrastructure. Also cooler post-AGB stars or proto-planetary nebulae (PPNe) display a surprisingly wide variety in shapes and structure in thermal emission as well as in scattered light (Figure 6-1). This was not expected since the major shaping was thought to occur when the central object is hot enough to generate a fast wind. Clearly shaping mechanisms are at work even very early after the AGB evolution (e.g. Maercker et al. 2012; Ramstedt et al. 2014).

The major discussion topic in the PNe community is the growing evidence that our view of the Planetary Nebulae physics is in fact dominantly determined by processes only relevant in binary stars (e.g. De Marco 2009; De Marco & Izzard 2017). Binary transition objects do contain bound Keplerian disks (Bujarrabal et al. 2013, 2015), the structure of which resembles protoplanetary disks around young stellar objects (Van Winckel 2018). It is now acknowledged that these disks must play a leading role in the evolution of the systems.

Progress on the observational side is now very prominent with ALMA (e.g. Ramstedt 2018), on one hand, and with IR interferometry and adaptive optics (e.g. Lagadec 2018) on the other. The present day inter-ferometers at CHARA (Center for High-Angular Resolution Astronomy) and/or the VLTI (ESO) allow efficient image reconstruction thanks to the 4 to 6-beam combinations. The MATISSE instrument at the VLTI of ESO which is under commissioning now, will certainly bring progress on high-spatial resolution science, but the stringent flux limit on the correlated flux, will remain an observational challenge. The con-clusion of these efforts is that symmetry breaking of the spherical winds occurs very early after the AGB, but the major driving forces remain unclear.

The combination of superb sensitivity, high-spatial spatial resolution and high-spectral resolution of METIS at the ELT is crucial to address the research goals presented in more detail in the following sections. The spectral resolution is needed to resolve the kinematics of the circumstellar material and study the isotopic ratios, which are ideal probes, not only for the AGB nucleosynthesis, but also for the nucleation processes in the circumstellar envelopes and disks. The full N-band spectra will allow us to study the mineralogy of the hot dust component and, for the nearest objects, resolved spectra will allow us to probe the radial dependence of the grain characteristics as well as the detection of density inhomogeneities like rings and spirals.

6.2   Scientific Goals

6.2.1   Molecular envelopes of evolved stars

Systematic studies of winds around evolved stars include (sub-)millimeter observations of molecular lines, IR spectroscopy of dust emission and molecular lines, and observations of atomic or molecular resonance scattering of photospheric light in the shell. Rotational emission lines of molecular species probe the intermediate and outer wind envelope, beyond 30 stellar radii (e.g. Habing & Olofsson 2003). Non-equilibrium chemistry models predict complex molecules to be formed close to the star, which are subsequently ejected in the outer wind as "parent" molecules Cherchneff (2012); Gobrecht (2018). A current limitation for testing these models is that the thermo-physical structure close to the target is not well constrained. Using high-resolution IR spectroscopy of rotation-vibration lines and observing scattering resonance lines along the line of sight through the envelope (Decin et al. 2007, 2010; Smith et al. 2009a; Ohnaka 2014; Hron et al. 2015; Ryde et al. 2015) offer interesting possibilities to explore the thermo-physical, spatial and chemical structures in this inner envelope. The approach has been tested using the high- resolution Phoenix spectrometer on the Gemini South telescope for the oxygen-rich AGB star R Hya (Figure 6-2). The slit was placed at different position angles to image the circumstellar envelope around the star. The intensity of the measured CO rotational- vibrational lines clearly decreases with distance to the star, consistent with a symmetric wind. The fact that the NW, NE, and SE intensities lie above the mean, while the SW, ES, EN, and WS lie below may suggest a bipolar structure, stretching from NW to SE. To investigate this idea, one needs a high-resolution IFU to map the inner wind structure.
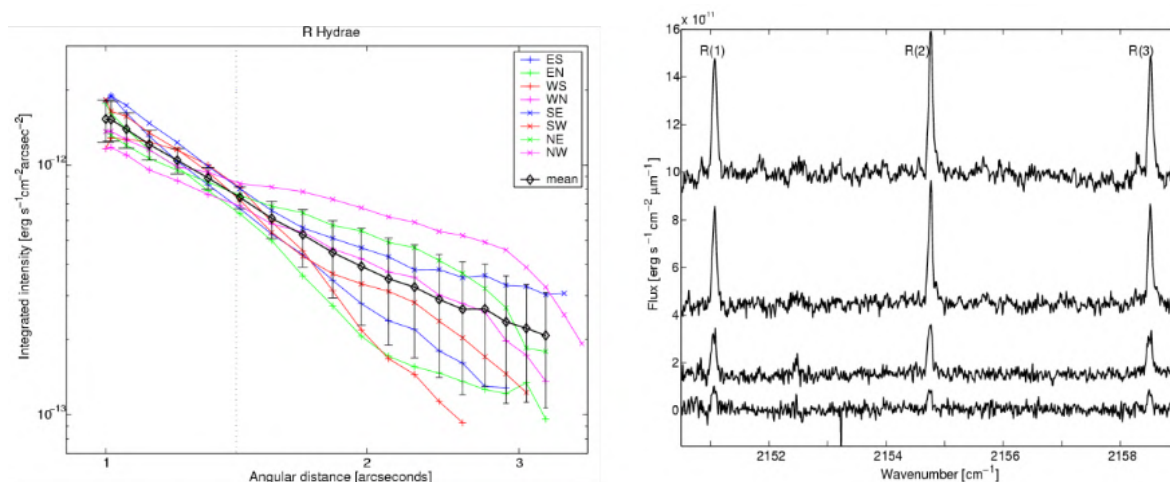
Figure 6-2: Left: The set of CO emission spectra at the east-position from R Hya. The spectra are shifted vertically for reasons of clarity. The top spectrum is measured closest to the star, i.e., at 1". The subsequent spectra are measured at 1.1", 1.6" and 2.4" from the star. Right: The CO line intensity of the circumstellar emission as a function of the angular distance from the star (R Hya) for eight scan directions, and the mean (Decin et al. 2008).

Also, MIR spectroscopy permits the observations of molecules that form in the region that is levitated from the photosphere and whose abundances "freeze out" during the dramatic density drop at the dust formation locus and/or which are depleted onto dust grains. An example for the inner envelope for a prominent AGB star is shown in Figure 6-3. METIS will map the inner wind structure for different molecular species and transitions, thus providing pivotal input in studying stellar mass loss, and in particular high-resolution L and M-band IFU observations are crucial to understand the complex inner wind zone of AGB stars. In comparison with ALMA, MIR spectroscopy gives efficient access to a large number of lines with widely different excitation conditions. Several crucial questions will be answered with the help of METIS:

- What is the structure of the velocity fields in the complex envelopes? Answers to this question can be achieved by spatially and spectrally resolving gas lines, many of which are expected to exhibit P

Cyg profiles or even inverse P Cyg profiles in their absorption and emission portions. Line confusion may be a serious problem that is best met with high spectral resolution.

- What is the density and thermal structure in the envelopes? Various molecules (e.g., CO, H_2O, C_2H_2, CH, SH, HCl, SiO, OH, CO2, CS, CH, HF, NH, NO, C3) are ideal thermometers and barometers to trace the density and thermal structure in the envelope. The L- and M-bands, accessible with METIS at high spectral resolution, are rich in lines of these molecules. CO, H_2O, C_2H2, SiO, CH, HCl and OH are of particular importance due to their abundance or relevance for the chemistry and dust formation.

- What are the details of nucleosynthesis and the neutron source driving the s-process in AGB stars, and the dredge-up efficiencies enriching the outer atmospheric layers with nuclear yields? Several isotopologues can be studied to derive the interesting isotopic ratios such as $^{1}2C/$ ^{13}C, $^{16}O/^{17}O$, $^{16}O/^{18}O$, $^{24}Mg/^{25}Mg$, etc. to refine our insight into the nucleosynthesis and mixing in evolved stars and their impact on the chemical evolution of the Galaxy.

- What is the chemistry in the inner envelope of AGB stars? Thanks to the IFU, we will be able to image the inner wind structure and hence measure the line intensities (and abundances) as a function of radius from the photosphere. Thus, we will provide direct measurements of the depletion and freeze-out processes of the different species, and we can study the effect of pulsation-induced shocks, the extent of inhomogeneities, the onset of shaping of the axisymmetric Planetary Nebula envelope, etc.

6.2.2   Dust Structure around evolved stars

An ELT equipped with a mid-IR instrument such as METIS would bring a whole variety of evolved objects within range for direct imaging of their dusty CSE. In that sense, it would supersede the short baseline VLTI, providing an image with several magnitudes higher sensitivity and dynamic range. A prerequisite for this research, however, is that the instrument can deal with the high flux levels of nearby luminous objects (of the order of many Jy). This will require the use of the corongraphs. For all these objects, complementary ALMA observations would allow us to create a combined gas+dust picture of the CSEs. The scientific questions that METIS will tackle in the study of dusty CSEs can be broken up into the different instrument modes:

- **Imaging**: The imaging modes from L to Q offered by METIS will allow a detailed study of the morphology of the ejecta, which is known to be related to stellar pulsation (shells), convection (clumps/plumes), chemical composition (dust and molecules), binarity (disks) and rotation (torii or aspherical shells). It would, for example, extend the current VISIR sample of spatially resolved post-main sequence objects (typically a few per class, see Fig. 1) by a factor of almost 50, finally allowing proper statistical analysis. This is crucial if we want to understand the shaping mechanism of Planetary Nebulae. If a substantial time baseline were available (a few years), it would be possible to directly observe the dynamics (e.g., expansion) of the dust in the CSE, which can then be compared to the dynamics of the gas (cf. the study of the molecular envelope).

- **Low-resolution long-slit spectroscopy**: The low-resolution N-band long-slit spectrograph will allow us to study the dust composition as a function of location within the CSE, by scanning the CSE with the slit. This will provide a direct observation of the dust condensation sequence in dust-driven AGB winds which is the most problematic unknown in all of AGB star research. Also, it will be used to determine the location of crystalline dust in those CSEs where strong dust processing appears to occur. Furthermore, studies of the evolution of dust along the AGB done in galactic globular clusters can be extended to external galaxies.
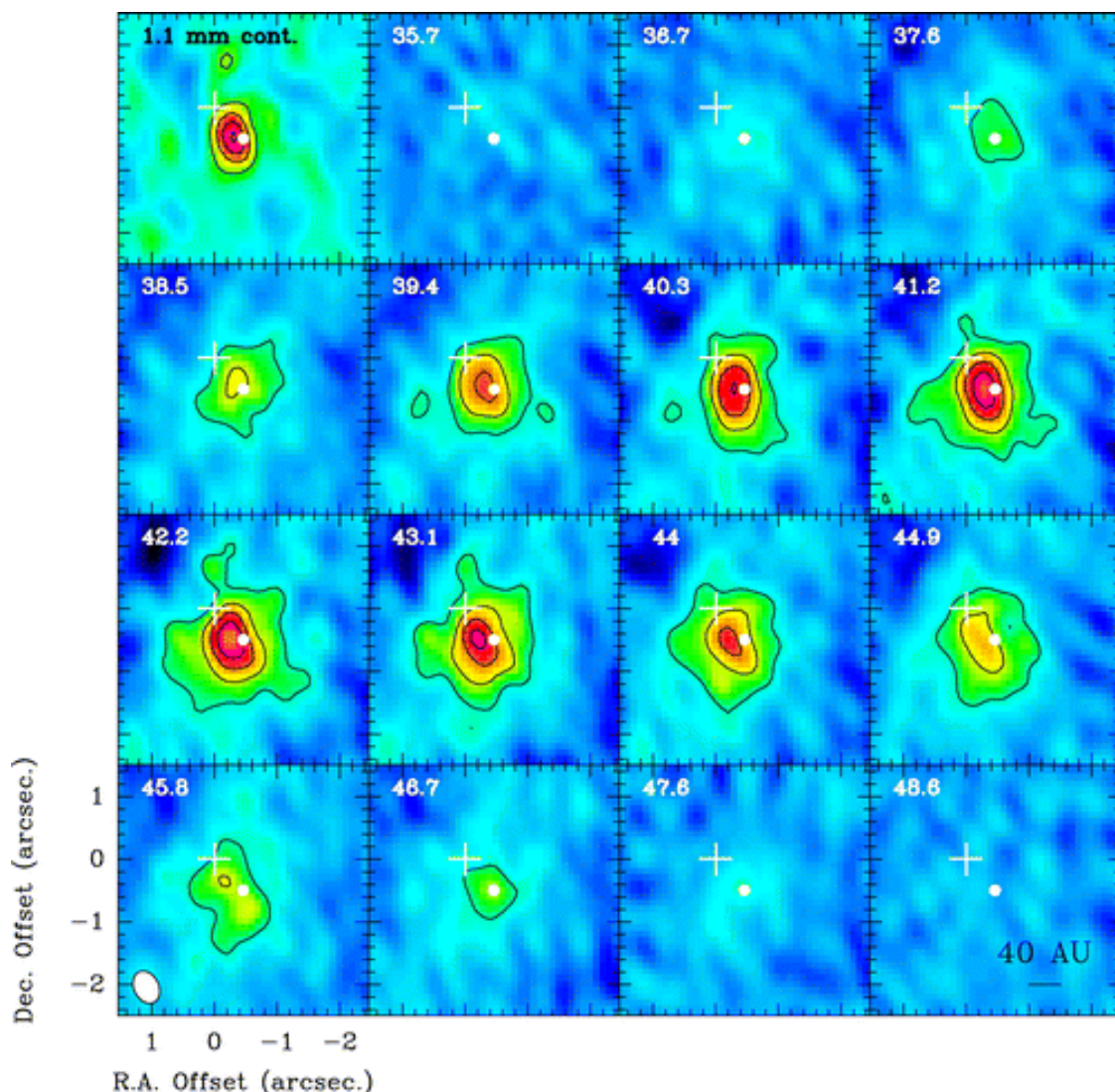
Figure 6-3: 1.1 mm continuum emission (top left corner box) and HCN (3-2) channel maps of W Hya as observed with the SMA very extended configuration. Contours are every 25 mJy/beam for the continuum map, and every 0.75 Jy/beam (5 sigma), corresponding to 60 K for the synthesized beam of 0.55"×0.40" (P.A. = 26 deg), for the channel maps. The white cross indicates the position of the phase center, set at the stellar position from the Hipparcos catalogue in the year 2000 (R.A.(J2000) = 13:49:01.998 and Dec.(J2000) = -28:22:03.49). The white dot gives the expected position of the star at the date of our observations in 2008, due to its proper motion. The small offset (?0.15") between this position and the peak emission may be due to baseline errors. The detection of carbon-bearing molecule HCN in the inner envelope of the oxygen-rich AGB star W Hya clearly points to an inner wind origin, possibly due to shock-induced non-equilibrium processes taking place in the inner envelope (from Muller et al. (2008)).

6.2.3   Protoplanetary disk physics around evolved stars: second generation of planets ?

The focus for the study of planet formation is directed to the disks around young stars, in which planet formation clearly occurs (see chapter on protoplanetary disks). However, it has recently become clear that there are other cases where disks with similar properties can form and might potentially lead to the formation of macrostructures or even planets. An interesting, albeit slightly exotic, case is planets around pulsars (Wolszczan & Frail 1992) which are believed to form in a disk formed after a supernova explosion (Wang et al. 2006). More recently, planets have also been discovered around the post-common envelope binary NN Ser (Beuermann et al. 2010), but also around AGB stars like L^2Pup (Kervella et al. 2016; Homan et al. 2017) with its disk resolved both with ALMA as well as with the extreme AO instrment at the VLT (SPHERE).
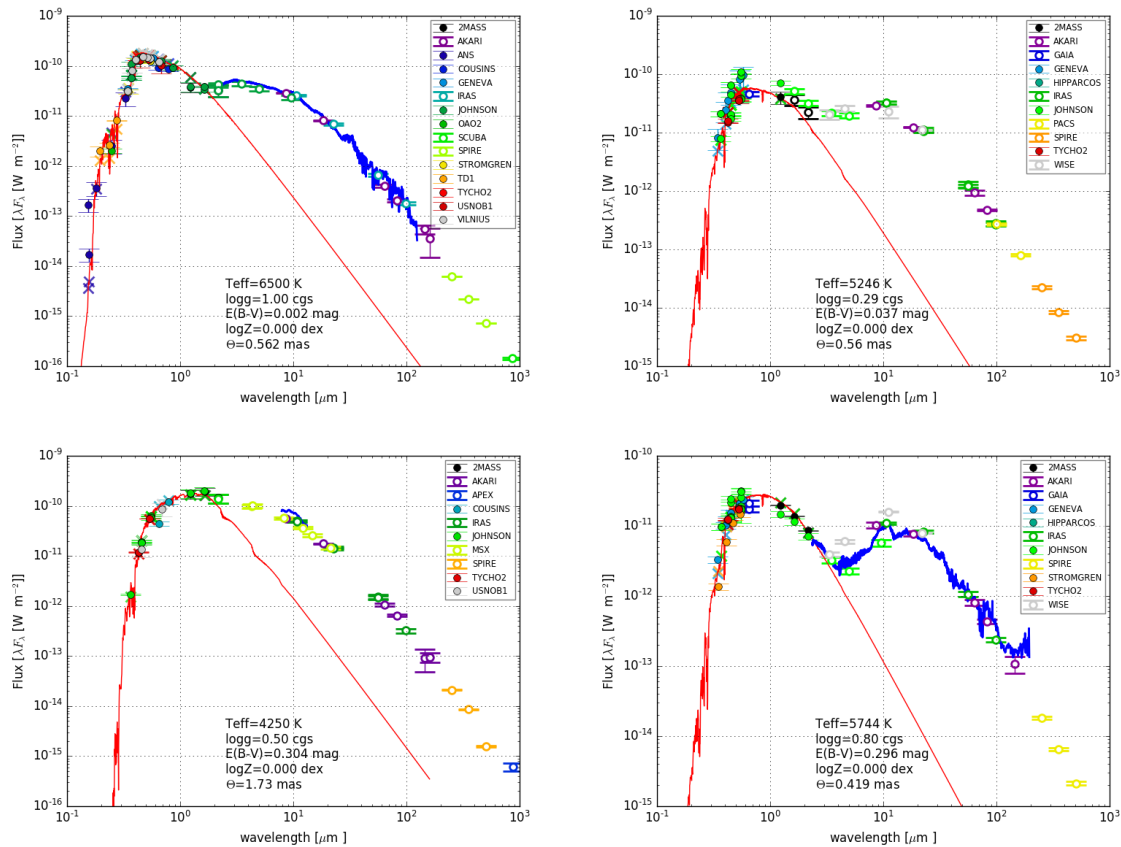
Figure 6-4: Characteristic examples of disks around post-AGB stars. The IR excess starts as dust sublimation temperatures, and the peak of the SED is around 10 μm. Some 90 of these objects are known in the Galaxy (Van Winckel 2018) and a significant number has been found in the LMC and SMC (Kamath et al. 2014, 2015).

An even more intriguing case is made by the recent detection of disks around so-called binary post-AGB stars, which in many observational properties seem to be very similar to classical protoplanetary disks. Their distinct SED characteristic (bimodal, with peaks in the visible and mid-IR and a distinct near-IR excess, see Figure 6-4), was used to start a systematic search for binary post- AGB candidates de Ruyter et al. (2006). A follow-up study includes radial velocity monitoring, high-spectral resolution optical and IR studies, and sub-millimeter bolometric observations. All objects show evidence for the presence of long-lived dusty disks (Van Winckel 2003, 2018).

Recent interferometric studies confirm the very compact nature of the circumstellar material (Hillen et al. 2013, 2014, 2015, 2017; Kluska et al. 2018) (Figure 6-6) and SPITZER spectroscopy shows the very high level of processing of the dust grains in the disks (Gielen et al. 2007) (Figure 6-5). Additionally there is an overresolved component which can be up to 30-40% of the flux in the optical (Hillen et al. 2013) or 15 % in the H-band (Kluska et al. 2018) and which is not accounted for by the state-of-the art radiative transfer models. The binary fraction for this class of objects is 100% (van Winckel et al. 2009; Oomen et al. 2018). The companion stars are likely unevolved main-sequence stars, which do not contribute significantly to the energy budget of the objects. These stars have not become contact binaries yet. However, their orbits are too small to have accommodated an AGB star. Therefore the global picture that emerges is that a binary star evolved in a system that is too small to accommodate a full-grown AGB star. During a phase of strong interaction, that is only poorly understood, a circumbinary dusty disk was formed, but the binary system did not suffer from orbital decay. What we observe now is a F-G type post-AGB supergiant in a binary system surrounded by a circumbinary dusty disk. The objects were likely truncated during their ascent on the AGB branch. Observational hints for that truncated AGB evolution is that in most objects, the circumstellar dust is oxygen rich (Gielen et al. 2008).

The dynamical interaction between this strong wind and the companion star causes part of the mass loss to be trapped in a circumbinary disk. Millimetre observations of CO lines with the Plateau de Bure interferometer and ALMA showed that these disks appear to be stable, i.e. in Keplerian rotation (Bujarrabal et al. 2013, 2015, 2018). These observations also revealed a disk-wind component suggesting angular momentum transport in the disk. These disks possess dust grains with large sizes (de Ruyter et al. 2005; Gielen et al. 2011; Hillen et al. 2015), and large crystallinity fraction (Gielen et al. 2011) (see also Figure 6-5).

Radiative transfer models of protoplanetary disks (PPDs) around young stellar objects (YSOs) are able to reproduce both the SED and infrared interferometric measurements on a few targets (Kluska et al. 2018). The dust masses found in these disks are of the order of 10^{-4} - 10^{-3} $M_{\odot}$ (Sahai et al. 2011; Hillen et al. 2014). In some cases, time-resolved spectroscopic data indicates the creation of a high velocity outflow (jet) in an accretion disk around the companion (Gorlova et al. 2012, 2015; Bollen et al. 2017)
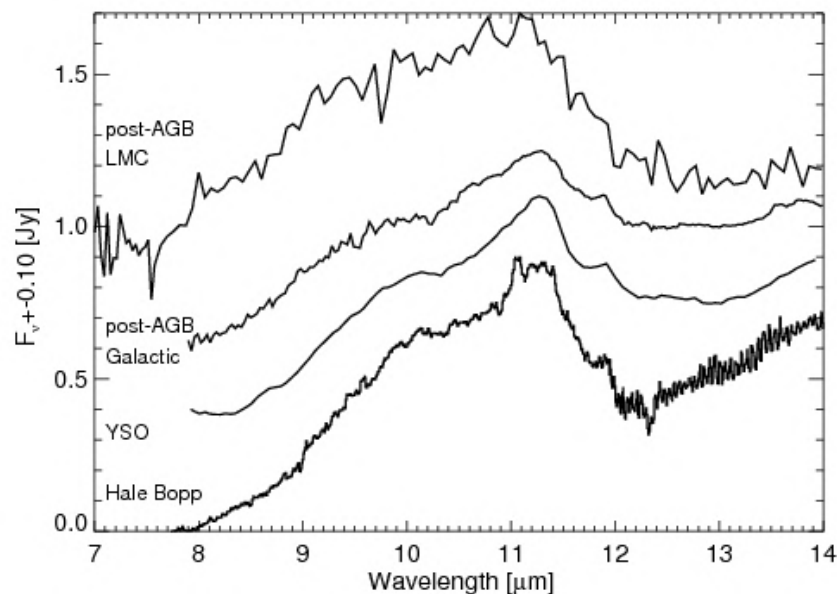
Figure 6-5: 10 μm silicate emission profiles of a wide variety of objects: the solar system comet Hale Bopp, a young stellar object (YSO), a Galactic post-AGB binary and a post-AGB star in the LMC. Note the very similar profile indicating that the average silicate grain is quite large with a clear contribution of crystalline silicates as shown by the 11.3 μm forsterite feature. The silicate feature is an ideal tracer for dust processing in the circumstellar disks.

In general, despite very different forming processes, post-AGB disks are in many ways (infrared excess, Keplerian rotation, winds, jets, dust mass, dust mineralogy and grain sizes) similar to protoplanetary disks around YSOs. As the protoplanetary disks are well studied both observationally and theoretically, the very close similarity with the disks around post-AGB binaries rises the question of the universality of physical processes in dusty circumstellar disks and more specifically of their planet formation efficiency. Circumbinary disks around pAGBs can therefore be second generation planet forming disks, especially as several planets are candidates of being formed in such disks (e.g. NN Ser as mentioned above). One way to form planets in those disks would be by gravitational instability (e.g. Schleicher & Dreizler 2014) and METIS, together with ALMA, would be able to probe and constrain such disk instabilities that happen in the outer parts.

The spatial resolution of the ELT, combined with METIS, will allow us to use coronographic high contrast imaging of the second generation of circumbinary disk. This will complement the interferometric data and allow for direct detection of structure in the disks which may be induced by the central binary as well as the eventual formation of macroscopic structures. The structure and physical origin of the overresolved flux will be determined as well. In Figure 6-6 we simulate a METIS experiment in the N-band, based on a detailed radiative transfer model of the disk around on of these systems for which the inner rim was resolved by optical interferometry (Hillen et al. 2015; Kluska et al. 2018). While the IFU in the L band will allow to
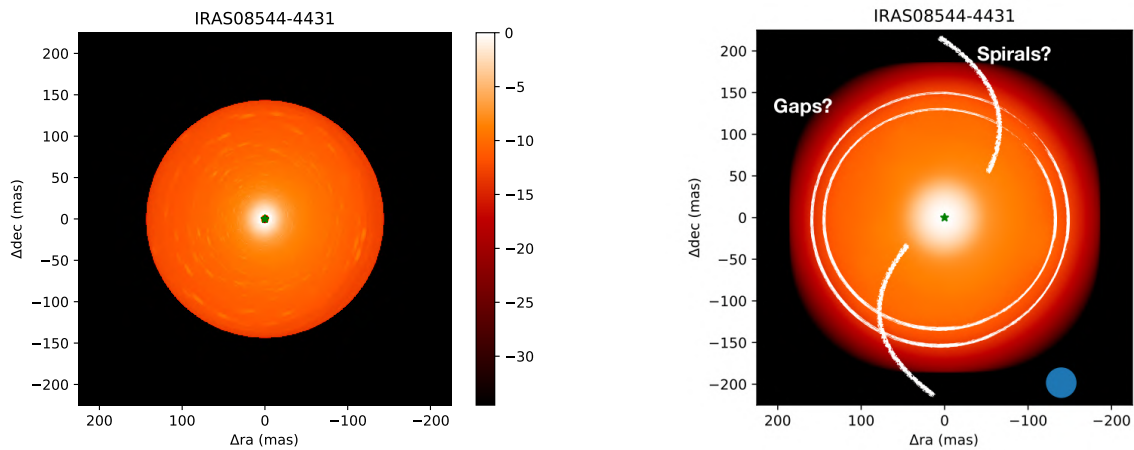
Figure 6-6: Left: Full radiative transfer model with a axisymmetric model of IRAS08544-4431 at 4 μm.(Kluska et al. 2018). Right: The same image but convolved with the METIS beam. METIS with the coronograph, will allow for direct detection of disk structures like spirals and eventual gaps.

study the circumstellar gas composition and dynamics of the interacting binaries, the coronographic images will directly probe the disk structure and its different components.

We have now identified very similar objects in the LMC and SMC. In the LMC, the disk sources account for about 30% of all post-AGB candidates (van Aarle et al. 2011; Kamath et al. 2014, 2015). Interestingly, disks are also observed at much lower luminosities where they are suggested to be post-RGB systems which have shortcut their evolution on the Red Giant Branch (RGB) (Kamath et al. 2016) This sample is unique as the known distances allow for a full astrophysical test with current (binary) evolution theory. Moreover, some the objects have disk SEDs, but luminosities that indicate a post-RGB instead of post-AGB nature (Kamath et al. 2015). The large Galactic, LMC and SMC samples prove that circumstellar disk formation must be an important ingredient in the evolution of binaries with a wide range of initial masses, mass ratios and initial orbital parameters.

METIS is an ideal instrument to probe both the gas and dust components of the disks and their interaction with the central stars. The low-resolution spectrum of the N-band will allow mineralogy studies using the 10-micron silicate feature (Figure 6-5). The profile is very sensitive to dust-grain processing both in grain-growth and crystallization (van Boekel et al. 2005; Gielen et al. 2008, 2011). METIS is ideally suited to study the faint objects in the LMC (fluxes in the N-band are down to a few mJy). The disks are very compact, thus at the distance of the LMC and SMC, they are not expected to be resolved with METIS. A systematic study of the whole extragalactic sample will allow detailed correlation studies between dust processing on the one hand, and the positions of the central star in the HR-diagram and the associated evolutionary status on the other hand. Moreover, the metallicity of the initial population will, certainly for the SMC, likely affect the dust processing as well. METIS in high-resolution spectroscopic mode will allow us to study the presence, composition and dynamics of the hot gas component in the disk. The L and M bands contain bands of CO, OH and water lines for the O-rich environments. The high-resolution mode is ideally suited to probe important isotopic abundance ratios of C and O, but also to allow us to compute the temperature and dynamics of the hot circumstellar gas (e.g. Hinkle et al. 2007) for a pilot study of a nearby post-AGB binary). The high-resolution IFU spectra will allow us to probe the expected rotation of the hot circumstellar gas layer and hence probe the gravitational mass of the whole system.

The feedback from the disk on the star is important, as it accounts for the strong depletion of refractory elements in the stellar photosphere. This photospheric chemical peculiarity is characterized by a low abundance of refractory elements like Fe, Ca, and Si, whereas volatile elements like S and Zn are near-solar and are commonly detected in the central stars of the disk sources (e.g. Van Winckel 2003; Maas et al. 2005; Giridhar et al. 2005; Hinkle et al. 2007). Despite being frequently detected, this depletion process remains very poorly understood. A systematic study of the sample of evolved stars with circumbinary,

protoplanetary-like disks in the LMC and SMC will only be possible with the METIS at the ELT. The ultimate goal of the program is to gain insight into the final evolutionary phase of a wide range of binaries. This evolution is intimately connected to the evolution of the circumbinary protoplanetary disk.
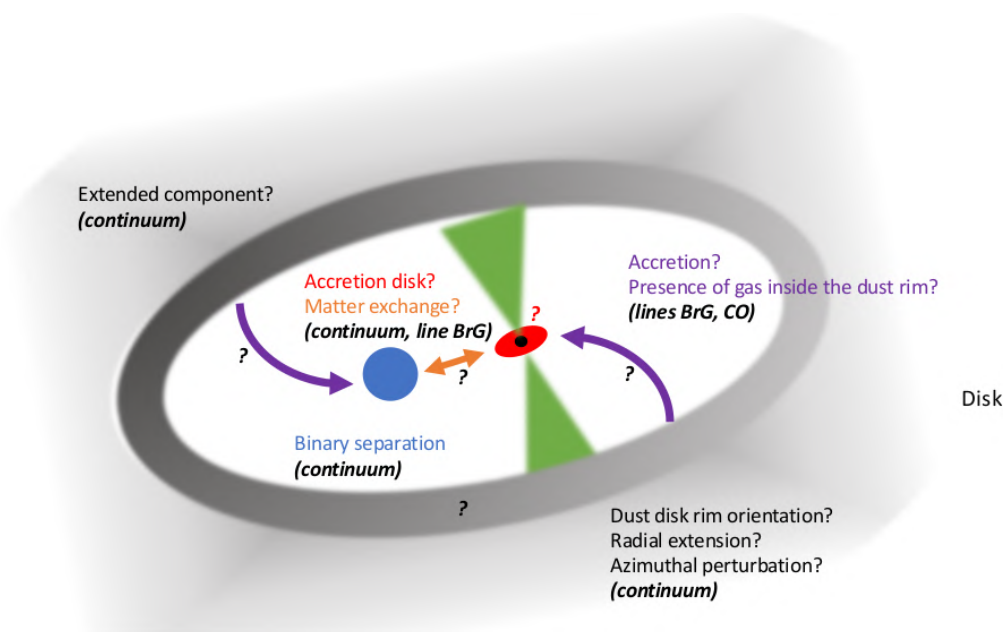
Figure 6-7: Cartoon of the physical interplay between the central post-AGB binary and the circumbinary disk. METIS will help constraining the complex interaction processes in these disks (Figure courtesy of J. Kluska).

Since these disks share so many properties with protoplanetary disks, is it conceivable that they, too, form planets? Does that depend on the chemical composition of the disk material? If yes, what will the further evolution of such disks look like? Could life form on these planets? Can they, or the planetary material formed in them, be detected during later evolutionary phases? In Figure 6-7, we show a cartoon of all structural components of binary post-AGB stars and their interaction with the circumbinary disk. METIS on the ELT will focus on the disk structure as well as on the circumstellar gas physics of these interacting binaries.

6.3   Gas producing agents in galaxies

While also JWST, and especially the MIRI instrument, will study the individual producing agents in nearby galaxies, only with the spectroscopic mode of METIS, unprecedented details on the chemical and isotopic gas-producing agents are possible. The space observatories ISO and Spitzer provided us with a first glimpse of the gas and dust enrichment of the Galactic ISM in our own Milky Way up to the Fornax dwarf spheroidal galaxy (d$\sim$140 kpc) in the 2–40 μm range. The superb sensitivity of METIS on the ELT (and of MIRI on the JWST beyond 5 μm) will allow detailed spectroscopic studies of the gas (and dust) species in a statistically relevant sample of evolved stars in Local Group galaxies (in the field and in clusters). These cover metallicities lower than our Milky Way and the LMC down to metallicities as low as 1/25 th of solar. This will enable us to study stellar gas and dust mass-loss rates and dust condensation sequences as a function of the metallicity in galaxies up to d$\sim$750 kpc. ALMA will be restricted to the nearest galaxies while MIRI does not cover the most important gas mass loss indicator, i.e., CO. Hence, we will be able to pinpoint the main gas and dust providers in the galactic interstellar media and to look for dependencies upon type of galaxy, interstellar activity, metallicity, etc. The insights gained from these investigations will also have an impact on our understanding of what the main gas and dust producers in starburst galaxies and ultra-luminous infrared galaxies (ULIRGs) are.

7 GALACTIC CENTER

7.1 Introduction and Scientific Background

The Galactic Center region is of great interest not only as the center of our galaxy but also as the environment of the closest (quiescent) super-massive black hole (see recent reviews, e.g., Eckart et al. 2017; Genzel et al. 2010). Largely enshrouded by gas and dust, it can be best explored at radio, sub-millimeter, Mid-to Near-infrared, X-ray and γ-ray wavelengths. The region includes a $\sim$4 million solar mass super massive black hole (SMBH; Eckart & Genzel 1997; Ghez et al. 1998), three clusters of young massive stars, and massive molecular clouds (see, e.g., Eckart et al. 2005). At a distance of 8 kpc it is the closest nucleus of a Galaxy that we can study in detail. In the central region there are several prominent filaments seen across the wavelength bands. Some of them are the Radio Arc (Yusef-Zadeh et al. 1984) consisting of non-thermally emitting linear filaments perpendicular to the Galactic plane, and the Arched Filaments and Sickle as thermal emitters seen in the light of their radio recombination lines (e.g., Yusef-Zadeh & Morris 1987; Morris & Yusef-Zadeh 1989; Lang et al. 1997, 2001). All constituents of the inner few parsecs, the super-massive black hole (SMBH), surrounding star clusters, streamers of ionized gas, molecular dust ring and a supernova remnant have been studied extensively during the last years (e.g., Melia & Falcke 2001).

7.2 Scientific Goals

There are numerous topics of great scientific importance in this complex region, including the stellar dynamics around the SMBH and its associated radio source Sgr A*, and the formation and evolution of massive young clusters found in the immediate vicinity of the SMBH. Fig. 7-1 shows the near-IR and mid-IR view of the central parsec region, illustrating their complementary nature. The infrared images are close to the diffraction limit of an 8m telescope at their wavelengths. However, METIS would provide approximately the same resolution at mid-IR wavelengths than NAOS-CONICA in the near-IR, enabling the first pan-spectral characterization of the region around Sgr A*. Highest angular resolution and/or diagnostic spectral line tracers available in the MIR are essential to make further progress in this field (e.g. through absorption features from ices H_2O, CH_4, CO, NH_3 etc.; or through emission features from gaseous molecules like $H_2, CO, H_2O, CH_4, C_2H_2, HCN, OH, SiO$ etc.). Several of them (e.g. CH_4, C_2H_2 in gas and ice) can be used as probes for stellar disks. For the Galactic Center we have demonstrated the usefulness of the H_2O line emission and the CO gas and ice absorption to study the extinction towards the Galactic Center and the properties of the GC interstellar medium (Moultaka et al. 2006). In addition to the central stellar cluster and the mini-spiral, the circumnuclear ring (CNR) is also bright in the MIR (see Fig. 7-2).

One issue of particular interest is the accretion and emission mechanisms of the SMBH. Variability and flares have been detected at infrared wavelengths (Genzel et al. 2003). The intrinsic size of Sgr A* has remained unresolved at centimeter and longer wavelengths because radio waves from Sgr A* are scattered by the turbulent interstellar plasma along the line of sight. The scattering increases with wavelength as λ^{-2}, pushing observations to shorter and shorter wavelengths. ALMA is expected to be a powerful tool for such observations, and MIR observations at the highest spatial resolution will enormously contribute to this exciting puzzle. Recent broad band observations give upper limits of factors of 2–10 above the theoretically expected SED for Sgr A*, based on a variety of accretion- and jet models. The limiting flux for these MIR observations was 80 mJy (optimum values are 20 mJy). Depending on the finally chosen site of the ELT, the corresponding point source sensitivity is expected to be 0.06 mJy to 0.08 mJy at 8.6μm. The quiescent Galactic center, up to now is not detectable at NIR wavelength, however, during short flare phases the GC has been observed and even polarimetric measurements have been obtained.

While such studies are near the limit of feasibility, monitoring of the quiescent and flaring GC could be easily performed with an ELT. Even medium resolution spectroscopy of Srg A* can be obtained. Thus, a very detailed study of the central few Schwarzschild-radii environment of a MBH will be possible.
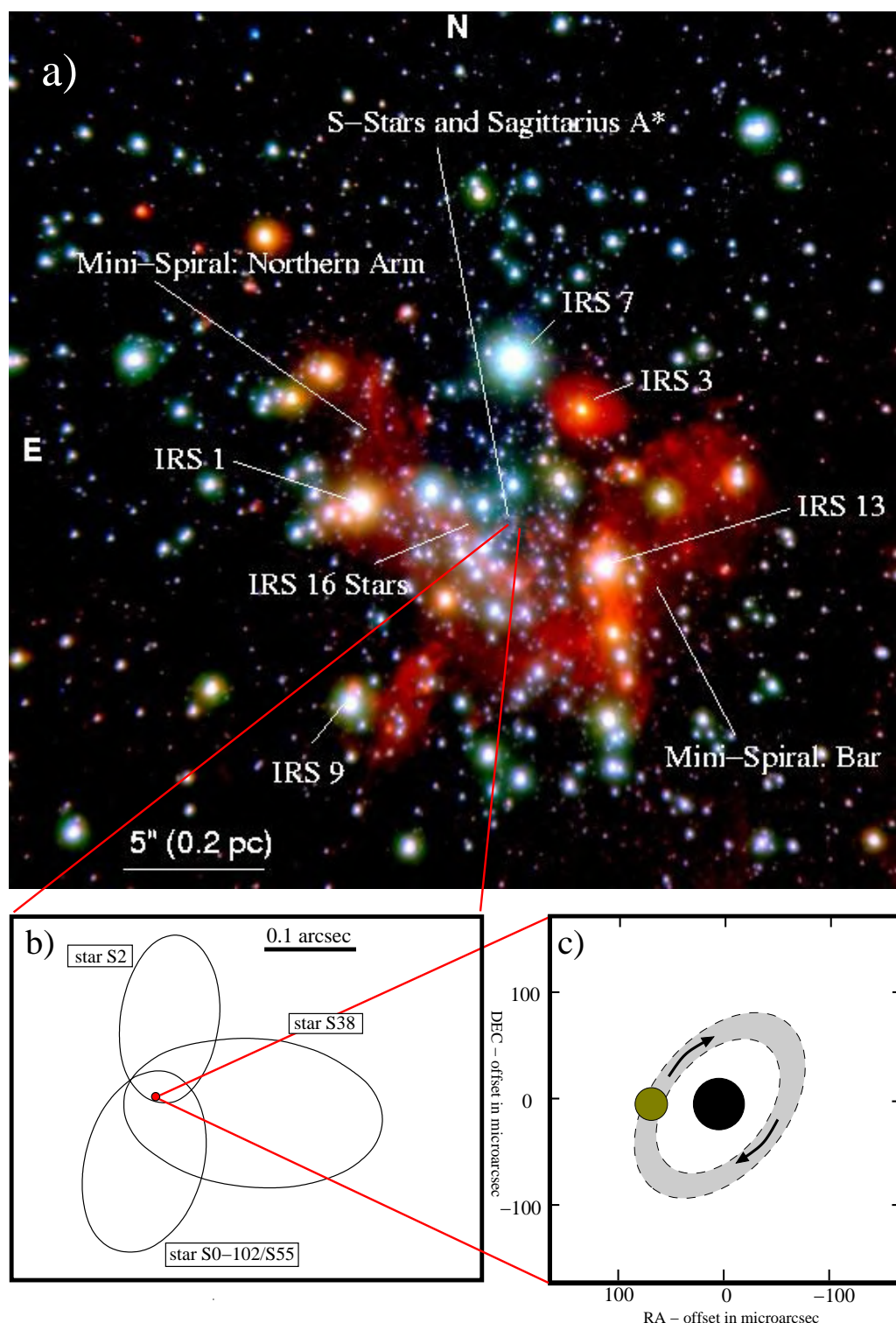
Figure 7-1: a) The central parsec of the Milky Way seen with the near infrared camera and adaptive optics system NACO at the ESO VLT. Two narrow band images (at 2.18μm and 2.36μm) were combined with a broad band image at 3.8μm to obtain a pseudo-color image. The red extended emission is due to gas and dust in the mini-spiral or due to circumstellar material of individual stars (see section 3 and references therein). **b)** The orbits of three of the innermost stars orbiting SgrA*. Star S2 can be used to determine the relativistic nature of the supermassive black hole environment (see section 4.1; Gravity Collaboration et al. 2017, 2018; Parsa et al. 2017; Eckart et al. 2018). **c)** Sketch of a possible scenario in the immediate vicinity of SgrA* (black circle at the center) with material in orbit around it (grey band with yellowish source component as a hotspot; see section 4.2; Gravity Collaboration et al. 2017; Meyer et al. 2006a,b; Eckart et al. 2006a,b). (Image from Eckart et al., submitted Conf. Proc.)
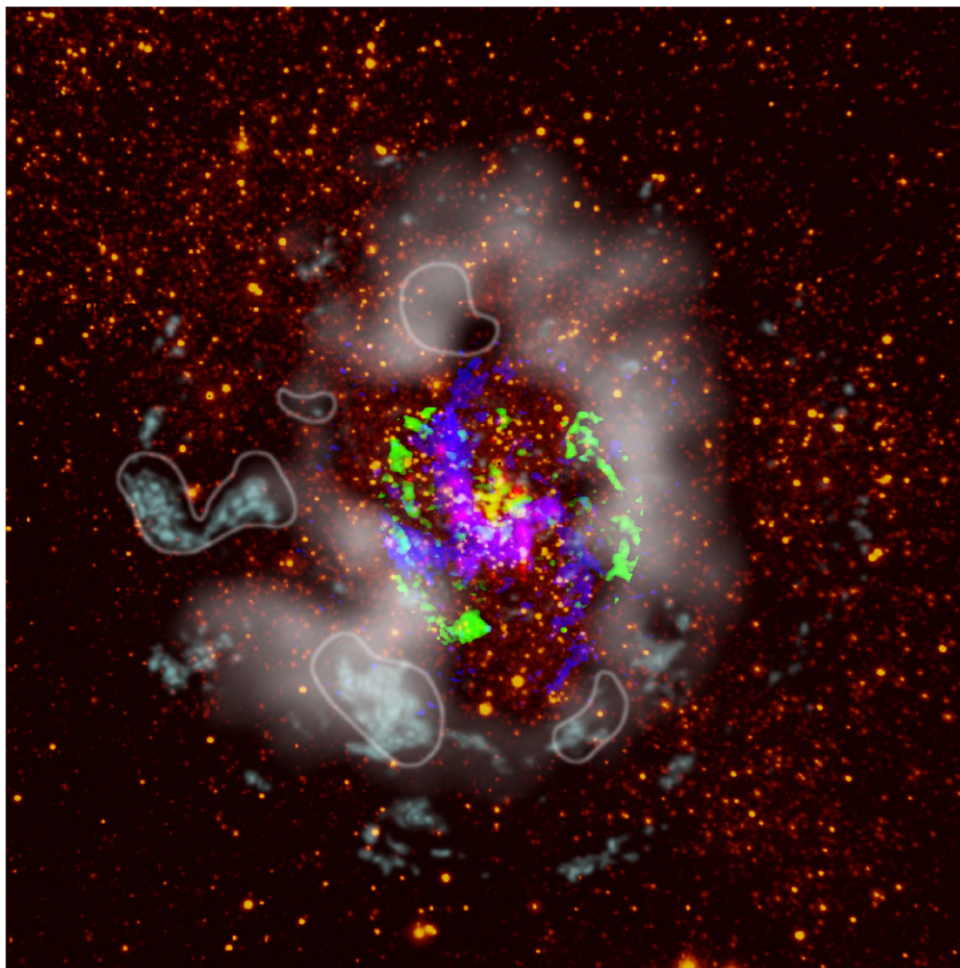
Figure 7-2: Sub-millimeter, NIR, and inverted X-ray composite image of the inner 5.6 pc×5.6 pc of the Galactic Center. **Yellow:** Stellar background from a combination of ISAAC 1.19μm, 1.71μm, and 2.25μm narrow filters (from Nishiyama & Schödel 2013); **red:** NACO L'-band dust emission. Sub-millimeter ALMA measurements: **blue:** GC mini-spiral is traced by 250 GHz continuum and H39α ionized emission; **green:** Inner regions of the CNR (in projection) shine in CS(5-4) molecular line; **cyan:** N$_2$H$^+$(1-0) molecular-gas major structures coincide with foreground dark clouds (Moser et al. 2017). **Extended white shadow:** This shadow shows the footprint of the circumnuclear disk as seen by the depression of the X-ray diffuse emission observed with CHANDRA (Mossoux & Eckart 2018). **Enclosed with white lines:** Prominent dust extinction patches, possibly star-forming regions, visible as dark silhouettes over the bright stellar background are enclosed with white lines. Some emission regions are also identified e.g. the South East Extension (SEE), that towards the west of it (SEW), the V-cloud, the Central Association (CA) and the Triop (see Moser et al. 2017, for more information). (Image from Eckart et al., submitted Conf. Proc.)

General requirements for METIS: Galactic center science this is mainly bright science - angular resolution and field of view are essential. In continuum emission one is confusion limited since one looks into the central star cluster. In spectroscopy one may only get into trouble if one uses the highest resolutions possible or faint continuum sources for absorption line studies.

Regarding Adaptive Optics and a possible N-band detector:

(1) For galactic center SCAO with limiting magnitude of K 12 mag is well suited and sufficient.

(2) Broad band N band imaging will only be used in a small fraction of the Galactic Center science case and it is of comparatively lower importance (compared to L, M band imaging and spectroscopic studies).

Simulations of the expected images and spectra of the Galactic Center as measured with METIS have started. In Figure 7-3 we show a simulated detector images in N-Band (N2). The image has been derived from a data cube derived from a continuum model of the Galactic Center region simulation extended and stellar components with appropriate continuum scaled template spectra for the extended (GC ISO SWS
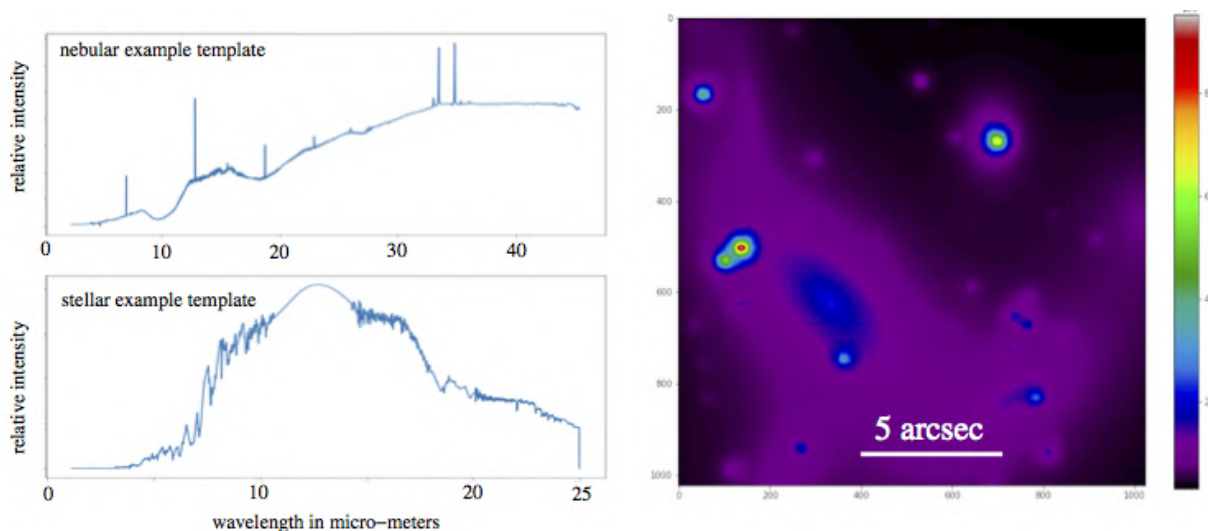
Figure 7-3: Example of simulated data for the METIS Galactic Center project. Template input spectra for extended and stellar/ compact components (left) and a simulated N-band continuum image (right).

spectrum) and stellar (as an example here a Pickles M5V spectrum) components including expected detector noise. These simulations will relative intensity relative intensity allow us to extract continuum, color, line, and line to continuum maps with noise. They will allow to address detectability and contrast questions.

7.3   A Representative Observing Program

The center of our galaxy (GC) is the closest galactic nucleus that access Control Help can be studied. In addition to a massive black hole, the central half parsec of the Milky Way hosts a surprisingly high number of massive young stars organized in at least one disk-like structure of clockwise rotating stars. The mechanism responsible for the presence of young stars in the strong tidal field of the super-massive black hole (SMBH) at the position of SgrA* is not clear. We have been actively publishing on a variety of topics that can ideally be followed up on - or even tackled for the first time using the ELT in the MIR.

7.3.1   YSO Candidates in the central stellar cluster

It is currently unclear how the young stars have been formed in the central stellar cluster. The Galactic center IRS 13E cluster is located 3.2 from SgrA*. This cluster harbors sources that are amount the best candidates for young (recently formed) stellar objects in the central cluster (e.g., Mužić et al. 2008); IRS 13E is an extremely dense stellar association containing several Wolf-Rayet and O-type stars, at least four of which show a common velocity. Only half an arcsecond north of IRS 13E there is a complex of extremely red sources so-called IRS 13N. Their nature is still unclear. Based on analysis of their colors, there are two main possibilities: (1) dust-embedded sources older than few Myr or (2) extremely young objects with ages less than 1 Myr. In Mužić et al. (2008) we present the first proper motion measurements of IRS 13N members and four of IRS 13E stars resolved in the L-band. The L-band (3.8μm) observations were carried out using the NACO adaptive optics system at the ESO VLT. Proper motions were obtained by linear fitting the stellar positions extracted by StarFinder as a function of time, weighted by positional uncertainties. As a result we could show that six of seven resolved northern sources show a common proper motion, thus revealing a new co-moving group of stars in the central half parsec of the Milky Way. The common proper motions of IRS 13E and IRS 13N clusters are significantly ($>$3) different. In Fig. 7-4 we show the IRS13N sources. We also performed a fitting of the positional data for those stars onto Keplerian orbits, assuming SgrA* as the center of the orbit. Our results favor the very young stars hypothesis.

Very good candidates for YSOs are the infrared excess sources like the dusty S-cluster object DSO (alias G2). This dusty source had been approaching the black hole SgrA* and passed by in 2016. The faint DSO was discovered in 2011 Gillessen et al. (2012) on its way towards the supermassive black hole SgrA*. The object is very faint in the NIR K-band, however, well detectable in its Brγ-line emission and considerable brighter continuum emission of the longer wavelength infrared L-band. After its discovery large monitoring programs were started by several groups. We covered the investigation of the source properties between the years 2006 to 2016 using the SINFONI camera at the ESO VLT.

The NIR 2.2 μm continuum emission of the DSO was first found Eckart et al. (2013) making use of the NACO camera at the ESO VLT. A confirmation of its detection could also be achieved using public data of the NIRC system at the Keck telescope (Eckart et al. 2014). Furthermore, the continuum source clearly showed itself in SINFONI data obtained at the VLT. As the source passed by SgrA* it showed a very obvious transit from a red- to a blue-shifted Brγ-line emission (Valencia-S. et al. 2015). Given that the source was not disrupted during and after the flyby around SgrA* - and given the fact that it stayed very compact in its continuum and line emission (Valencia-S. et al. 2015; Witzel et al. 2014), it became obvious that it is not an extended and core-less cloud as previously claimed (e.g., Gillessen et al. 2012; Pfuhl et al. 2015; Schartmann et al. 2015).

Shahzamanian et al. (2016) could detect and measure the polarization of the DSO as it was descending towards its periapsis close to SgrA*. These observations showed that it is very likely a compact dust-enshrouded - probably young - star. The high degree of polarization implies that the scattering material is not distributed highly symmetrically around the source (see e.g., Zajaček et al. 2014, 2016). The data point at a combination of a bow shock and a bipolar wind propagating and surrounding a central star (Shahzamanian et al. 2016; Zajaček et al. 2014, 2016, 2017; Valencia-S. et al. 2015).

The contribution of METIS: High resolution studies with METIS will allow us to clears determine the structures of the dust envelopes of these young star candidates. Spectroscopy of PAH and ionic line emission will help us to trace the interaction of the shells with the radiation field from the bright stars in the cluster and SgrA*. Goal of these studies will be to consolidate the identification with young stars that are still surrounded by relicts of their dust disks that will certainly suffer from traveling through the dense stellar cluster. Any interaction of the dusty infrared excess sources with the local Galactic Center ISM or a wind from SgrA* should be observable at high angular resolution with the ELT. Dusty shells or tails should readily become observable in their dust emission.

7.3.2   The Nature of Thin Dust Filaments

Narrow dust filaments in the diffuse ISM of the centra stellar cluster allow us to trace its the interaction with a wind from the central region through their proper motions (e.g., Mužić et al. 2007). L-band (3.8μm) images of the Galactic center show a large number of thin filaments in the mini-spiral, located west of the mini-cavity and along the inner edge of the Northern Arm. In Fig. 7-5 we show the location and proper motion of thin dust filaments in the central stellar cluster. One possible mechanism that could produce such structures is the interaction of a central wind with the mini-spiral. Additionally, we identify similar features that appear to be associated with stars. In Mužić et al. (2007) we present the first proper motion measurements of the thin dust filaments observed in the central parsec around SgrA* and investigate possible mechanisms that could be responsible for the observed motions. The observations have been carried out using the NACO adaptive optics system at the ESO VLT. The images have been transformed to a common coordinate

system and features of interest were extracted. Then a cross-correlation technique could be performed in order to determine the offsets between the features with respect to their position in the reference epoch. As results we derive the proper motions of a number of filaments and 2 cometary shaped dusty sources close (in projection) to SgrA*. We show that the shape and the motion of the filaments does not agree with a purely Keplerian motion of the gas in the potential of the super-massive black hole at the position of SgrA*. Therefore, additional mechanisms must be responsible for their formation and motion. We argue
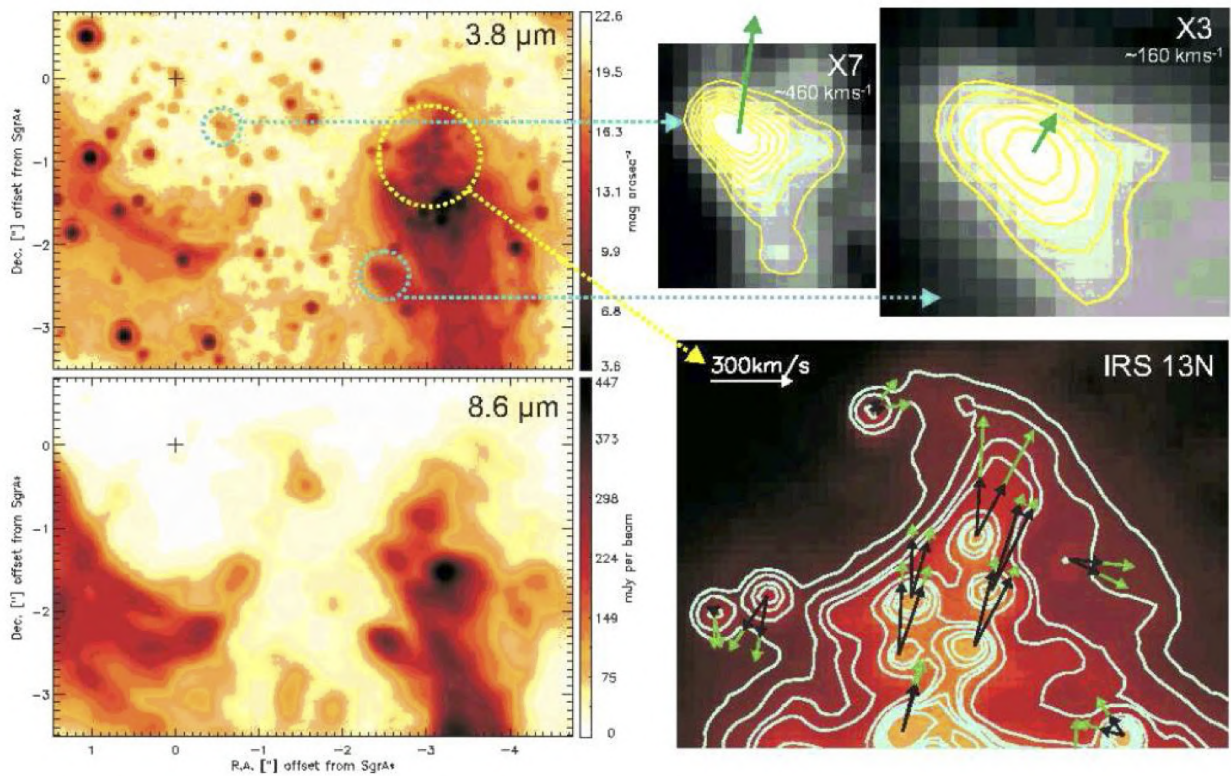
Figure 7-4: Left top and bottom: A 4×6 arcsec^2 section of the central stellar cluster at $3.8 \mu m$ and $8.68 \mu m$ wavelength including the position of SgrA* and IRS13N just north of the cluster of bright stars of IRS 13 proper. Top right: The sources IRS13N, X3 and X7 in the Galactic Center stellar cluster (Mužić et al. 2007). Bottom right: Proper motions of the dust embedded IRS13N sources (Mužić et al. 2008). The small cluster represents a co-moving group of stars showing that this particular group of stars is not only young with respect of their spectroscopic properties, but that it is also dynamically a young stellar association.

that the properties of the filaments are probably related to an outflow from the disk of young mass-losing stars around SgrA*. In part, the outflow may originate from the black hole itself. We also present some evidence and theoretical considerations that the outflow may be collimated.

In Fig. 7-4 we also show the cometary shaped bow-shock sources X3 and X7. These sources show bow-shock structures pointing towards SgrA* and have proper motions of a few 100 km/s almost perpendicular to the projected connection line towards SgrA*. This suggests that these sources interact with a very fast wind (with a velocity of probably larger than ~1000 km/s) probably originating in SgrA*. The stars are also located within the mini-cavity. In summary this indicates that the sources X3 and X7 are possibly the best probes of the accretion process and an associated wind from SgrA*.

The contribution of METIS: Only a ELT class telescope working in the MIR and long-NIR wavelength range will allow us to study the proper motions of a large number of dust filaments like the ones reported by Mužić et al. (2007). Such a study will then give a complete picture of the wind and outflow activities in the central stellar cluster including SgrA*.

7.3.3   Low Luminosity Bow-Shock Sources in the Central Stellar Cluster

The central stellar cluster contains several bow-shock sources or embedded stars that interact with their immediate ISM (mostly associated with the mini-spiral) (e.g. Perger et al. 2008). Mid-infrared observations of the Galactic Center show among the extended mini-spiral a number of compact sources. Their nature is of interest because they represent an interaction of luminous stars with the mini-spiral material or mass
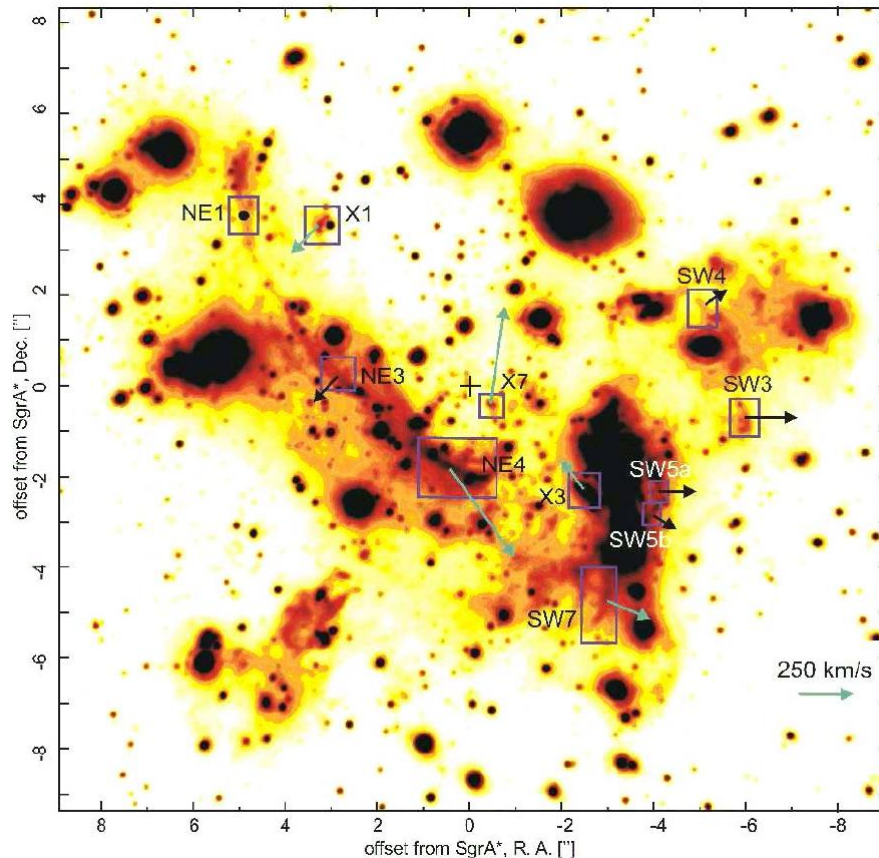
Figure 7-5: L'-band image of the Galactic Center. Boxes mark thin filaments with measurable proper motions. Note that boxes in this image are different from those used for measurements. The arrows show proper motions of the thin filaments obtained in our study: light blue arrows stand for the features with measurable proper motion in both directions, while black arrows show only the proper motion component perpendicular to the feature (see Muzic et al. 2007). The insignificant motion of the Northern Arm filament NE1 is marked with a circle rather than an arrow. The cross marks the position of SgrA*.

losing sources that are enshrouded in dust and gas shells. Characterizing their nature is necessary to obtain a complete picture of the different stellar populations and the star formation history of the central stellar cluster in general. Prominent compact MIR sources in the Galactic Center are either clearly offset from the mini-spiral (e.g. the M2 super-giant IRS 7 and the bright dust enshrouded IRS 3) or have been identified earlier with bright bow shock sources (e.g. IRS 21, 1W, 10W and IRS 5). There are, however, four less prominent compact sources east of IRS 5, the natures of which were unclear until now. In Perger et al. (2008) we present near-infrared K-band long slit spectroscopy of the four sources east of IRS 5 obtained with the ISAAC spectrograph at the ESO VLT in July 2005. We interpret the data in combination with high angular resolution NIR and MIR images obtained with ISAAC and NACO at the ESO VLT. The K-band images and proper motions show that the sources are multiple. For all but one source we find dominant contributions from late type stars with best overall fits to template stars with temperatures below 5000 K. We conclude that the brightest sources contained in IRS 5NE, 5E and 5S may be asymptotic giant branch stars and a part of the MIR excess may be due to dust shells produced by the individual sources. However, in all cases an interaction with the mini-spiral cannot be excluded and their broad band infrared SEDs indicate that they could be lower luminosity counterparts of the identified bow shock sources. In fact, IRS 5SE is associated with a faint bow shock and its spectrum shows contributions from a hotter early type star which supports such a classification.

The contribution of METIS: High angular resolution studies that are sensitive to both point like stars and extended emission will allow us to identify and study dust embedded candidates for young stars. A detailed

compilation of stand-off distances and proper motion velocities will help to determine the stellar winds that are involved and allow us to narrow down the stellar types even in dust enshrouded systems.

7.3.4 Absorption Line Studies

The Galactic Center sources allow for detailed absorption line studies of the intervening material both along the line of sight towards the Galactic Center and very close to/at the Galactic Center (Geballe 1986; Moneti et al. 2001). In our previous works (Moultaka et al. 2004, 2005, 2015), we showed that local absorption occurs probably in the direct environment of the GC infrared sources. As a matter of fact, the spectra of luminous infrared sources in the L-band (from 2.7 to 4.2μm) revealed absorption features due to water ices and hydrocarbons that we claimed to be present in the local medium of the central parsec. These absorption effects were attributed earlier by other authors to be due to material in the foreground molecular clouds (e.g., Chiar et al. 2000, 2002).

Moultaka et al. (2020) presented the results of CRIRES observations of 13 infrared sources located in the central parsec of the Galaxy. The data provide direct evidence for a complex structure of the interstellar medium along the line of sight and in the close environment of the central sources. In particular we find four foreground cold clouds at radial velocities v_{LSR} of the order of -145,-85, -60 and -40$\pm$15 km/s that show absorption in the lower transition lines from R(0) to P(2) and in all the observed spectra. We also find in all sources an absorption in velocity range of 50-60 km/s, possibly associated with the 50 km/s cloud in the Galactic Center region. Hence, as the 50km/s cloud is believed to lie behind the GC cluster, parts of it m lie in the line of sight towards it - indicating the the dynamical structure may be very complex. With the METIS at the ELT the absorption studies can be extended over a much larger field as now also the SNR for fainter sources will be sufficient to study their absorption line spectrum.

The contribution of METIS: IFU low resolution spectroscopy (R=250-1000) is performed in parallel to the imaging mode. In addition to information on SgrA* and the accretion process IFU imaging of the small cusp of high velocity stars will result in proper motion measurements of these objects and will contribute to the determination of the central mass distribution. The cluster of high velocity B-stars that surrounds the SMBH or the stronger continuum of the He-stars (e.g. IRS16C and 16NW) in the central stellar cluster could be used for detailed foreground absorption studies over the field towards the GC. As an example: the $CH_3 v_2$ Q-branch at 16.5μm, the R(0) line at 16μm and the $C_2H_2 v_2$ Q-branch at 13.7μm have been detected towards SgrA* (Feuchtgruber et al. 2000). The CH_3/CH_4 and CH_3/CH ratios are difficult to be reproduced by pure gas-phase reactions in dense clouds. The data presented by Feuchtgruber et al. (2000) indicate a mixture between diffuse and translucent clouds with different densities and extinctions and gas-grain reactions and freeze-out mechanisms are required.

7.3.5 The Super-Massive Black Hole

The infrared source associated with the compact radio counterpart of the super massive black hole (SMBH) at the position of Sagittarius A* (SgrA*) is highly variable in its NIR emission. The identification and investigation of the variability of SgrA* will be a prime goal of the Galactic Center ELT observations with METIS (e.g., Eckart et al. 2008). Sgr A* at the center of the Milky Way is a black hole accreting at extremely sub-Eddington rates (see Fig. 7-6). Measurements of its emission in the infrared and X-ray domains are difficult due to its faintness and high variability.

The optically thin emission in the infrared will allow us to monitor the accretion process in detail and to determine the physical conditions near the black hole and its putative accretion disk or stream (Meyer et al. 2008a). We observed the Galactic center 8.6μm in order to detect a mid-infrared (MIR) counterpart to Sgr A*, parallel to NIR observations. In Fig. 7-7 we show a Lucy-Richardson de-convolved 8.6μm VLT VISIR image. The goal was to set constraints on possible emission mechanisms. Imaging data were acquired with the adaptive-optics assisted NIR instrument NACO and the MIR instrument VISIR at the ESO VLT. As a result we obtained MIR imaging data of an unprecedented quality in terms of spatial resolution and
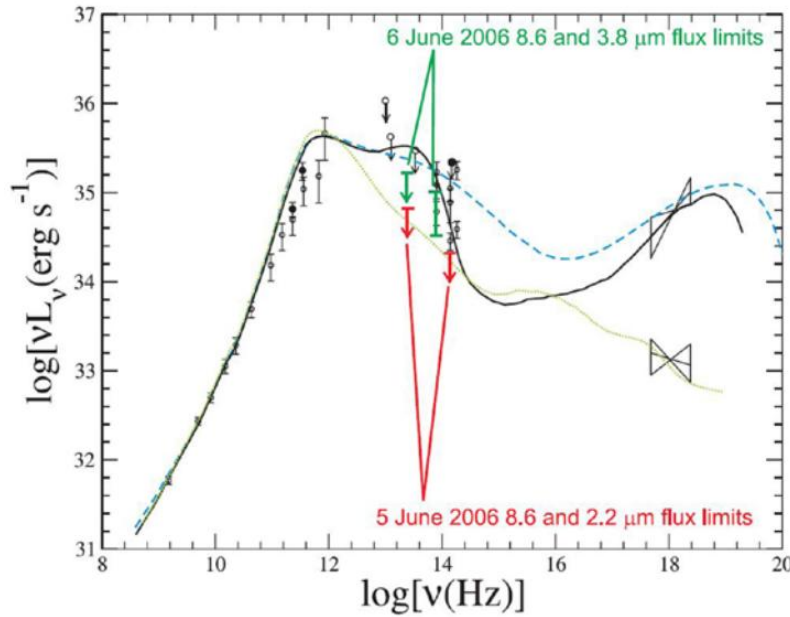
Figure 7-6: Emission models for SgrA* (Yuan et al. 2003, 2004). The upper limit on the flux of Sgr A* at 8.6μm determined by Schödel et al. (2007) is indicated together with the simultaneously measured (NACO/VLT) flux at 3.8μm on June 6 and the upper limit on the 2.2μm emission on June 5 superposed onto RIAF models of the quiescent (dotted line) and flaring (dashed and solid lines) emission from Sgr

sensitivity. An extended ridge of emission is found to be present in the immediate vicinity of Sgr A* thereby rendering any detection of a point source difficult.

No counterpart of Sgr A* has been detected yet at 8.6μm. At this wavelength, Sgr A* is located on a dust ridge, which complicates the search for a potential point source. Schödel et al. (2011) derive an observed 3σ upper limit of about 10 mJy for the emission of Sgr A* at 8.6μm. The de-reddened 3σ upper limit, including the uncertainty of the extinction correction, is ~84 mJy. Haubois et al. (2012) detect no source in the MIR, but derive a low upper limit for a flare at 8.6 μm (22.4 mJy with A$_{8.6\mu m}$ = 1.6±0.5). Schödel et al. (2011) conclude that, based on the available data, Sgr A* cannot be detected in the MIR, not even during flares, with currently available instruments. Haubois et al. (2012) explain this behavior by a loss of electrons to the system and/or by a decrease in the magnetic field, as might conceivably occur in fast outflows and/or magnetic reconnection. Yusef-Zadeh et al. (2010) argues that an anticorrelation between the infrared and the sub-millimeter is due to occultation effects of the SgrA* source by outbound jet/wind components. Both Haubois et al. (2012); Schödel et al. (2011) spent together a total of <5 hours of useful integration time on-source in one filter around 8μm wavelength (this is observing time - including inefficiencies due to the observing modes). This time breaks up into ≤4 integration blocks of typically flare lengths over which the upper limits were derived. Hence, below we can use the 3σ limit of 22.4 mJy to derive the detectability of flares over longer observing time periods.

Using the spectral index of α=-0.7 and the upper 8μm flux density limit we obtain a corresponding dereddened K-band flux limit of ~8.5 mJy. We can use the SgrA* flare flux histogram in the K-band by (Witzel et al. 2012, Fig.1b; see Fig. 7-8), published after Haubois et al. (2012); Schödel et al. (2011). Within a total integration time of 0.4% of the 7 years (i.e., 3490 hours) time interval covered by (Witzel et al. 2012, see also Witzel et al. (2018)) bright flare with a ~31 mJy flux was detected. This is ~100 times less frequent than the 8.5 mJy K-band MIR flare flux limit. On the other hand, typical frequently occurring K-band flares happen with a rate of 6-8 per day (0.25 to 0.33 per hour). This is ~8-10 times more frequent than our limit, resulting in an estimated 30 hours on source VLT integration time. For METIS this detection could be done in a fifth of the time, i.e. a few hours. Failing to detect SgrA* would then speak in favour of alternative scenarios mentioned above.
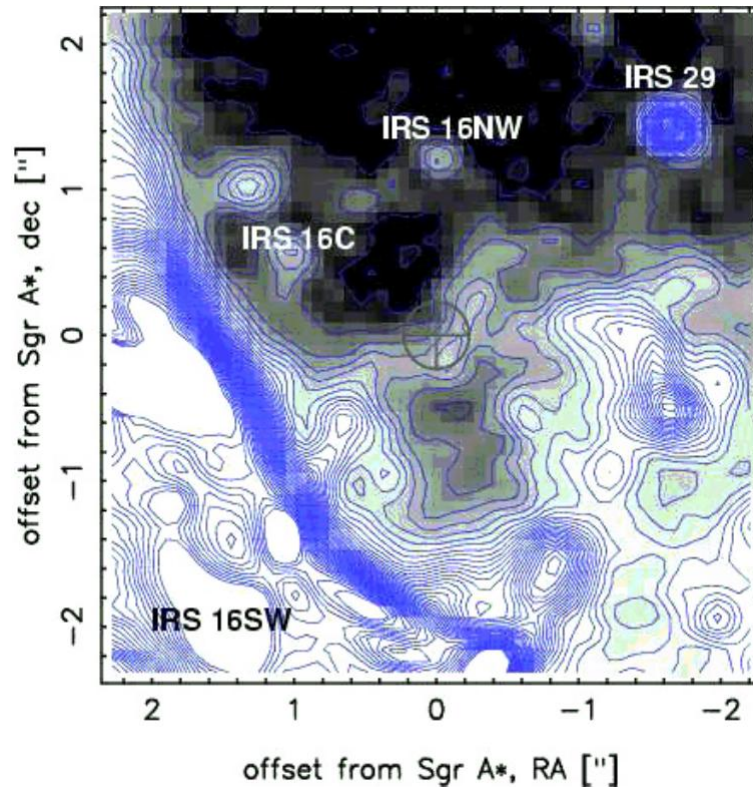
Figure 7-7: The Lucy-Richardson de-convolved and beam-restored image taken at a wavelength of 8.6μm using the VLT VISIR system. We derive fluxes of 22$\pm$5, 21$\pm$5, and 180$\pm$20 mJy for the point sources IRS 16C, IRS 16NW, and IRS29 (without extinction correction). Here the angular resolution is 0.25 arcsec. With METIS we will achieve about 75 mas at the same wavelength (which is an ideal match the the 60 mas K-band resolution obtainable with the VLT).
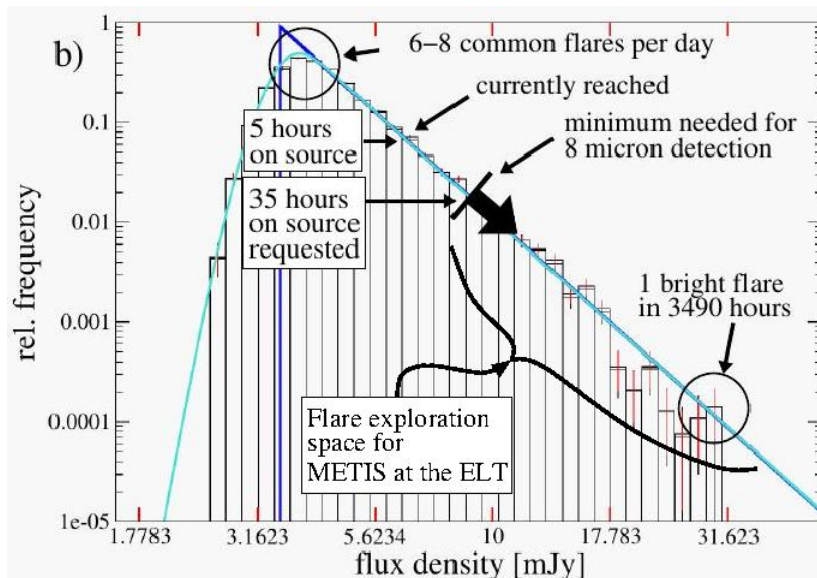
Figure 7-8: Our K-band flare flux histogram by Witzel et al. 2012 covering 7 years of observations with an efficiency of 0.4%. The variable NIR emission can be described well by a single stationary power law process. The peak to the left is the detection limit, the noisy edge to the right is the bright under-sampled end of the histogram.

The contribution of METIS: In the MIR and long-NIR high angular resolution is required to distinguish between the feeble emission from SgrA* and the more extended dust emission of the mini-spiral. The spectral index of SgrA* in the NIR/MIR is not well known. Here synchrotron losses may dominate the spectral shape. Also a variability study in the MIR can only be done efficiently with METIS (sensitivity and resolution). Especially in the MIR region the situation will be complicated, since emission and scattering of dust will contribute to the contamination of the signal from SgrA*. To get photometric values of Sgr A*, dithered imaging exposures of about 60 sec single integration time at L, M and N have to be taken over several nights, to monitor the flaring SgrA*. Stars within the same FoV can be used as photometric standards. If the Sgr A* point source turns out to be bright enough, low resolution spectroscopy at L,M and N could provide helpful information to understand the flare mechanism.

7.3.6   Comparison with other facilities

In the context of METIS it is important to note that the detectability of Sgr A* is not limited by the atmospheric background but by the diffuse emission of the surrounding gas and dust. Thus, studies from space are severely limited by the low spatial resolution and the high surface brightness. METIS on the ELT will be able to detect Sgr A* and measure the broad band fluxes coming from the central ≤ 17 Schwarzschild radii at the most critical wavelengths between L and N band Fig. 7-5.

Even though VLTI can provide even higher spatial resolution due to a baseline of about 100m, the sensitivity is by far not sufficient to observe Sgr A* at MIR wavelengths (MIDI): Its limiting flux at 10μm is around 1 Jy.

Currently, the VLTI project Gravity is working and produced first spectacular results on the Galactic Center (Gravity Collaboration et al. 2017, 2018). GRAVITY is an adaptive optics assisted, near-infrared VLTI instrument for precision narrow-angle astrometry and interferometric phase referenced imaging of faint objects. With a limiting magnitude of up to K=20 mag, this instrument can provide complementary NIR data on Sgr A*, however, limited to the NIR domain, Gravity is no competitor to METIS.

MIRI on JWST will allow for sensitive spectroscopic observations of the Galactic Center. However, the angular resolution of the telescope will be inferior compared to the METIS/ELT combination. Detailed spatial information over a decent field of view in the MIR can only be achieved with METIS.

8 THE PHYSICS OF GALAXIES

8.1 Scientific background and context

Understanding how galaxies formed and evolved remains one of the most challenging issues in modern cosmology. Over the past few years, tremendous progress was achieved in constraining at kilo-parsec scales the nature of the physical processes that drove the build-up of galaxies across cosmic times (e.g., Madau & Dickinson 2014, and references therein). Scaling relations linking fundamental galaxy properties (e.g., stellar mass, star formation rate, gas surface density, central black hole mass, ...) seem to have emerged as soon as the first Giga years of cosmic evolution (Speagle et al. 2014). They suggest that star formation and black hole growth in the distant Universe were mostly governed by internal processes (e.g., gravitational disk instabilities, secular gas consumption) occurring in isolated galaxies and regulated by the feedback action from supernovae and Active Galactic Nuclei (Lilly et al. 2013). In addition, there is also a global consensus on the importance of environmental effects such as galaxy encounters and clustering, which played a critical role in quenching the star-forming activity of blue galaxies and transforming their morphological structure into passive red sources (Hopkins et al. 2010).

On the intermediate sub-galactic scales though, the local conditions and processes that compress the gas and trigger the formation of new stars are still very uncertain. This shortcoming prevents an accurate description of the recipes required to properly reproduce the physical properties of galaxies in current state-of-the-art hydrodynamic simulations of structure formation (e.g., Schaye et al. 2015a). With the ELT we will finally get a chance to unveil the nature of the physical mechanisms at work in highly star-forming environments, by studying in detail the formation of dense and massive star clusters such as those found in nearby luminous infrared galaxies and circum-nuclear starbursts. In addition, we will be able to probe the presence and the properties of nuclear star formation in the vicinity of active galactic nuclei on scales of the order of ~ 10pc or below, which has never been achieved so far. This will allow us to address with unprecedented details how the central star formation connects to the black hole accretion rate, and how the interaction between the two phenomena may have been driving the emergence of the correlation linking the mass of galaxy bulges with the mass of their central super-massive black hole.

8.2 Massive star cluster formation

The massive star clusters hosted in luminous starbursting galaxies are likely different from the massive young clusters known within the Local Group: R136 (LMC), NGC 604 (M33), NGC346 (SMC), NGC3603 (MW), and even most of the super star clusters in the Antennae galaxies, all of which are located in low density environments like galactic spiral arms or dwarf galaxies. The young clusters with masses well in excess of 10^{6-7} M$_\odot$ in the dense environments of luminous starburst galaxies have typical ages up to 10 Myr, luminosities of 10^{8-10} L$_\odot$ and visual extinctions up to several tens of A$_V$. Due to their large distances, compact sizes, and their dense and dusty environment, these stars are very difficult to observe with existing instruments a challenge that can be best, or maybe even solely addressed with the combination of long wavelengths ($>3\mu$m) and high angular resolution as provided by METIS on the ELT.

For illustration, Fig.8-1 shows the circum-nuclear starburst ring in NGC 7552, a face-on galaxy at approximately 20 Mpc distance, as observed with different instruments and telescopes (Spitzer, VLT) at different wavelengths (near-/mid-infrared). The star formation rate in the nine most mid-IR luminous clusters alone equals about four times the total amount of star formation in the entire Milky Way! With [Ne II] line fluxes of a few times 10^{-21} W cm^{-2}, even much fainter clusters will be detected with METIS in a few minutes only. Based on Fig.8-1, two fundamentally important facts need to be stressed, where METIS will make the difference:

- High angular resolution is crucial! Despite diffraction limited performance, the Spitzer Space Telescope cannot resolve the individual clusters. VISIR at 10μm reaches the diffraction limit of the VLT,

corresponding already to about 30 parsecs at NGC 7552. METIS, at the wavelength of the Br-alpha (4.05 μm) line will provide an unsurpassed resolution of 3 parsec with minimal susceptibility to dust reddening. At this resolution, we can finally resolve the substructures of and interaction between embedded massive clusters in a representative sample of nearby starburst galaxies.

- Although less sensitive to dust extinction, the K-band ($\sim$2μm) continuum does not trace the youngest, most massive clusters (M1, M2 in Fig.8-1). Instead, the K-band continuum is dominated by the light from giant and super-giant stars. Even the position of the center of NGC 7552 appears to be offset with respect to the radio peak (and center of the mid-IR ring). In short, wavelengths longer than K-band are essential!
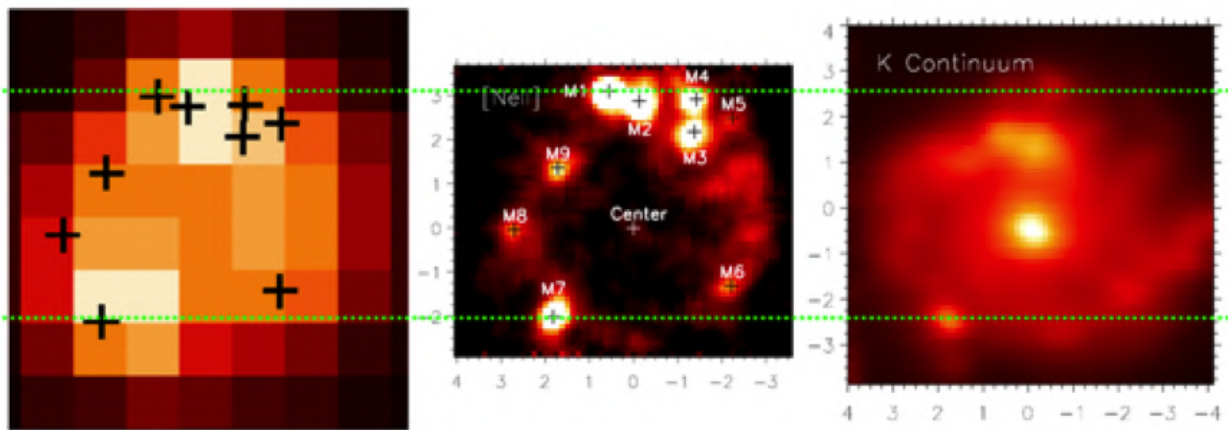
Figure 8-1: Infrared imaging of the circum-nuclear starburst ring in NGC 7552. *Left:* Spitzer-IRAC at 8μm. *Center:* VLT-VISIR [Ne II] at 12.8μm. *Right:* VLT-SINFONI K-band ($\sim$2μm) (Brandl et al. 2012). The black crosses indicate the location of the most mid-IR luminous clusters; the dotted horizontal lines have been added to guide the eye.

Furthermore, METIS on the ELT will provide unique key diagnostics (Brα, [S IV], [Ne II], PAHs, silicates, CO), which enable measurements that are very relevant to a better understanding of the micro-physics of galaxy evolution. Such key investigations are:

- Study the local temperatures and densities of the ionised gas in the most luminous star forming regions from where the next generation of massive stars will (or will not) form.

- Derive the relative ages of the massive clusters to pin down the local star formation histories with respect to triggering and quenching (positive and negative feedback). This may be particularly relevant in regions where the gas supply is localized, e.g., by transport along the nuclear bars.

- Determine the dynamical properties of the clusters from their line shifts, which will lead to a better (virial) mass estimate as well as general insights into the formation scenario. Although significantly over-resolved, Brα observations with the METIS IFU will be ideal for these studies.

- Measure the local physical conditions at the launching pad of galactic-scale jets and outflows (super-winds) to understand the boundary conditions for these dramatic events, which enriched the inter-galactic medium with metals in the early Universe.

Target selection

The constraints imposed by the Adaptive Optics (AO) system that will equip METIS requires the presence of a relatively bright point source ($K < \sim 12$ mag) in the close vicinity of the science target ($r \sim 10$"). In

the case of extragalactic objects, this can not be achieved with a foreground star, because the probability to find such a suitable bright star almost aligned with the target is extremely low. This implies that the METIS observations of starburst sources like NGC 7552 will require in principle the availability of a Laser guide star. In the absence of Laser-assisted AO, a possibility is therefore to select star clusters in relatively nearby luminous galaxies also harboring an active galactic nucleus (AGN), and to use this AGN as a reference point source for the AO guiding.
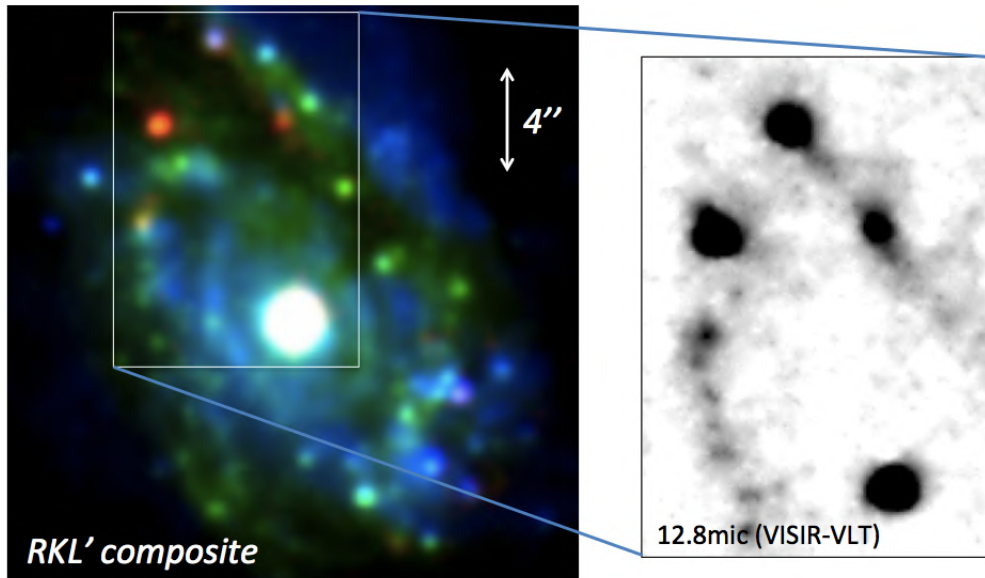
Figure 8-2: Composite image of NGC 1365 obtained from $R-$, $K-$ and L'–band imaging, revealing the bright active galactic nucleus in the core of the galaxy, as well as a large number of massive star clusters throughout the disk. The reddest of these clusters are embedded in dusty regions, requiring observations in the mid-Infrared such as the close-up obtained with VISIR/VLT at 12.8μm (Galliano et al. 2008).

Fig. 8-2 shows the example of NGC 1365, which exhibits a luminous AGN ($K \sim 10$ mag) as well as a wealth of very massive young star clusters in the disk (Galliano et al. 2008). Similar configurations are also found in many other cases like NGC 253, NGC 7469, NGC 1808, showing that METIS will be able to constrain the physics of star formation in massive clusters over a wide range of environments, age, and galaxy physical conditions.

8.3   Nuclear star formation

Over the past few years, observations of local Seyfert's galaxies at high spatial resolution revealed that star formation can be found as close as ~ 10 pc from their central super-massive black hole (see Fig. 8-3). However, we still lack a detailed understanding of the interplay between the AGN activity and the trigger of star formation in the nuclear and circum-nuclear regions of galaxies. Thanks to the exquisite capabilities of METIS on the ELT, we will be able to probe on-going star-forming activity at even higher spatial resolution and shorter distances from galaxy nuclei. Using the spectroscopic mode of METIS in the N-band, we will use the PAH feature at 11.3μm as a key diagnostic for probing star formation and disentangling its signature from that of the nuclear emission (e.g., Mori et al. 2014; Alonso-Herrero et al. 2014; Ramos Almeida et al. 2014). The angular resolution of METIS will allow us to search for recent star formation not only around type 2 AGNs, but presumably also around some type 1 Seyferts. We will explore how this activity of star formation correlates with the black hole accretion rate (e.g., Esquej et al. 2014a). Finally, we will investigate if the dust collocated with the gas that fuels the nuclear star formation can play a role in the obscuration of type 2 AGNs (Hicks et al. 2009), and if this dust is partially related to the clumpy torus emission often invoked in the unified scheme of active nuclei.
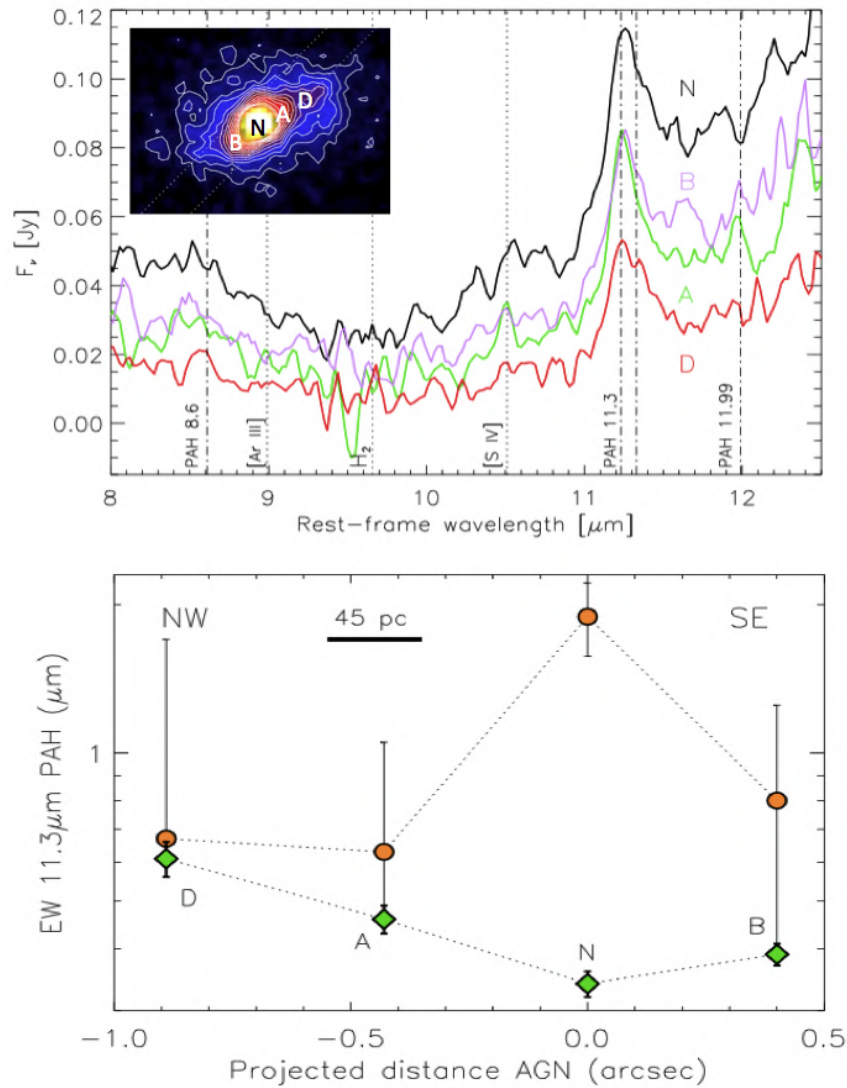
Figure 8-3: *Top:* Mid-Infrared spectra obtained in the core region of Mrk 1066, showing the presence of star formation in the vicinity of the nucleus through the detection of the PAH 11.3μm. The spectra were extracted at the 4 locations shown in the inset (A, N, B and D). The distance between B and N is typically ~ 100 pc. *Bottom:* the PAH equivalent width derived from the 4 spectra as a function of the projected distance from the nucleus, before and after subtracting the contribution from the AGN (green and orange symbols, respectively). Adapted from Alonso-Herrero et al. (2014) and Ramos Almeida et al. (2014).

9 ACTIVE GALACTIC NUCLEI

9.1 Scientific background and context

In recent years is has become clear that super-massive black holes (SMBHs) form an integral part of galaxy nuclei and that they are closely linked to the large-scale properties of galaxies. The fact that the black hole mass and total galaxy mass are closely related is truly remarkable, given that there is a factor of 10^8 between the AU-size Schwarzschild radius of the black hole and the kpc-size dimension of the galaxy. This is generally interpreted as evidence that the formation and growth of the SMBH is directly related to the formation process of the stellar population, e.g. in a violent burst of star formation. While an intimate connection between star formation and SMBH growth nowadays is included in all major cosmological simulations (e.g. Schaye et al. 2015b), the actual physical processes giving rise to the black hole – spheroid mass cor-

relation are not understood at all. Popular scenarios include feedback from AGNs dispersing the gas that feeds both starburst and AGN, and Eddington-limited starburst activity with radiation pressure from the starburst dispersing the gas (e.g. Murray et al. 2005). To understand this conspiracy, reliable measurements of SMBH masses in a range of galactic nuclei, including inactive galaxies, AGNs and starburst galaxies, are indispensable.

Similarly important, and directly related, is the issue of the immediate vicinity of the SMBH. In the standard model of AGNs, the black hole and its hot accretion disk are surrounded by an obscuring dusty torus, and the dichotomy between type 1 and type 2 AGNs results from different viewing angles. Data on the size and geometry of this torus are extremely scarce; only for the most nearby Seyfert galaxies, the innermost regions have been probed through interferometric VLTI observations. Rather than confirming this unification model, these observations have mainly revealed the diversity of the nuclear environments Burtscher et al. (2016).

Finally, on slightly larger scales, the mechanisms by which gas can loose its angular momentum and fall into the nuclear region, fuelling both nuclear starbursts and AGNs, are poorly understood. High-resolution imaging and spectroscopic studies have mapped the morphology and dynamics of some nearby galaxies (e.g. Prieto et al. 2014; Hicks et al. 2013; Rosario et al. 2019), but the physical mechanism for fuelling AGNs and the possible link with nuclear starbursts remains far from being understood. There is currently no consensus on whether AGN fuelling must be synchronous with nuclear star formation (Esquej et al. 2014b), is only sometimes so (Cid Fernandes et al. 2004), follows it during a post-starburst phase (Davies et al. 2007; Vollmer et al. 2008), or is not associated with any recent star formation in the vicinity of the AGN (Sarzi et al. 2007).

High-resolution imaging and integral-field spectroscopic studies of nearby active galaxies are necessary to trace the structure and dynamics of the gas and to resolve star-formation activity in the close vicinity of the AGN. The current instrumentation has allowed us to zoom into the central region of AGNs (see Fig. 9-1), but it has now reached its limits to investigate the nuclear and circum-nuclear regions of galaxies. Fundamental problems are twofold:

- **Obscuration**   The nuclear regions of AGNs are often so strongly obscured that even near-infrared observations are not sufficient to peer into the nucleus and witness the fuelling of an AGN and/or starburst. The nearby AGN NGC 4945 is a remarkable example: variable hard X-ray emission unambiguously reveals the presence of an AGN, yet the obscuration is so large ($A_V > 50$) that no evidence for an AGN is found at optical or even near-infrared wavelengths.

- **Spatial resolution**   Very high spatial resolution is required to resolve the region of dynamical influence of the black hole. In particular, in order to determine SMBH masses using dynamics (a well-developed technique at shorter wavelengths, using both gas and stellar dynamics) it is necessary to resolve the radius of influence of the SMBH. Using the empirical relation between SMBH mass and velocity dispersion (Ferrarese & Merritt 2000; Gebhardt et al. 2000), the radius of influence can be written as:

$$\theta_{\mathrm{BH}} = 0.03'' \left(\frac{M_{\mathrm{BH}}}{10^8 M_\odot} \right)^{0.5} \left(\frac{100 \,\mathrm{Mpc}}{D} \right) \tag{1}$$

  With 8m class telescopes, this can only be resolved for the most nearby galaxies and most massive black holes.

METIS at the ELT provides the unique opportunity to investigate the nuclei of local AGNs by mapping gas flows and measuring dynamic black hole masses. The very large obscuration towards these nuclei necessitates the use of the longest accessible wavelengths, and therefore favours METIS. Combined with the spatial resolution provided by an ELT, a direct dynamical probe of black hole masses in obscured galactic nuclei will for the first time be possible. Finally, combining imaging with integral field spectroscopy, the structures and gas dynamics in the nuclear regions can be mapped and the relation between star formation
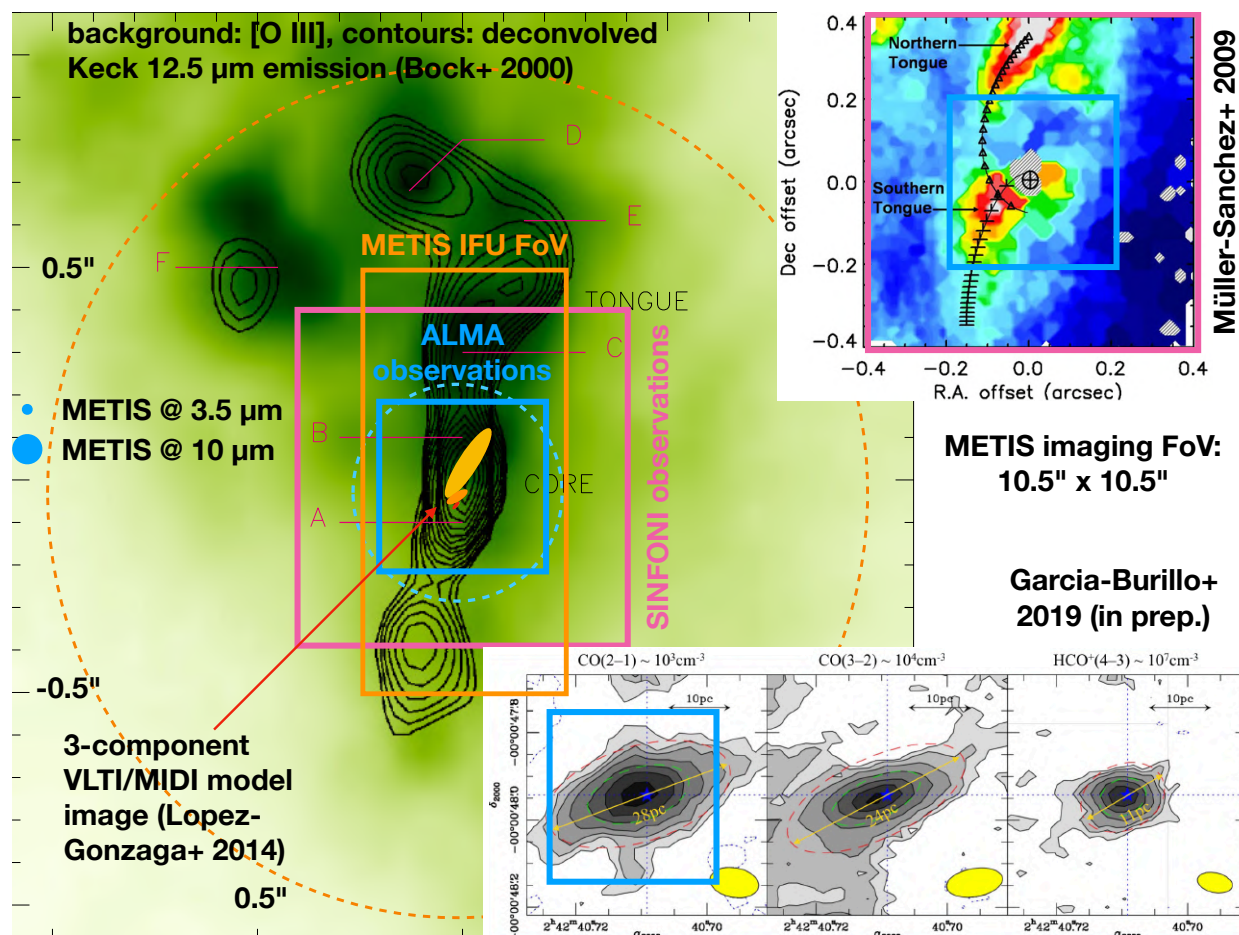
Figure 9-1: The modern view of the complex AGN "torus" region: The largest panel shows an overlay of an optical image in the [OIII] line with a deconvolved 12.5 μm image in contours (Bock et al. 2000). On top of the contours, we show the three component model image derived with VLTI/MIDI (López-Gonzaga et al. 2014). The blue dots in the center left of this panel show the METIS PSF at 3.5μm and at 10μm, respectively, and the orange rectangle indicates the field of view of the METIS L and M band high-resolution integral-field spectrograph. The blue and purple squares allow to compare to the fields of view of the SINFONI (Müller-Sánchez et al. 2009) and ALMA (Garcia-Burillo et al. 2019, in prep.) observations shown in the upper right and lower right panels, respectively, and to the same scale. While the mid-IR continuum emission is interpreted as being part of the outflowing Narrow Line Region, the near-IR "tongues", seen in the light of hot molecular hydrogen (the 1-0 S(1) line), have been interpreted as inflow. The ALMA observations, on the other hand, show a rotating disk with superposed non-circular motions in the lines of CO and HCO$^+$.

and black hole growth can be investigated in a systematic way. Specific questions that will be answered include:

1. What are the masses of the SMBHs in the nuclei of nearby AGNs?

2. How is the SMBH fed during the phase of mass buildup?

3. Do stellar mass and SMBH mass build up simultaneously in AGNs, or does one component precede the other?

4. Is the star formation process terminated by feedback from the SMBH?

5. How does feedback from the starburst affect the environment?

6. What is the fate of the gas that is left over after star formation has terminated?

7. (How) is this gas related to the circum-nuclear obscuring torus?

8. What is the size and geometry of the circum-nuclear torus?

9. Does the circum-nuclear torus have a central cavity and how does gas in this region flow towards the accreting SMBH?

10. How does the warm AGN-heated dust on circum-nuclear scales relate to the cold gas seen by ALMA on similar scales and to the hot dust seen by VLTI on parsec scales?

11. Which of them, if any, can be identified as *the* torus?

It is worth noting that an instrument like METIS primarily observes continuum emission from dust at 100-800 K, but is also sensitive to Br α, coronal lines like [SiIX], [ArVI] and [AlVI], molecular lines of CO and H2O, and broad silicate emission and absorption lines. Examples of spectral features in the atmospheric *L*, *M* and *N* bands are shown in Fig. 9-2, 9-5 and 9-6 respectively.

9.2   High-resolution imaging of the AGN "torus" region

The AGN "central engine", in the broader sense, contains many components. In order of increasing size these include the **SMBH**, the (nuclear) radio jet, the surrounding hot accretion disk, the **Broad Line Region** (BLR), the dusty **obscuring structure** or **torus**, the **Narrow Line Region** (NLR), and the circum-nuclear star-forming region. Material flows inward through these regions in reverse order, while radiation and kinetic energy flow outward into the surrounding galaxy. Historically each region has been discovered using different instrumental techniques and often at different wavelengths from radio to gamma rays. Astronomers analyzed the conditions and physical properties independently for each region.

In the past decade theoreticians have begun to break the artificial barrier between the BLR, the "torus" and the NLR, showing that they are part of a single physical system (e.g. Czerny & Hryniewicz 2011; Baskin & Laor 2018; Vollmer et al. 2018). The material travelling inward passes smoothly through a transition where dust sublimates and the nuclear UV ionizes the clouds that form the BLR. In this transition region, the radiation pressure from UV photons reprocessed into the infrared lifts material out of the accretion plane into winds and fountains that redistribute matter and energy into the NLR (e.g. Schartmann et al. 2014; Wada et al. 2016). Besides finally clarifying the mechanism that supports thick dusty accretion disks against the gravity of the SMBH, this model also explains the recently confirmed prevalence of *polar* infrared emission from the central engine region (Asmus et al. 2016; López-Gonzaga et al. 2016), see Fig. 9-3. By resolution and sensitivity, METIS will be the ideal instrument to probe this polar dust emission, i.e. the base of the AGN outflow, in a large number of AGNs, see Fig. 9-4.

The physics of these regions is particularly relevant to the context of the larger surrounding galaxy because this is where winds and non-relativistic outflows are formed that are the main channels of energy transport to the ISM. Feedback at different epochs and in different environments cannot be understood until the physics of dusty accretion are understood. Key questions include:

- What are the physical conditions of the accreting dust systems that surround AGNs at $\approx 1 - 100$ pc radius? Are they turbulent? Are they heated by nuclear UV- and X-ray radiation and is infrared radiation pressure as dominant as recent models predict? Observations with VLTI/MIDI have shown that the structures vary considerably from galaxy to galaxy (Burtscher et al. 2013), and do not always align perpendicular to radio axes (López-Gonzaga et al. 2016).

- Is the unified model of AGNs still useful or does it rather prohibit us from seeing the full complexity of these regions? Seyfert 1 and Seyfert 2 galaxies are classically interpreted as hosting an identical AGN seen face-on or edge-on, respectively. Statistical investigations have shown, however, that the dust structures in these two types of AGNs are in fact physically different: Seyfert 2 galaxies have
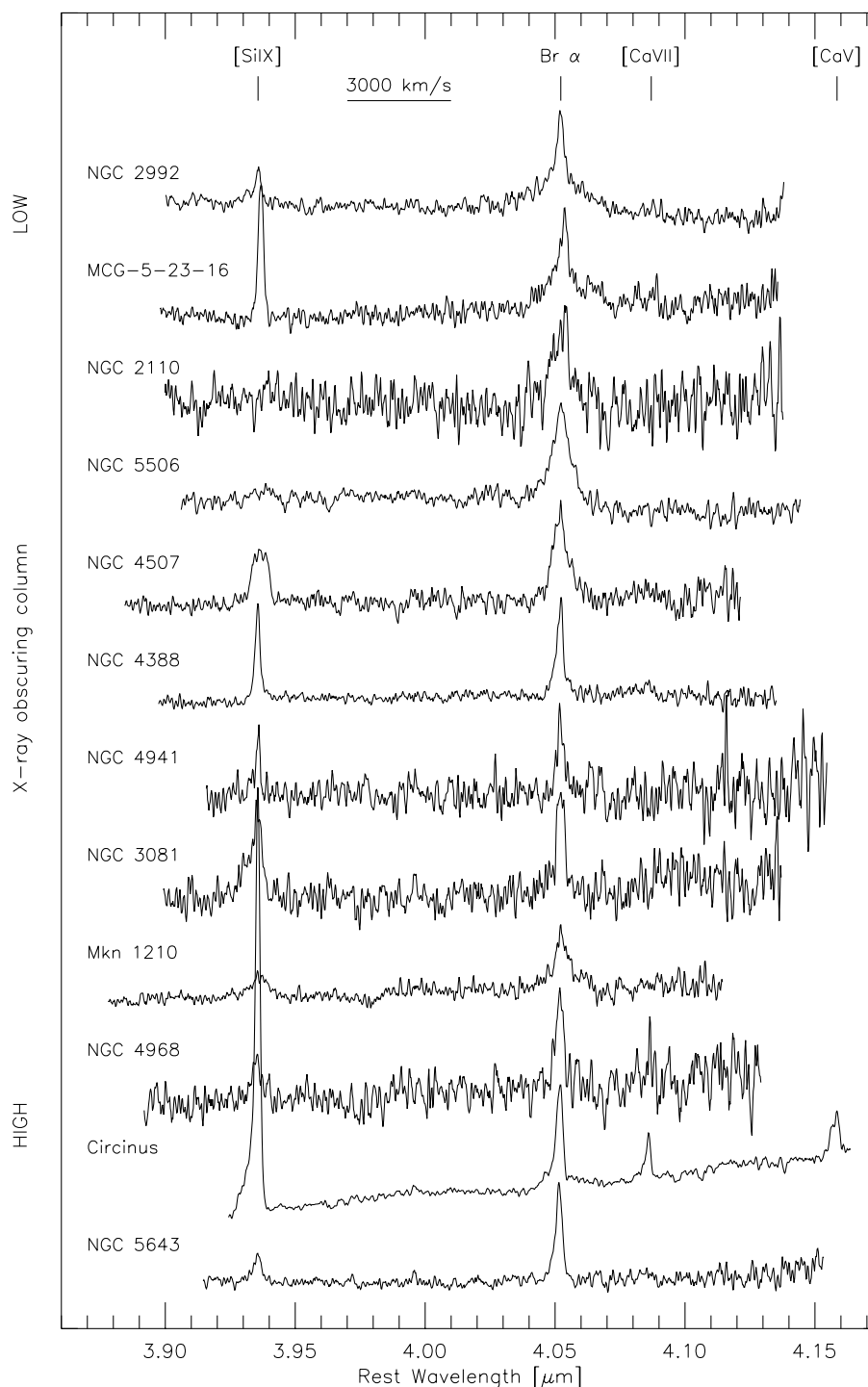
Figure 9-2: VLT/ISAAC 4 μm spectra of twelve local Seyfert 2 galaxies showing that Br-α as well as the coronal line [Si IX] are strongly detected in nearly all of these galaxies. From Lutz et al. (2002)

more dust clouds that also cover a larger solid angle and may represent a different accretion state (Ramos Almeida et al. 2011).

- Is the dust composition affected by the transition from the BLR to the dusty outflow? Some silicate absorption features indicate non-standard dust compositions, but the signal-to-noise rate and the spatial resolution of existing observations is too low to make conclusive statements. Existing mid-IR spectra of AGNs typically show a diversity of Silicate absorption and emission features and this is
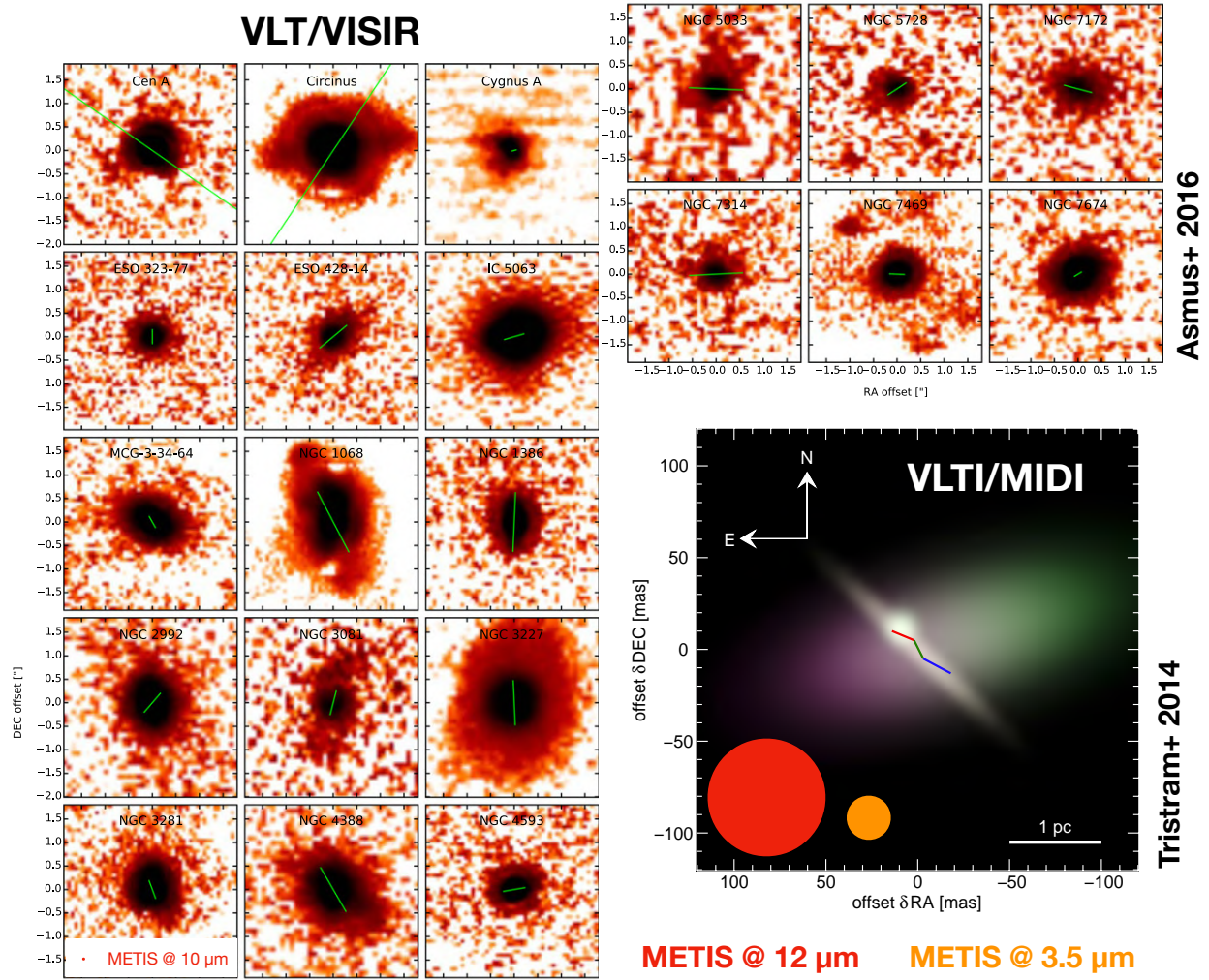
Figure 9-3: Polar dust in nearby Seyfert galaxies as seen by VLT/VISIR (Asmus et al. 2016) and VLTI/MIDI (López-Gonzaga et al. 2016) on scales of $\approx$ 100 pc and 1 pc, respectively. In the panel with the MIDI model image, we also show the PSF of METIS at L and N band as orange and red disks, respectively.

not as straight-forwardly related to the optical (Seyfert 1/2) classification as one might expect (see Fig. 9-6).

- How is energy fed back from the inner regions of AGNs to the surrounding galaxy? The majority of this feedback, at least in lower luminosity AGNs, is probably not from radio jets, but from interaction with winds from the inner edge of the dust disk. Mid-IR observations of NGC 1068 show the polar hot dust (see Fig. 9-3) and coronal lines of [SiIX] possibly arising from wind-induced shocks.

- Where does the dusty material come from? The most obvious source is circum-nuclear star clusters. What processes allow material at 100 pc to dump angular momentum? Does this material spiral in quietly or is it grossly turbulent? Why doesn't it form stars? The region outside 10 pc is too big and too faint for MIDI/MATISSE to map dust and CO or Br α emission lines, but METIS will have the right field of view and sensitivity to bridge the gap between VLTI and ALMA observations.

Observations of the obscured central regions, to comparable resolutions, can also be obtained with ALMA, in its most extended configurations, and the most luminous objects. So far, a clear detection of the torus, separated from the surrounded medium, has only been possible in the continuum, for the bright nearby Seyfert galaxy NGC 1068 (García-Burillo et al. 2016, see also Fig. 9-1). Remarkably, ALMA observations
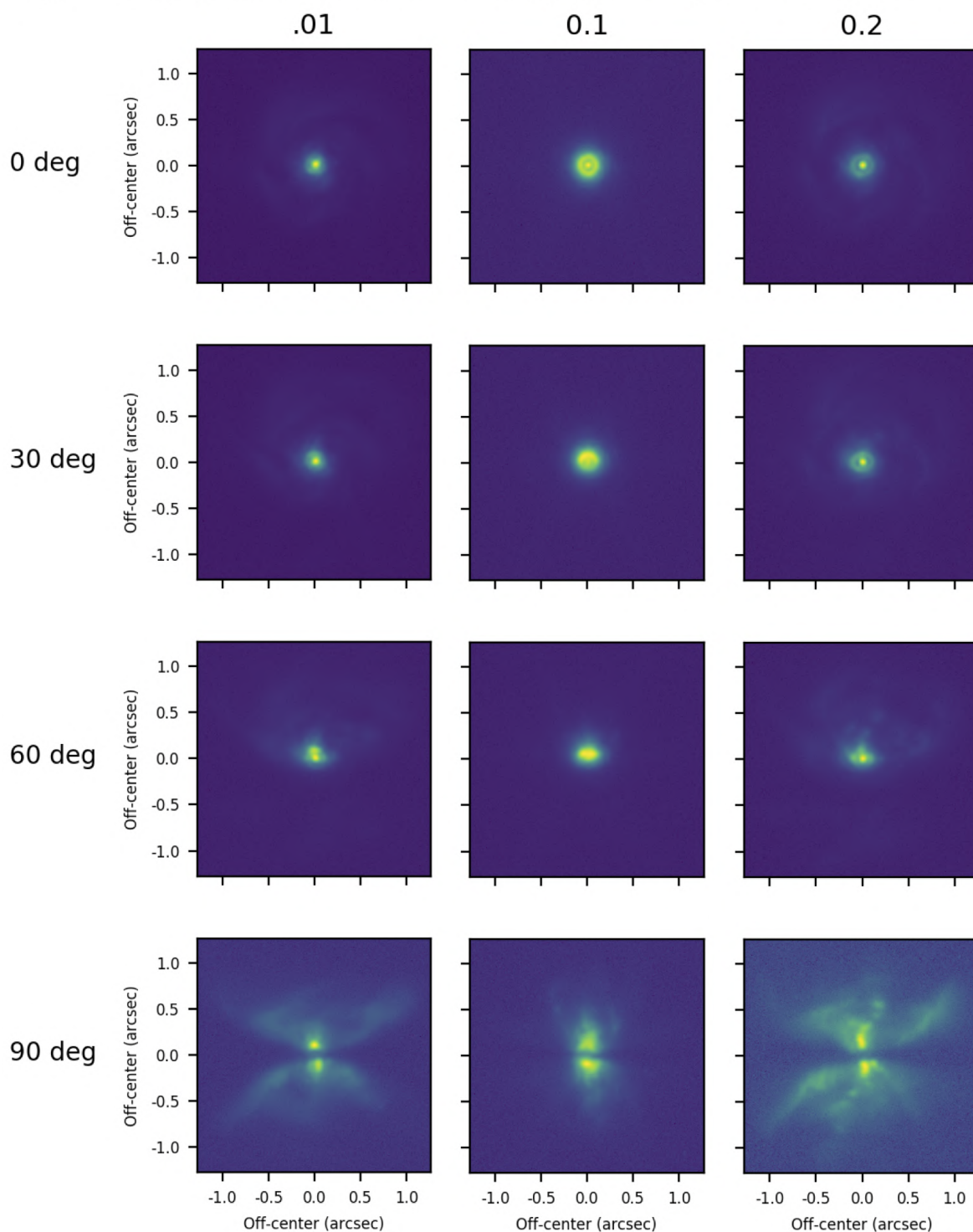
Figure 9-4: Simulated METIS images (using the METIS data simulator *SimMETIS*) of the "torus" region of a nearby faint AGN, simulated as a radiation-driven dusty outflow by Schartmann et al. (2014). The rows show different inclinations of the central disk while the columns shown models with Eddington ratios varying from 1% (left) to 10% (center) and 20% (right).
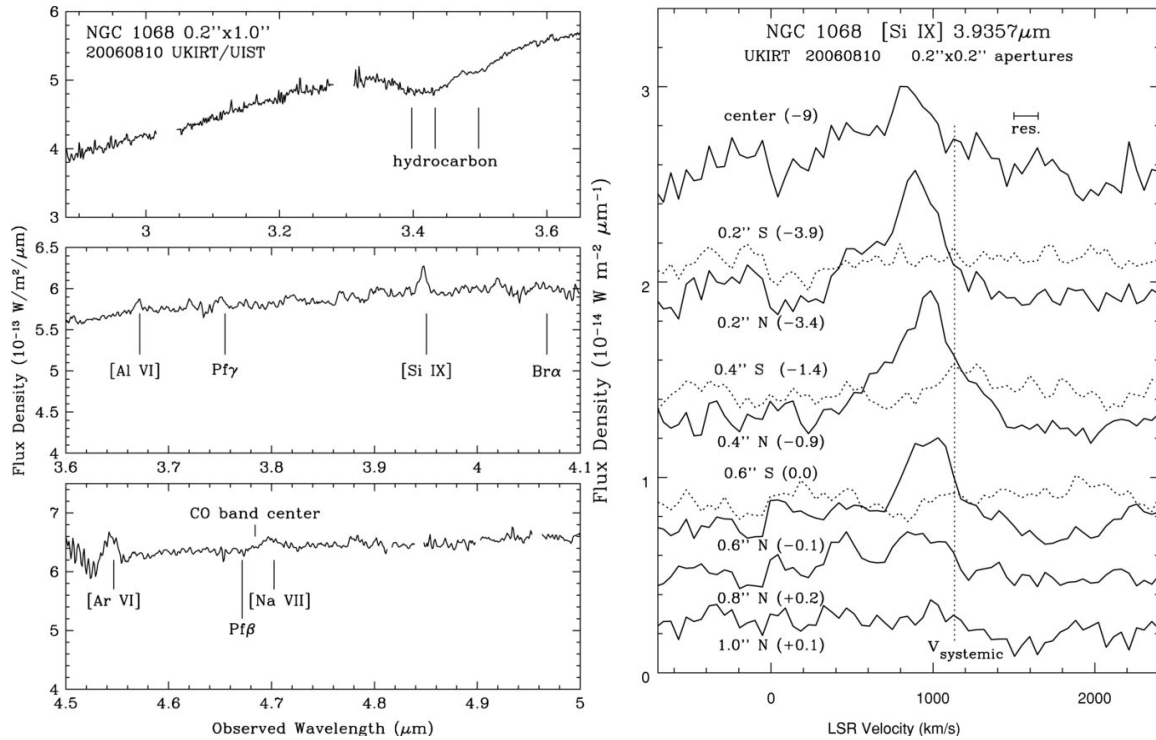
Figure 9-5: Left: 35 μm spectrum of the central $0.2'' \times 1.0''$ (EW × NS) region of NGC 1068. Wavelengths of atomic lines of interest are shown, as are the three components of the 3.4 μm hydrocarbon feature and the band center of CO, all at the systemic redshift of NGC 1068. Right: Velocity profiles of the [Si IX] line in $0.2''$ steps along the slit. The continuous lines denote spectra at the center and to the north; the dashed lines indicate spectra to the south. Numbers in parentheses are continuum offsets. The y-axis is flux density in a $0.2'' \times 0.2''$ aperture. From Geballe et al. (2009).

of one of the nearest prominent AGNs, the radio galaxy Centaurus A do not show any emission of molecular lines in the region close to the AGN (McCoy et al. 2017), while near-IR molecular hydrogen emission is strong (Neumayer et al. 2007). The most likely explanation is that molecules other than H_2 are either in extremely highly excited states or, more likely, destroyed in the harsh radiation environment of the AGN. This indicates that molecular lines in the ALMA region are good for probing the torus environment, but not the torus itself, which can be probed through near- and mid-infrared spectroscopy. METIS and ALMA observations are thus highly complementary, and the combination of both is essential for understanding these complex regions.

The specific role of ELT/METIS in unwinding this complexity is its combined high spatial and spectral resolution and high sensitivity. The other relevant instruments that will be operating at the same time are the VLTI (MATISSE+GRAVITY), ALMA, and the JWST. Of these the VLTI has the highest spatial resolution (2-10 milli-arcseconds in the K and N bands respectively), but is sensitivity-limited to a few tens of nearby Seyfert galaxies. The sensitivity limit particularly limits possible kinematic studies because the CO and Hydrogen emission line strengths from the inner dust regions seem to be quite low. The resolution of ALMA is only slightly lower and its spectral resolution is high. Its longer wavelength coverage is optimum for studying the colder regions between the star-forming ring and the outer dust disk, rather than the hotter BLR-dust transition where most of the energy is emitted in the infrared. Finally, the JWST has superb sensitivity and spectral coverage, but has a spatial resolution (135–400 milli-arcseconds in the wavelength range that METIS will cover) that is too small to resolve the processes in the "torus" region

We expect the primary contributions of METIS to be:

- Follow the kinematics, chemistry, and dynamics of the dusty/molecular accretion flow in nearby Seyfert galaxies from the colder outer regions ($T \sim 30$ K) towards the sublimation zone ($T \sim 1500$

K) through mapping of molecular and recombination lines in the mid-IR.

- Similarly, in the same galaxies, follow the acceleration of this material, presumably by radiation pressure, into dusty polar winds towards the NLR.

- Extend these studies, with limited spatial resolution, to hundreds of galaxies, in order to trace how these AGN flows interact with the inward and outward transport of mass, momentum, and energy with the host galaxy and surrounding environment.

9.3   Black hole masses in nearby obscured AGNs

As argued in Section 9.1, systematically measuring SMBH masses in significant samples of galaxies is indispensable to understand the link between black hole growth, star formation and galaxy evolution. These samples of galaxies need to contain different subsamples, including inactive galaxies with "sleeping" SMBHs, AGNs and (U)LIRGs. For the first category, characterized by modest amounts of obscuration, optical or near-infrared observations are suitable and the techniques to measure SMBH masses based on stellar and/or gas kinematics have reached a reasonable level of maturity. AGNs and (U)LIRGs on the other hand are typically obscured by large amounts of dust, such that mid-infrared observations are required to probe their nuclear regions.
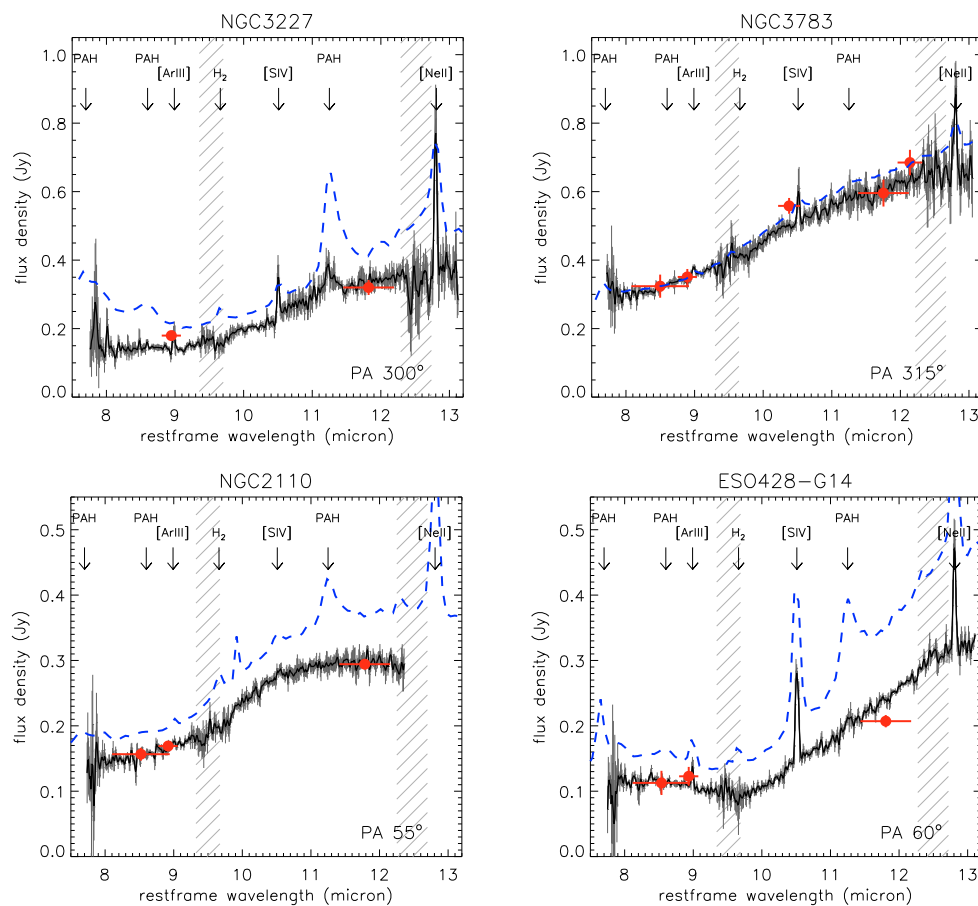
Figure 9-6: A collection of *N* band spectra from Seyfert 1 (top row) and Seyfert 2 (bottom row). The black line is the spectrum obtained from VLT/VISIR and the blue dashed line is a Spitzer spectrum for comparison. The red dots are photometric measurement from VLT/VISIR. Prominent mid-IR emission lines are marked. In the lower right panel the broad absorption band of Silicates (centered at ≈ 9.7 μm) can easily be seen in the Seyfert 2 galaxy ESO 428-G14. From Hönig et al. (2010).

Target	D [Mpc]	M_{BH} [$M_\odot$]	θ_{BH} [$''$]	Notes
Cen A	3.5	$4.5\ldots5.5\cdot10^7$	0.6	Neumayer et al. (2007); Cappellari et al. (2009)
Circinus	3.9	$1.3\cdot10^6$	0.09	Greenhill et al. (2003)
NGC 4945	7.3	$3.8\cdot10^6$	0.09	Greenhill et al. (1997)
NGC 1068	14	$1.0\cdot10^7$	0.07	Greenhill et al. (1996)
NGC 7582	21	$5.5\cdot10^7$	0.11	Wold et al. (2006)
Arp 220	70	$\approx10^8$	0.06	Black hole mass estimated
NGC 6240	100	$\approx10^8$	0.03	Black hole mass estimated

Table 9-1: Black hole masses and radii of influence for nearby AGNs and (U)LIRGs.

Tab 9-1 lists relevant parameters of nearby obscured AGNs and (U)LIRGs with representative key METIS observations. The black hole masses of Circinus, NGC 4945 and NGC 1068 in this table come from VLBI measurements of H_2O maser emission, but the black hole mass of NGC 7582 has been determined using mid-infrared spectroscopy of the [Ne II] 12.8 μm line at the diffraction limit of VISIR/VLT, demonstrating the promise of mid-infrared spectroscopy for these observations (Wold et al. 2006). The high-resolution integral-field spectrograph in the L and M bands will allow METIS to perform such observations in about 30–100 AGNs.

As can be seen from Tab 9-1, at the resolution of the VLT the radius of influence of the SMBH is approached, but not resolved. However, at the higher resolution provided by an ELT, the full Keplerian motion of the gaseous disk will be revealed. METIS therefore opens up the detailed study of dynamics and gas flow in accreting gas disks in obscured AGNs, and will not be limited to the subset of AGNs that have luminous H_2O maser emission. This allows a much more statistically robust approach than hitherto possible.

9.4   A representative AGN observing program for METIS

1. Mapping of CO or Br-alpha kinematics from warm dusty disks. No kinematic information is currently available, and CO and Br-alpha fluxes are low (Geballe et al. 2009). This information would be the first indication of whether the accretion is smooth or turbulent, whether ionized material is blown of the tops of disks as winds.

2. Mapping of dust continuum emission beyond radii available to VLTI MIDI/MATISSE. This is partly a field-of-view issue (VLTI limited to 0".25) and partly a surface brightness sensitivity issue. The prime interests are to trace the infall of material from the circumnuclear stellar regions, and to trace dust and gas being blown out as winds. One can include in this mapping of PAH emission. This is not seen at all in MIDI maps, indicating that PAHs near the nucleus are destroyed by nuclear UV/X-rays. Mapping the PAHs at larger radii will diagnose the nuclear radiation fields and its effect on the inflowing gas (Jensen et al. 2017).

3. Map coronal line emission from jet/wind interaction regions. Once again MATISSE sensitivity is probably too low except for the few nearest galaxies. Understanding this interaction is critical to feedback physics.

4. Probe the mid-IR/X-ray relation for AGNs. The mid-IR flux indicates the conversion efficiency of nuclear UV/X-rays to IR, and thus typically measures the dust-covering fraction (fraction of sky covered by dust as seen by the nucleus). This is a critical number for testing AGN unified models, and evolution of accretion phenomenon with cosmic time. Current single dish observations cannot separate nuclear IR from that at larger radii (circumstellar star regions, spiral arms) and MATISSE is not sensitive enough for a large sample.

A   METIS OBSERVING MODES

Science Observing Mode	Instrument Configuration						Science Driver
	Sub-Syst.	Band	IFS Setting	HCI Mask	PT	FT	
Direct Imaging	IMG	L,M	N/A	N/A	•	•	circum-stellar (YSOs) and circum-nuclear (AGN) structures, star clusters
	IMG	N,Q	N/A	N/A	•	•	circum-stellar (YSOs) and circum-nuclear (AGN) structures
High Contrast Imaging	IMG	L,M	N/A	RAVC/CVC	•		exoplanets (detection + characterization)
			N/A	APP	•		
			N/A	CLC	•		
	IMG	N	N/A	CVC	•		exoplanets (detection + characterization)
			N/A	CLC	•		AGB stars
Longslit spectroscopy	IMG	L,M	N/A	N/A		•	ices in comets and star forming regions
	IMG	N	N/A	N/A		•	physics of circum-stellar and circum-nuclear environments; sold-state chemistry & mineralogy
IFU spectroscopy	LMS	L,M	full IFU field	N/A	•	•	kinematics and chemistry of circum-stellar environments
	LMS	L,M	spectral IFU Δλ~300nm	N/A	•	•	chemical studies of the interstellar medium
IFU+HCI spectroscopy	LMS	L,M	full IFU field	APP	•		exoplanetary atmospheres at $\theta > 3\lambda/D$, pp-disks
				RAVC/CVC	•		exoplanetary atmospheres at $\theta \sim 2\lambda/D$, pp-disks
				CLC	•		very bright stars, AGB stars
	LMS	L,M	spectral IFU Δλ~300nm	APP	•		exoplanetary atmospheres at $\theta > 3\lambda/D$
				RAVC/CVC	•		exoplanetary atmospheres at $\theta \sim 2\lambda/D$
				CLC	•		very bright stars, AGB stars

Figure 1-1: The five science observing modes of METIS. The acronyms stand for: CLC – Classical Lyot Coronagraph (for partly resolved targets); CVC – Classical Vortex Coronagraph (for highest throughput); RAVC – Ring-apodized Vortex Coronagraph (for highest nominal performance); APP – Apodized Phase Plate (most robust against vibrations). Pupil tracking (PT) and field tracking (FT) modes are indicated by black dots.

REFERENCES

Ábrahám, P., Juhász, A., Dullemond, C. P., et al. 2009, Nature, 459, 224

Absil, O., Milli, J., Mawet, D., et al. 2013, A&A, 559, L12

Alexander, R., Pascucci, I., Andrews, S., Armitage, P., & Cieza, L. 2014, Protostars and Planets VI, 475

Allison, R. J., Goodwin, S. P., Parker, R. J., et al. 2009, ApJL, 700, L99

ALMA Partnership, Brogan, C. L., Pérez, L. M., et al. 2015, ApJ, 808, L3

Alonso-Herrero, A., Ramos Almeida, C., Esquej, P., et al. 2014, MNRAS, 443, 2766

Altwegg, K., Balsiger, H., Berthelier, J. J., et al. 2017, Monthly Notices of the Royal Astronomical Society, 469, S130

Andrews, S. M., Huang, J., Pérez, L. M., et al. 2018, ApJL, 869, L41

Anglada-Escudé, G., Amado, P. J., Barnes, J., et al. 2016, Nature, 536, 437

Antonellini, S., Kamp, I., Riviere-Marichalar, P., et al. 2015, A&A, 582, A105

Armitage, P. J. 2011, ARA&A, 49, 195

Asmus, D., Hönig, S. F., & Gandhi, P. 2016, ApJ, 822, 109

Avenhaus, H., Quanz, S. P., Garufi, A., et al. 2018, ApJ, 863, 44

Ayliffe, B. A. & Bate, M. R. 2009, MNRAS, 393, 49

Backman, D. E. & Paresce, F. 1993, in Protostars and Planets III, ed. E. H. Levy & J. I. Lunine, 1253–1304

Balick, B. & Frank, A. 2002, ARA&A, 40, 439

Banzatti, A., Pascucci, I., Edwards, S., et al. 2019, ApJ, 870, 76

Banzatti, A. & Pontoppidan, K. M. 2015, ApJ, 809, 167

Banzatti, A., Pontoppidan, K. M., Salyk, C., et al. 2017, ApJ, 834, 152

Baraffe, I., Chabrier, G., Barman, T. S., Allard, F., & Hauschildt, P. H. 2003, A&A, 402, 701

Baskin, A. & Laor, A. 2018, MNRAS, 474, 1970

Bast, J. E., Brown, J. M., Herczeg, G. J., van Dishoeck, E. F., & Pontoppidan, K. M. 2011, A&A, 527, A119

Bastian, N., Covey, K. R., & Meyer, M. R. 2010, ARAA, 48, 339

Batygin, K., Bodenheimer, P., & Laughlin, G. 2009, ApJL, 704, L49

Beichman, C. A., Tanner, A., Bryden, G., et al. 2006, ApJ, 639, 1166

Berné, O. & Tielens, A. G. G. M. 2012, Proceedings of the National Academy of Science, 109, 401

Béthune, W., Lesur, G., & Ferreira, J. 2017, A&A, 600, A75

Beuermann, K., Hessman, F. V., Dreizler, S., et al. 2010, A&A, 521, L60

Beuther, H., Linz, H., Henning, T., Feng, S., & Teague, R. 2017, A&A, 605, A61

Birkby, J. L. 2018, Spectroscopic Direct Detection of Exoplanets, 16

Birkby, J. L., de Kok, R. J., Brogi, M., et al. 2013, MNRAS, 436, L35

Birkby, J. L., de Kok, R. J., Brogi, M., Schwarz, H., & Snellen, I. A. G. 2017, AJ, 153, 138

Birnstiel, T., Dullemond, C. P., & Pinilla, P. 2013, A&A, 550, L8

Birnstiel, T., Fang, M., & Johansen, A. 2016, Space Sci. Rev., 205, 41

Bjerkeli, P., van der Wiel, M. H. D., Harsono, D., Ramsey, J. P., & Jørgensen, J. K. 2016, Nature, 540, 406

Bladh, S. 2018, IAU 343, invited review [[IAU343]1809.10583]

Bladh, S. & Höfner, S. 2012, A&A, 546, A76

Blake, G. A. & Boogert, A. C. A. 2004a, ApJ, 606, L73

Blake, G. A. & Boogert, A. C. A. 2004b, ApJL, 606, L73

Bock, J. J., Neugebauer, G., Matthews, K., et al. 2000, AJ, 120, 2904

Böhnhardt, H., Mumma, M. J., Villanueva, G. L., et al. 2008, The Astrophysical Journal Letters, 683, L71

Boley, P. A., Linz, H., van Boekel, R., et al. 2013, A&A, 558, A24

Bollen, D., Van Winckel, H., & Kamath, D. 2017, A&A, 607, A60

Bonavita, M., de Mooij, E. J. W., & Jayawardhana, R. 2013, PASP, 125, 849

Bonnell, I. A. & Bate, M. R. 2006, MNRAS, 370, 488

Bonnell, I. A. & Smith, R. J. 2011, in IAU Symposium, Vol. 270, Computational Star Formation, ed. J. Alves, B. G. Elmegreen, J. M. Girart, & V. Trimble, 57–64

Booth, R. A., Clarke, C. J., Madhusudhan, N., & Ilee, J. D. 2017, MNRAS, 469, 3994

Borucki, W. J., Koch, D. G., Basri, G., et al. 2011a, ApJ, 736, 19

Borucki, W. J., Koch, D. G., Basri, G., et al. 2011b, ApJ, 736, 19

Bosman, A. D., Bruderer, S., & van Dishoeck, E. F. 2017, A&A, 601, A36

Bouwman, J., Castellanos, P., Bulak, M., et al. 2019, A&A, 621, A80

Bouwman, J., de Koter, A., Dominik, C., & Waters, L. B. F. M. 2003, A&A, 401, 577

Bouwman, J., Meeus, G., de Koter, A., et al. 2001, A&A, 375, 950

Brandl, B. R., Martín-Hernández, N. L., Schaerer, D., Rosenberg, M., & van der Werf, P. P. 2012, A&A, 543, A61

Brittain, S. D., Carr, J. S., Najita, J. R., Quanz, S. P., & Meyer, M. R. 2014, ApJ, 791, 136

Brittain, S. D., Najita, J. R., & Carr, J. S. 2009, ApJ, 702, 85

Brittain, S. D., Najita, J. R., Carr, J. S., et al. 2013, ApJ, 767, 159

Brogi, M., de Kok, R. J., Albrecht, S., et al. 2016, ApJ, 817, 106

Brogi, M., Snellen, I. A. G., de Kok, R. J., et al. 2012, Nature, 486, 502

Bromm, V. & Larson, R. B. 2004, ARAA, 42, 79

Bromm, V., Yoshida, N., Hernquist, L., & McKee, C. F. 2009, Nature, 459, 49

Brown, J. M., Pontoppidan, K. M., van Dishoeck, E. F., et al. 2013, ApJ, 770, 94

Brown, M. E. 2008, The Largest Kuiper Belt Objects, ed. M. A. Barucci, H. Boehnhardt, D. P. Cruikshank, A. Morbidelli, & R. Dotson, 335–344

Bruderer, S., Harsono, D., & van Dishoeck, E. F. 2015, A&A, 575, A94

Bruderer, S., van der Marel, N., van Dishoeck, E. F., & van Kempen, T. A. 2014, A&A, 562, A26

Bruderer, S., van Dishoeck, E. F., Doty, S. D., & Herczeg, G. J. 2012, A&A, 541, A91

Bujarrabal, V., Castro-Carrizo, A., Alcolea, J., & Van Winckel, H. 2015, A&A, 575, L7

Bujarrabal, V., Castro-Carrizo, A., Alcolea, J., et al. 2013, A&A, 557, L11

Bujarrabal, V., Castro-Carrizo, A., Winckel, H. V., et al. 2018, A&A, 614, A58

Burtscher, L., Hönig, S., Jaffe, W., et al. 2016, in Proc. SPIE, Vol. 9907, Society of Photo-Optical Instrumentation Engineers (SPIE) Conference Series, 99070R

Burtscher, L., Meisenheimer, K., Tristram, K. R. W., et al. 2013, A&A, 558

Canup, R. M. & Ward, W. R. 2002, AJ, 124, 3404

Canup, R. M. & Ward, W. R. 2009, Origin of Europa and the Galilean Satellites, ed. R. T. Pappalardo, W. B. McKinnon, & K. K. Khurana, 59

Caratti o Garatti, A., Stecklum, B., Weigelt, G., et al. 2016, A&A, 589, L4

Carney, M. T., Hogerheijde, M. R., Loomis, R. A., et al. 2017, A&A, 605, A21

Casassus, S., van der Plas, G., M, S. P., et al. 2013, Nature, 493, 191

Chapman, J. W., Zellem, R. T., Line, M. R., et al. 2017, PASP, 129, 104402

Charbonneau, D., Brown, T. M., Noyes, R. W., & Gilliland, R. L. 2002, ApJ, 568, 377

Chatterjee, S., Ford, E. B., Matsumura, S., & Rasio, F. A. 2008, ApJ, 686, 580

Cheng, Y., Tan, J. C., Liu, M., et al. 2018, ApJ, 853, 160

Cherchneff, I. 2012, A&A, 545, A12

Chiar, J. E., Adamson, A. J., Pendleton, Y. J., et al. 2002, ApJ, 570, 198

Chiar, J. E., Tielens, A. G. G. M., Whittet, D. C. B., et al. 2000, ApJ, 537, 749

Cid Fernandes, R., Gu, Q., Melnick, J., et al. 2004, MNRAS, 355, 273

Ciesla, F. J. & Cuzzi, J. N. 2006, Icarus, 181, 178

Clayton, R. N., Grossman, L., & Mayeda, T. K. 1973, Science, 182, 485

Cochran, A. L., Levasseur-Regourd, A.-C., Cordiner, M., et al. 2015, Space Science Reviews, 197, 9

Conroy, C., Dutton, A. A., Graves, G. J., Mendel, J. T., & van Dokkum, P. G. 2013, ApJL, 776, L26

Cridland, A. J., Eistrup, C., & van Dishoeck, E. F. 2019, arXiv e-prints [[arXiv]1901.08896]

Crossfield, I. J. M. 2014, A&A, 566, A130

Crossfield, I. J. M., Biller, B., Schlieder, J. E., et al. 2014, Nature, 505, 654

Cugno, G., Quanz, S. P., Hunziker, S., et al. 2019, A&A, 622, A156

Cyganowski, C. J., Brogan, C. L., Hunter, T. R., et al. 2017, MNRAS, 468, 3694

Czerny, B. & Hryniewicz, K. 2011, A&A, 525, L8+

Dale, J. E., Haworth, T. J., & Bressert, E. 2015, MNRAS, 450, 1199

Danielski, C., Baudino, J.-L., Lagage, P.-O., et al. 2018, AJ, 156, 276

Davies, B., Lumsden, S. L., Hoare, M. G., Oudmaijer, R. D., & de Wit, W.-J. 2010, MNRAS, 402, 1504

Davies, R. I., Mueller Sánchez, F., Genzel, R., et al. 2007, ApJ, 671, 1388

Dawson, R. I. & Johnson, J. A. 2018, ARA&A, 56, 175

de Juan Ovelar, M., Min, M., Dominik, C., et al. 2013, A&A, 560, A111

de Kok, R. J., Brogi, M., Snellen, I. A. G., et al. 2013, A&A, 554, A82

De Marco, O. 2009, PASP, 121, 316

De Marco, O. & Izzard, R. G. 2017, PASA, 34, e001

de Pater, I., Fletcher, L. N., Luszcz-Cook, S., et al. 2014, Icarus, 237, 211

de Ruyter, S., van Winckel, H., Dominik, C., Waters, L. B. F. M., & Dejonghe, H. 2005, A&A, 435, 161

de Ruyter, S., van Winckel, H., Maas, T., et al. 2006, A&A, 448, 641

de Wit, W. J., Hoare, M. G., Oudmaijer, R. D., et al. 2011, A&A, 526, L5

de Zeeuw, P. T., Hoogerwerf, R., de Bruijne, J. H. J., Brown, A. G. A., & Blaauw, A. 1999, AJ, 117, 354

Decin, L., Blomme, L., Reyniers, M., et al. 2008, A&A, 484, 401

Decin, L., De Beck, E., Brünken, S., et al. 2010, A&A, 516, A69

Decin, L., Hony, S., de Koter, A., et al. 2007, A&A, 475, 233

Decin, L., Richards, A. M. S., Waters, L. B. F. M., et al. 2017, A&A, 608, A55

Defrère, D., Absil, O., den Hartog, R., Hanot, C., & Stark, C. 2010, A&A, 509, A9

Defrère, D., Stark, C., Cahoy, K., & Beerer, I. 2012, in Proc. SPIE, Vol. 8442, Space Telescopes and Instrumentation 2012: Optical, Infrared, and Millimeter Wave, 84420M

Delbo, M., Mueller, M., Emery, J. P., Rozitis, B., & Capria, M. T. 2015, Asteroid Thermophysical Modeling, ed. P. Michel, F. E. DeMeo, & W. F. Bottke, 107–128

Deming, D., Seager, S., Richardson, L. J., & Harrington, J. 2005, Nature, 434, 740

Dong, S., Katz, B., & Socrates, A. 2013, ApJL, 762, L26

Dong, S., Katz, B., & Socrates, A. 2014, ApJ, 781, L5

Dressing, C. D. & Charbonneau, D. 2015, ApJ, 807, 45

Drew, J. E., Proga, D., & Stone, J. M. 1998, MNRAS, 296, L6

Du, F., Bergin, E. A., Hogerheijde, M., et al. 2017, ApJ, 842, 98

Duchêne, G. & Kraus, A. 2013, ARA&A, 51, 269

Dumusque, X., Pepe, F., Lovis, C., et al. 2012, Nature, 491, 207

Dunne, L., Eales, S., Ivison, R., Morgan, H., & Edmunds, M. 2003, Nature, 424, 285

Eckart, A., Baganoff, F. K., Schödel, R., et al. 2006a, A&A, 450, 535

Eckart, A., Baganoff, F. K., Zamaninasab, M., et al. 2008, A&A, 479, 625

Eckart, A. & Genzel, R. 1997, in Bulletin of the American Astronomical Society, Vol. 29, American Astro-nomical Society Meeting Abstracts, 1366

Eckart, A., Horrobin, M., Britzen, S., et al. 2014, in IAU Symposium, Vol. 303, The Galactic Center: Feeding and Feedback in a Normal Galactic Nucleus, ed. L. O. Sjouwerman, C. C. Lang, & J. Ott, 269–273

Eckart, A., Hüttemann, A., Kiefer, C., et al. 2017, Foundations of Physics, 47, 553

Eckart, A., Mužić, K., Yazici, S., et al. 2013, A&A, 551, A18

Eckart, A., Schödel, R., Meyer, L., et al. 2006b, A&A, 455, 1

Eckart, A., Schödel, R., Moultaka, J., et al. 2005, in American Institute of Physics Conference Series, Vol. 783, The Evolution of Starbursts, ed. S. Hüttmeister, E. Manthey, D. Bomans, & K. Weis, 17–25

Eckart, A., Zajacek, M., Parsa, M., et al. 2018, arXiv e-prints [[arXiv]1806.00284]

Eisner, J. A. 2015, ApJ, 803, L4

Eistrup, C., Walsh, C., & van Dishoeck, E. F. 2018, A&A, 613, A14

Elmegreen, B. G. 2002, ApJ, 577, 206

Ertel, S., Defrère, D., Hinz, P., et al. 2018a, AJ, 155, 194

Ertel, S., Kennedy, G. M., Defrère, D., et al. 2018b, in Society of Photo-Optical Instrumentation Engineers (SPIE) Conference Series, Vol. 10698, Space Telescopes and Instrumentation 2018: Optical, Infrared, and Millimeter Wave, 106981V

Esquej, P., Alonso-Herrero, A., González-Martín, O., et al. 2014a, ApJ, 780, 86

Esquej, P., Alonso-Herrero, A., González-Martín, O., et al. 2014b, ApJ, 780, 86

Fedele, D., Bruderer, S., van Dishoeck, E. F., et al. 2012, A&A, 544, L9

Fedele, D., Tazzari, M., Booth, R., et al. 2018, A&A, 610, A24

Feng, F., Tuomi, M., & Jones, H. R. A. 2018, arXiv e-prints [[arXiv]1803.08163]

Ferrarese, L. & Merritt, D. 2000, ApJ, 539, L9

Feuchtgruber, H., Helmich, F. P., van Dishoeck, E. F., & Wright, C. M. 2000, ApJl, 535, L111

Flowers, E., Brogi, M., Rauscher, E., M-R Kempton, E., & Chiavassa, A. 2018, arXiv e-prints [[arXiv]1810.06099]

Follette, K. B., Grady, C. A., Swearingen, J. R., et al. 2015, ApJ, 798, 132

Fortney, J. J., Marley, M. S., Saumon, D., & Lodders, K. 2008, ApJ, 683, 1104

Fouchet, L. & Mayer, L. 2008, arXiv e-prints [[arXiv]0806.3975]

Fry, P. M., Sromovsky, L. A., de Pater, I., Hammel, H. B., & Rages, K. A. 2012, The Astronomical Journal, 143, 150

Fujiwara, H., Ishihara, D., Onaka, T., et al. 2013, A&A, 550, A45

Gail, H.-P. 1998, A&A, 332, 1099

Galliano, E., Alloin, D., Pantin, E., et al. 2008, A&A, 492, 3

García-Burillo, S., Combes, F., Ramos Almeida, C., et al. 2016, ApJ, 823, L12

Garufi, A., Quanz, S. P., Avenhaus, H., et al. 2013, A&A, 560, A105

Garufi, A., Quanz, S. P., Schmid, H. M., et al. 2016, A&A, 588, A8

Geballe, T. R. 1986, A&A, 162, 248

Geballe, T. R., Mason, R. E., Rodríguez-Ardila, A., & Axon, D. J. 2009, ApJ, 701, 1710

Gebhardt, K., Kormendy, J., Ho, L. C., et al. 2000, ApJ, 543, L5

Geers, V. C., Augereau, J.-C., Pontoppidan, K. M., et al. 2006, A&A, 459, 545

Geers, V. C., Pontoppidan, K. M., van Dishoeck, E. F., et al. 2007a, A&A, 469, L35

Geers, V. C., van Dishoeck, E. F., Visser, R., et al. 2007b, A&A, 476, 279

Genzel, R., Eisenhauer, F., & Gillessen, S. 2010, Reviews of Modern Physics, 82, 3121

Genzel, R., Schödel, R., Ott, T., et al. 2003, Nature, 425, 934

Ghez, A. M., Klein, B. L., Morris, M., & Becklin, E. E. 1998, ApJ, 509, 678

Gielen, C., Bouwman, J., van Winckel, H., et al. 2011, A&A, 533, A99

Gielen, C., van Winckel, H., Min, M., Waters, L. B. F. M., & Lloyd Evans, T. 2008, A&A, 490, 725

Gielen, C., van Winckel, H., Waters, L. B. F. M., Min, M., & Dominik, C. 2007, A&A, 475, 629

Gillessen, S., Genzel, R., Fritz, T. K., et al. 2012, Nature, 481, 51

Gillon, M., Triaud, A. H. M. J., Demory, B.-O., et al. 2017, Nature, 542, 456

Giridhar, S., Lambert, D. L., Reddy, B. E., Gonzalez, G., & Yong, D. 2005, ApJ, 627, 432

Gobrecht, D. 2018, IAU 343, invited review [[IAU343]1809.10583]

Gobrecht, D., Cherchneff, I., & Sarangi, A. 2015, in Astronomical Society of the Pacific Conference Series, Vol. 497, Why Galaxies Care about AGB Stars III: A Closer Look in Space and Time, ed. F. Kerschbaum, R. F. Wing, & J. Hron, 321

Gordon, K. D., Meixner, M., Meade, M. R., et al. 2011, AJ, 142, 102

Gorlova, N., Van Winckel, H., Gielen, C., et al. 2012, A&A, 542, A27

Gorlova, N., Van Winckel, H., Ikonnikova, N. P., et al. 2015, MNRAS, 451, 2462

Goto, M., Usuda, T., Dullemond, C. P., et al. 2006a, ApJ, 652, 758

Goto, M., Usuda, T., Dullemond, C. P., et al. 2006b, ApJ, 652, 758

Gravity Collaboration, Abuter, R., Accardo, M., et al. 2017, A&A, 602, A94

Gravity Collaboration, Abuter, R., Amorim, A., et al. 2018, A&A, 618, L10

Guidi, G., Ruane, G., Williams, J. P., et al. 2018, MNRAS, 479, 1505

Habing, H. J. & Olofsson, H., eds. 2003, Asymptotic giant branch stars

Harker, D. E. & Desch, S. J. 2002, ApJ, 565, L109

Harker, D. E., Woodward, C. E., & Wooden, D. H. 2005, Science, 310, 278

Harsono, D., Bjerkeli, P., van der Wiel, M. H. D., et al. 2018, Nature Astronomy, 2, 646

Hartmann, L., Ciesla, F., Gressel, O., & Alexander, R. 2017, Space Sci. Rev., 212, 813

Hatzes, A. P. 2016, Space Sci. Rev., 205, 267

Haubois, X., Dodds-Eden, K., Weiss, A., et al. 2012, A&A, 540, A41

Hawker, G. A., Madhusudhan, N., Cabot, S. H. C., & Gandhi, S. 2018, ApJl, 863, L11

Hayward, C. C., Narayanan, D., Kereš, D., et al. 2013, MNRAS, 428, 2529

Helling, C., Woitke, P., Rimmer, P. B., et al. 2014, Life, 4 [[arXiv]1403.4420]

Herczeg, G. J., Brown, J. M., van Dishoeck, E. F., & Pontoppidan, K. M. 2011, A&A, 533, A112

Hicks, E. K. S., Davies, R. I., Maciejewski, W., et al. 2013, ApJ, 768, 107

Hicks, E. K. S., Davies, R. I., Malkan, M. A., et al. 2009, ApJ, 696, 448

Hillen, M., de Vries, B. L., Menu, J., et al. 2015, A&A, 578, A40

Hillen, M., Menu, J., Van Winckel, H., et al. 2014, A&A, 568, A12

Hillen, M., Van Winckel, H., Menu, J., et al. 2017, A&A, 599, A41

Hillen, M., Verhoelst, T., Van Winckel, H., et al. 2013, A&A, 559, A111

Hinkle, K. H., Brittain, S. D., & Lambert, D. L. 2007, ApJ, 664, 501

Hoeijmakers, H. J., Ehrenreich, D., Heng, K., et al. 2018a, Nature, 560, 453

Hoeijmakers, H. J., Schwarz, H., Snellen, I. A. G., et al. 2018b, A&A, 617, A144

Höfner, S. 2008, A&A, 491, L1

Hogerheijde, M. R., Bergin, E. A., Brinch, C., et al. 2011, Science, 334, 338

Homan, W., Richards, A., Decin, L., et al. 2017, A&A, 601, A5

Honda, M., Inoue, A. K., Fukagawa, M., et al. 2009, ApJ, 690, L110

Hönig, S. F., Kishimoto, M., Gandhi, P., et al. 2010, A&A, 515, A23+

Hopkins, P. F., Bundy, K., Croton, D., et al. 2010, ApJ, 715, 202

Hosek, Jr., M. W., Lu, J. R., Anderson, J., et al. 2019, ApJ, 870, 44

Hosokawa, T., Yorke, H. W., & Omukai, K. 2010, ApJ, 721, 478

Hron, J., Uttenthaler, S., Aringer, B., et al. 2015, A&A, 584, A27

Hsu, D. C., Ford, E. B., Ragozzine, D., & Morehead, R. C. 2018, AJ, 155, 205

Huélamo, N., Chauvin, G., Schmid, H. M., et al. 2018, A&A, 613, L5

Hughes, A. M., Duchêne, G., & Matthews, B. C. 2018, ARA&A, 56, 541

Ilee, J. D., Cyganowski, C. J., Nazari, P., et al. 2016, MNRAS, 462, 4386

Ilee, J. D., Wheelwright, H. E., Oudmaijer, R. D., et al. 2013, MNRAS, 429, 2960

Indebetouw, R., Whitney, B. A., Johnson, K. E., & Wood, K. 2006, ApJ, 636, 362

Jackson, A. P., Wyatt, M. C., Bonsor, A., & Veras, D. 2014, MNRAS, 440, 3757

Jensen, J. J., Hönig, S. F., Rakshit, S., et al. 2017, MNRAS, 470, 3071

Johansen, A. & Lambrechts, M. 2017, Annual Review of Earth and Planetary Sciences, 45, 359

Johnston, K. G., Robitaille, T. P., Beuther, H., et al. 2015, ApJL, 813, L19

Kamath, D., Wood, P. R., & Van Winckel, H. 2014, MNRAS, 439, 2211

Kamath, D., Wood, P. R., & Van Winckel, H. 2015, MNRAS, 454, 1468

Kamath, D., Wood, P. R., Van Winckel, H., & Nie, J. D. 2016, A&A, 586, L5

Kamiński, T. 2018, arXiv e-prints [[arXiv]1809.10583]

Kammerer, J. & Quanz, S. P. 2018, A&A, 609, A4

Kane, S. R., Wittenmyer, R. A., Hinkel, N. R., et al. 2016, ApJ, 821, 65

Kasper, M., Arsenault, R., Käufl, H.-U., et al. 2017, The Messenger, 169, 16

Kawahara, H., Murakami, N., Matsuo, T., & Kotani, T. 2014, ApJS, 212, 27

Kemper, F., Vriend, W. J., & Tielens, A. G. G. M. 2004, ApJ, 609, 826

Keppler, M., Benisty, M., Müller, A., et al. 2018, A&A, 617, A44

Kervella, P., Homan, W., Richards, A. M. S., et al. 2016, A&A, 596, A92

Kessler-Silacci, J. E., Dullemond, C. P., Augereau, J.-C., et al. 2007, ApJ, 659, 680

Kluska, J., Hillen, M., Van Winckel, H., et al. 2018, A&A, 616, A153

Kobayashi, C. 2018, IAU 343, invited review [[IAU343]1809.10583]

Kraus, A. L. & Ireland, M. J. 2012, ApJ, 745, 5

Kraus, A. L., Ireland, M. J., Cieza, L. A., et al. 2014, ApJ, 781, 20

Kraus, A. L., Ireland, M. J., Huber, D., Mann, A. W., & Dupuy, T. J. 2016, AJ, 152, 8

Kraus, S., Hofmann, K.-H., Menten, K. M., et al. 2010, Nature, 466, 339

Kraus, S., Kluska, J., Kreplin, A., et al. 2017, ApJL, 835, L5

Kreidberg, L., Bean, J. L., Désert, J.-M., et al. 2014, Nature, 505, 69

Krumholz, M. R., Klein, R. I., & McKee, C. F. 2007, ApJ, 665, 478

Kuiper, R., Klahr, H., Beuther, H., & Henning, T. 2010, ApJ, 722, 1556

Kuiper, R., Klahr, H., Beuther, H., & Henning, T. 2011, ApJ, 732, 20

Lacey, C. G., Baugh, C. M., Frenk, C. S., et al. 2008, MNRAS, 385, 1155

Lagadec, E. 2018, IAU 343, invited review

Lagadec, E., Verhoelst, T., Mékarnia, D., et al. 2011, MNRAS, 417, 32

Lagage, P.-O., Doucet, C., Pantin, E., et al. 2006, Science, 314, 621

Lang, C. C., Goss, W. M., & Morris, M. 2001, AJ, 121, 2681

Lang, C. C., Goss, W. M., & Wood, O. S. 1997, ApJ, 474, 275

Langton, J. & Laughlin, G. 2008, ApJ, 674, 1106

Lawler, S. M., Beichman, C. A., Bryden, G., et al. 2009, ApJ, 705, 89

Lawler, S. M. & Gladman, B. 2012, ApJ, 752, 53

Lebreton, J., Beichman, C., Bryden, G., et al. 2016a, ApJ, 817, 165

Lebreton, J., Beichman, C., Bryden, G., et al. 2016b, ApJ, 817, 165

Lee, E. J. & Chiang, E. 2015, ApJ, 811, 41

Lee, J.-M., Heng, K., & Irwin, P. G. J. 2013, ApJ, 778, 97

Lellouch, E., Moreno, R., & Paubert, G. 2005, Astronomy and Astrophysics, 430, L37

Lilly, S. J., Carollo, C. M., Pipino, A., Renzini, A., & Peng, Y. 2013, ApJ, 772, 119

Linz, H., Henning, T., Feldt, M., et al. 2009, A&A, 505, 655

Lissauer, J. J. 1993, ARA&A, 31, 129

Lisse, C. M., Chen, C. H., Wyatt, M. C., et al. 2009, ApJ, 701, 2019

Liu, W. M., Hinz, P. M., Meyer, M. R., et al. 2003, ApJ, 598, L111

López-Gonzaga, N., Burtscher, L., Tristram, K. R. W., Meisenheimer, K., & Schartmann, M. 2016, A&A, 591, A47

López-Gonzaga, N., Jaffe, W., Burtscher, L., Tristram, K. R. W., & Meisenheimer, K. 2014, A&A, 565, A71

Lovis, C., Snellen, I., Mouillet, D., et al. 2016, ArXiv e-prints [[arXiv]1609.03082]

Lumsden, S. L., Hoare, M. G., Urquhart, J. S., et al. 2013, ApJs, 208, 11

Lumsden, S. L., Wheelwright, H. E., Hoare, M. G., Oudmaijer, R. D., & Drew, J. E. 2012, MNRAS, 424, 1088

Lund, K. & Bonnell, I. A. 2018, MNRAS, 479, 2235

Lutz, D., Maiolino, R., Moorwood, A. F. M., et al. 2002, A&A, 396, 439

Lyons, J. R. & Young, E. D. 2005, Nature, 435, 317

Lyra, W. & Klahr, H. 2011, A&A, 527, A138

Maas, T., Van Winckel, H., & Lloyd Evans, T. 2005, A&A, 429, 297

Maaskant, K. M., Min, M., Waters, L. B. F. M., & Tielens, A. G. G. M. 2014, A&A, 563, A78

Madau, P. & Dickinson, M. 2014, ARA&A, 52, 415

Madhusudhan, N., Crouzet, N., McCullough, P. R., Deming, D., & Hedges, C. 2014, ApJ, 791, L9

Maercker, M., Mohamed, S., Vlemmings, W. H. T., et al. 2012, Nature, 490, 232

Malfait, K., Waelkens, C., Waters, L. B. F. M., et al. 1998, A&A, 332, L25

Mamajek, E. E. & Meyer, M. R. 2007, ApJ, 668, L175

Manara, C. F., Morbidelli, A., & Guillot, T. 2018, A&A, 618, L3

Mandell, A. M., Bast, J., van Dishoeck, E. F., et al. 2012, ApJ, 747, 92

Mangold, N., Baratoux, D., Witasse, O., Encrenaz, T., & Sotin, C. 2016, The Astronomy and Astrophysics
    Review, 24, 15

Matthews, B. C., Krivov, A. V., Wyatt, M. C., Bryden, G., & Eiroa, C. 2014, Protostars and Planets VI, 521

Mawet, D., Hirsch, L., Lee, E. J., et al. 2018, arXiv e-prints [[arXiv]1810.03794]

Mayne, N. J., Baraffe, I., Acreman, D. M., et al. 2014, A&A, 561, A1

McClure, M. K., Espaillat, C., Calvet, N., et al. 2015, ApJ, 799, 162

McCoy, M., Ott, J., Meier, D. S., et al. 2017, ApJ, 851, 76

McKee, C. F. & Tan, J. C. 2003, ApJ, 585, 850

Meech, K. J., Weryk, R., Micheli, M., et al. 2017, Nature, 552, 378

Meixner, M., Gordon, K. D., Indebetouw, R., et al. 2006, AJ, 132, 2268

Melia, F. & Falcke, H. 2001, ARAA, 39, 309

Mennesson, B., Millan-Gabet, R., Serabyn, E., et al. 2014, ApJ, 797, 119

Meyer, D. M.-A., Kuiper, R., Kley, W., Johnston, K. G., & Vorobyov, E. 2018, MNRAS, 473, 3615

Meyer, L., Do, T., Ghez, A., et al. 2008a, ApJL, 688, L17

Meyer, L., Eckart, A., Schödel, R., et al. 2006a, A&A, 460, 15

Meyer, L., Schödel, R., Eckart, A., et al. 2006b, A&A, 458, L25

Meyer, M. R., Carpenter, J. M., Mamajek, E. E., et al. 2008b, ApJ, 673, L181

Millan-Gabet, R., Serabyn, E., Mennesson, B., et al. 2011, ApJ, 734, 67

Miller-Ricci, E., Meyer, M. R., Seager, S., & Elkins-Tanton, L. 2009, ApJ, 704, 770

Min, M., Bouwman, J., Dominik, C., et al. 2016, A&A, 593, A11

Min, M., Waters, L. B. F. M., de Koter, A., et al. 2007, A&A, 462, 667

Miotello, A., Bruderer, S., & van Dishoeck, E. F. 2014, A&A, 572, A96

Mollière, P. & Snellen, I. A. G. 2018, arXiv e-prints [[arXiv]1809.01156]

Moneti, A., Cernicharo, J., & Pardo, J. R. 2001, ApJl, 549, L203

Moore, T. J. T., Bretherton, D. E., Fujiyoshi, T., et al. 2007, MNRAS, 379, 663

Morales, F. Y., Padgett, D. L., Bryden, G., Werner, M. W., & Furlan, E. 2012, ApJ, 757, 7

Morbidelli, A., Levison, H. F., & Gomes, R. 2008, The Dynamical Structure of the Kuiper Belt and Its Primordial Origin, ed. M. A. Barucci, H. Boehnhardt, D. P. Cruikshank, A. Morbidelli, & R. Dotson, 275–292

Morbidelli, A., Lunine, J. I., O'Brien, D. P., Raymond, S. N., & Walsh, K. J. 2012, Annual Review of Earth and Planetary Sciences, 40, 251

Morbidelli, A., Szulágyi, J., Crida, A., et al. 2014, Icarus, 232, 266

Mordasini, C. 2018, Planetary Population Synthesis, 143

Mordasini, C., van Boekel, R., Mollière, P., Henning, T., & Benneke, B. 2016, ApJ, 832, 41

Mori, T. I., Imanishi, M., Alonso-Herrero, A., et al. 2014, PASJ, 66, 93

Morley, C. V., Kreidberg, L., Rustamkulov, Z., Robinson, T., & Fortney, J. J. 2017, ApJ, 850, 121

Morris, M. & Yusef-Zadeh, F. 1989, ApJ, 343, 703

Moser, L., Sánchez-Monge, Á., Eckart, A., et al. 2017, A&A, 603, A68

Mosqueira, I. & Estrada, P. R. 2003, Icarus, 163, 198

Mossoux, E. & Eckart, A. 2018, MNRAS, 474, 3787

Moultaka, J., Eckart, A., & Sabha, N. 2015, MNRAS, 448, 3363

Moultaka, J., Eckart, A., Schödel, R., Viehmann, T., & Najarro, F. 2005, A&A, 443, 163

Moultaka, J., Eckart, A., Viehmann, T., et al. 2004, A&A, 425, 529

Moultaka, J., Eckart, A., Viehmann, T., & Schödel, R. 2006, in Journal of Physics Conference Series, Vol. 54, Journal of Physics Conference Series, ed. R. Schödel, G. C. Bower, M. P. Muno, S. Nayakshin, & T. Ott, 57–61

Mousis, O., Atkinson, D. H., Cavalié, T., et al. 2018, Planetary and Space Science, 155, 12

Movsessian, T. A., Magakian, T. Y., & Moiseev, A. V. 2012, A&A, 541, A16

Mulders, G. D., Min, M., Dominik, C., Debes, J. H., & Schneider, G. 2013, A&A, 549, A112

Mulders, G. D., Waters, L. B. F. M., Dominik, C., et al. 2011, A&A, 531, A93

Müller, A., Keppler, M., Henning, T., et al. 2018, A&A, 617, L2

Muller, S., Dinh-V-Trung, He, J.-H., & Lim, J. 2008, ApJ, 684, L33

Müller, T. G., Sekiguchi, T., Kaasalainen, M., Abe, M., & Hasegawa, S. 2005, Astronomy and Astrophysics, 443, 347

Müller-Sánchez, F., Davies, R. I., Genzel, R., et al. 2009, ApJ, 691, 749

Mumma, M. J. & Charnley, S. B. 2011, Annual Review of Astronomy and Astrophysics, 49, 471

Murakawa, K., Lumsden, S. L., Oudmaijer, R. D., et al. 2013, MNRAS, 436, 511

Murray, N., Quataert, E., & Thompson, T. A. 2005, ApJ, 618, 569

Muto, T., Grady, C. A., Hashimoto, J., et al. 2012, ApJ, 748, L22

Mužić, K., Eckart, A., Schödel, R., Meyer, L., & Zensus, A. 2007, A&A, 469, 993

Mužić, K., Schödel, R., Eckart, A., Meyer, L., & Zensus, A. 2008, A&A, 482, 173

Najita, J., Carr, J. S., & Mathieu, R. D. 2003, ApJ, 589, 931

Neumayer, N., Cappellari, M., Reunanen, J., et al. 2007, ApJ, 671, 1329

Nishiyama, S. & Schödel, R. 2013, A&A, 549, A57

Norris, B. R. M., Tuthill, P. G., Ireland, M. J., et al. 2012, Nature, 484, 220

Nortmann, L., Pallé, E., Salz, M., et al. 2018, Science, 362, 1388

Nowotny, W., Aringer, B., Höfner, S., Gautschy-Loidl, R., & Windsteig, W. 2005, A&A, 437, 273

Nugroho, S. K., Kawahara, H., Masuda, K., et al. 2017, AJ, 154, 221

Öberg, K. I., Murray-Clay, R., & Bergin, E. A. 2011, ApJL, 743, L16

Ohnaka, K. 2014, A&A, 561, A47

Oliveira, I., Olofsson, J., Pontoppidan, K. M., et al. 2011, ApJ, 734, 51

Olofsson, J., Juhász, A., Henning, T., et al. 2012, A&A, 542, A90

Oomen, G.-M., Van Winckel, H., Pols, O., et al. 2018, A&A, 620, A85

Orton, G. S., Fletcher, L. N., Encrenaz, T., et al. 2015, Icarus, 260, 94

Paganini, L., Mumma, M. J., Gibb, E. L., & Villanueva, G. L. 2017, The Astrophysical Journal Letters, 836, L25

Panić, O., Ratzka, T., Mulders, G. D., et al. 2014, A&A, 562, A101

Parsa, M., Eckart, A., Shahzamanian, B., et al. 2017, ApJ, 845, 22

Pascucci, I., Herczeg, G., Carr, J. S., & Bruderer, S. 2013, ApJ, 779, 178

Pascucci, I. & Sterzik, M. 2009, ApJ, 702, 724

Patel, R. I., Metchev, S. A., & Heinze, A. 2014, ApJS, 212, 10

Perez, S., Dunhill, A., Casassus, S., et al. 2015, ApJ, 811, L5

Perger, M., Moultaka, J., Eckart, A., et al. 2008, A&A, 478, 127

Perrot, C., Baudoz, P., Boccaletti, A., et al. 2018, arXiv e-prints [[arXiv]1804.01371]

Petigura, E. A., Howard, A. W., & Marcy, G. W. 2013, Proceedings of the National Academy of Science, 110, 19273

Pfuhl, O., Gillessen, S., Eisenhauer, F., et al. 2015, ApJ, 798, 111

Pinilla, P., Birnstiel, T., Ricci, L., et al. 2012, A&A, 538, A114

Pinilla, P., Birnstiel, T., & Walsh, C. 2015a, A&A, 580, A105

Pinilla, P., Klarmann, L., Birnstiel, T., et al. 2016, A&A, 585, A35

Pinilla, P., Tazzari, M., Pascucci, I., et al. 2018, ApJ, 859, 32

Pinilla, P., van der Marel, N., Pérez, L. M., et al. 2015b, A&A, 584, A16

Pinilla, P. & Youdin, A. 2017, in Astrophysics and Space Science Library, Vol. 445, Astrophysics and Space
    Science Library, ed. M. Pessah & O. Gressel, 91

Pinte, C., Price, D. J., Ménard, F., et al. 2018, ApJ, 860, L13

Pollack, J. B., Hubickyj, O., Bodenheimer, P., et al. 1996, Icarus, 124, 62

Pomohaci, R., Oudmaijer, R. D., & Goodwin, S. P. 2019, MNRAS, 484, 226

Pomohaci, R., Oudmaijer, R. D., Lumsden, S. L., Hoare, M. G., & Mendigutía, I. 2017, MNRAS, 472,
    3624

Pontoppidan, K. M., Blake, G. A., & Smette, A. 2011a, ApJ, 733, 84

Pontoppidan, K. M., Blake, G. A., & Smette, A. 2011b, ApJ, 733, 84

Pontoppidan, K. M., Blake, G. A., van Dishoeck, E. F., et al. 2008, ApJ, 684, 1323

Pontoppidan, K. M., Salyk, C., Bergin, E. A., et al. 2014, Protostars and Planets VI, 363

Pontoppidan, K. M., Salyk, C., Blake, G. A., et al. 2010, ApJ, 720, 887

Prieto, M. A., Mezcua, M., Fernández-Ontiveros, J. A., & Schartmann, M. 2014, MNRAS, 442, 2145

Protopapa, S., Boehnhardt, H., Herbst, T. M., et al. 2008, Astronomy and Astrophysics, 490, 365

Qi, C., Öberg, K. I., Wilner, D. J., et al. 2013, Science, 341, 630

Quanz, S. P., Amara, A., Meyer, M. R., et al. 2015a, ApJ, 807, 64

Quanz, S. P., Amara, A., Meyer, M. R., et al. 2013, ApJ, 766, L1

Quanz, S. P., Crossfield, I., Meyer, M. R., Schmalzl, E., & Held, J. 2015b, International Journal of Astrobi-
    ology, 14, 279

Rajpaul, V., Aigrain, S., & Roberts, S. 2016, MNRAS, 456, L6

Rameau, J., Follette, K. B., Pueyo, L., et al. 2017, AJ, 153, 244

Ramos Almeida, C., Alonso-Herrero, A., Esquej, P., et al. 2014, MNRAS, 445, 1130

Ramos Almeida, C., Levenson, N. A., Alonso-Herrero, A., et al. 2011, ApJ, 731, 92

Ramstedt, S. 2018, IAU 343, invited review

Ramstedt, S., Mohamed, S., Vlemmings, W. H. T., et al. 2014, A&A, 570, L14

Rappaport, S., Levine, A., Chiang, E., et al. 2012, ApJ, 752, 1

Ratzka, T., Köhler, R., & Leinert, C. 2005, A&A, 437, 611

Ratzka, T., Schegerer, A. A., Leinert, C., et al. 2009, A&A, 502, 623

Regály, Z., Sándor, Z., Dullemond, C. P., & van Boekel, R. 2010, A&A, 523, A69

Reggiani, M., Christiaens, V., Absil, O., et al. 2018, A&A, 611, A74

Reggiani, M., Quanz, S. P., Meyer, M. R., et al. 2014, ApJ, 792, L23

Reid, M. J., Menten, K. M., Greenhill, L. J., & Chandler, C. J. 2007, ApJ, 664, 950

Riaud, P. & Schneider, J. 2007, A&A, 469, 355

Ribas, I., Bolmont, E., Selsis, F., et al. 2016, A&A, 596, A111

Ribas, I., Tuomi, M., Reiners, A., et al. 2018, Nature, 563, 365

Richardson, D. C., Leinhardt, Z. M., Melosh, H. J., Bottke, Jr., W. F., & Asphaug, E. 2002, Gravitational Aggregates: Evidence and Evolution, ed. W. F. Bottke, Jr., A. Cellino, P. Paolicchi, & R. P. Binzel, 501–515

Rizzuto, A. C., Ireland, M. J., & Robertson, J. G. 2011, MNRAS, 416, 3108

Roberge, A., Chen, C. H., Millan-Gabet, R., et al. 2012, PASP, 124, 799

Rosario, D. J., Togi, A., Burtscher, L., et al. 2019, ApJ (accepted)

Rosen, A. L., Krumholz, M. R., McKee, C. F., & Klein, R. I. 2016, MNRAS, 463, 2553

Rosotti, G. P., Juhasz, A., Booth, R. A., & Clarke, C. J. 2016, MNRAS, 459, 2790

Rowe, J. F., Coughlin, J. L., Antoci, V., et al. 2015, ApJS, 217, 16

Ryde, N., Lambert, J., Richter, M. J., et al. 2015, in Astronomical Society of the Pacific Conference Series, Vol. 497, Why Galaxies Care about AGB Stars III: A Closer Look in Space and Time, ed. F. Kerschbaum, R. F. Wing, & J. Hron, 67

Sahai, R., Morris, M. R., & Villar, G. G. 2011, AJ, 141, 134

Salyk, C., Blake, G. A., Boogert, A. C. A., & Brown, J. M. 2011, ApJ, 743, 112

Salyk, C., Pontoppidan, K., Corder, S., et al. 2014, ApJ, 792, 68

Salyk, C., Pontoppidan, K. M., Blake, G. A., et al. 2008, ApJ, 676, L49

Sana, H., de Mink, S. E., de Koter, A., et al. 2012, Science, 337, 444

Sánchez-Monge, Á., Cesaroni, R., Beltrán, M. T., et al. 2013, A&A, 552, L10

Sanhueza, P., Jackson, J. M., Zhang, Q., et al. 2017, ApJ, 841, 97

Sargent, B. A., Forrest, W. J., Tayrien, C., et al. 2009, ApJS, 182, 477

Sarzi, M., Allard, E. L., Knapen, J. H., & Mazzuca, L. M. 2007, MNRAS, 380, 949

Scharf, C. & Menou, K. 2009, ApJL, 693, L113

Schartmann, M., Ballone, A., Burkert, A., et al. 2015, ApJ, 811, 155

Schartmann, M., Wada, K., Prieto, M. A., Burkert, A., & Tristram, K. R. W. 2014, MNRAS, 445, 3878

Schaye, J., Crain, R. A., Bower, R. G., et al. 2015a, MNRAS, 446, 521

Schaye, J., Crain, R. A., Bower, R. G., et al. 2015b, MNRAS, 446, 521

Scheeres, D. J., Britt, D., Carry, B., & Holsapple, K. A. 2015, Asteroid Interiors and Morphology, ed. P. Michel, F. E. DeMeo, & W. F. Bottke, 745–766

Schegerer, A. A., Wolf, S., Hummel, C. A., Quanz, S. P., & Richichi, A. 2009, A&A, 502, 367

Schleicher, D. R. G. & Dreizler, S. 2014, A&A, 563, A61

Schödel, R., Eckart, A., Mužić, K., et al. 2007, A&A, 462, L1

Schödel, R., Morris, M. R., Muzic, K., et al. 2011, A&A, 532, A83

Schwarz, H., Ginski, C., de Kok, R. J., et al. 2016, A&A, 593, A74

Schworer, G., Lacour, S., Huélamo, N., et al. 2017, ApJ, 842, 77

Segura, A., Walkowicz, L. M., Meadows, V., Kasting, J., & Hawley, S. 2010, Astrobiology, 10, 751

Shahzamanian, B., Eckart, A., Zajaček, M., et al. 2016, A&A, 593, A131

Shepherd, D. S., Claussen, M. J., & Kurtz, S. E. 2001, Science, 292, 1513

Showman, A. P., Fortney, J. J., Lian, Y., et al. 2009, ApJ, 699, 564

Shuping, R. Y., Morris, M., & Bally, J. 2004, AJ, 128, 363

Sing, D. K., Fortney, J. J., Nikolov, N., et al. 2016, Nature, 529, 59

Skemer, A. J., Hinz, P. M., Esposito, S., et al. 2012, ApJ, 753, 14

Skemer, A. J., Marley, M. S., Hinz, P. M., et al. 2014, ApJ, 792, 17

Skemer, A. J., Morley, C. V., Zimmerman, N. T., et al. 2016, ApJ, 817, 166

Smith, N., Hinkle, K. H., & Ryde, N. 2009a, AJ, 137, 3558

Smith, R. L., Pontoppidan, K. M., Young, E. D., Morris, M. R., & van Dishoeck, E. F. 2009b, ApJ, 701, 163

Snellen, I., de Kok, R., Birkby, J. L., et al. 2015, A&A, 576, A59

Snellen, I. A. G., Brandl, B. R., de Kok, R. J., et al. 2014, Nature, 509, 63

Snellen, I. A. G. & Brown, A. G. A. 2018, Nature Astronomy, 2, 883

Snellen, I. A. G., de Kok, R. J., de Mooij, E. J. W., & Albrecht, S. 2010a, Nature, 465, 1049

Snellen, I. A. G., de Kok, R. J., de Mooij, E. J. W., & Albrecht, S. 2010b, Nature, 465, 1049

Socrates, A., Katz, B., Dong, S., & Tremaine, S. 2012, ApJL, 750, 106

Sozzetti, A., Giacobbe, P., Lattanzi, M. G., et al. 2014, MNRAS, 437, 497

Sparks, W. B. & Ford, H. C. 2002, ApJ, 578, 543

Speagle, J. S., Steinhardt, C. L., Capak, P. L., & Silverman, J. D. 2014, ApJS, 214, 15

Stolker, T., Dominik, C., Avenhaus, H., et al. 2016, A&A, 595, A113

Szulágyi, J., Morbidelli, A., Crida, A., & Masset, F. 2014, ApJ, 782, 65

Tan, J. C., Beltrán, M. T., Caselli, P., et al. 2014, Protostars and Planets VI, 149

Tan, J. C., Kong, S., Butler, M. J., Caselli, P., & Fontani, F. 2013, ApJ, 779, 96

Teague, R., Bae, J., Bergin, E. A., Birnstiel, T., & Foreman-Mackey, D. 2018, ApJ, 860, L12

Tenenbaum, E. D. & Ziurys, L. M. 2009, ApJ, 694, L59

Terada, H. & Tokunaga, A. T. 2017, ApJ, 834, 115

Terada, H., Tokunaga, A. T., Kobayashi, N., et al. 2007, ApJ, 667, 303

Testi, L., Skemer, A., Henning, T., et al. 2015, ApJ, 812, L38

Thalmann, C., Janson, M., Garufi, A., et al. 2016, ApJ, 828, L17

Thi, W. F., Kamp, I., Woitke, P., et al. 2013, A&A, 551, A49

Thiabaud, A., Marboeuf, U., Alibert, Y., Leya, I., & Mezger, K. 2015, A&A, 574, A138

Thompson, M. A., Urquhart, J. S., Moore, T. J. T., & Morgan, L. K. 2012, MNRAS, 421, 408

Tielens, A. G. G. M. 1990, in From Miras to Planetary Nebulae: Which Path for Stellar Evolution?, ed.
    M. O. Mennessier & A. Omont, 186–200

Todorov, K. O., Line, M. R., Pineda, J. E., et al. 2016, ApJ, 823, 14

Treu, T., Auger, M. W., Koopmans, L. V. E., et al. 2010, ApJ, 709, 1195

Turbet, M., Leconte, J., Selsis, F., et al. 2016, A&A, 596, A112

Tychoniec, Ł., Tobin, J. J., Karska, A., et al. 2018, ApJS, 238, 19

Valencia-S., M., Eckart, A., Zajaček, M., et al. 2015, ApJ, 800, 125

van Aarle, E., van Winckel, H., Lloyd Evans, T., et al. 2011, A&A, 530, A90

van Boekel, R., Min, M., Leinert, C., et al. 2004, Nature, 432, 479

van Boekel, R., Min, M., Waters, L. B. F. M., et al. 2005, A&A, 437, 189

van Boekel, R., Waters, L. B. F. M., Dominik, C., et al. 2003, A&A, 400, L21

van der Marel, N., van Dishoeck, E. F., Bruderer, S., et al. 2016, A&A, 585, A58

van der Marel, N., van Dishoeck, E. F., Bruderer, S., et al. 2013, Science, 340, 1199

van der Marel, N., Williams, J. P., Ansdell, M., et al. 2018, ApJ, 854, 177

van der Plas, G., van den Ancker, M. E., Waters, L. B. F. M., & Dominik, C. 2015, A&A, 574, A75

Van Winckel, H. 2003, ARA&A, 41, 391

Van Winckel, H. 2018, arXiv e-prints [[arXiv]1809.00871]

van Winckel, H., Lloyd Evans, T., Briquet, M., et al. 2009, A&A, 505, 1221

Vigan, A., Bonavita, M., Biller, B., et al. 2017, A&A, 603, A3

Villanueva, G. L., Mumma, M. J., Novak, R. E., et al. 2013, Icarus, 223, 11

Visser, R., Geers, V. C., Dullemond, C. P., et al. 2007, A&A, 466, 229

Visser, R., van Dishoeck, E. F., Doty, S. D., & Dullemond, C. P. 2009, A&A, 495, 881

Vollmer, B., Beckert, T., & Davies, R. I. 2008, A&A, 491, 441

Vollmer, B., Schartmann, M., Burtscher, L., et al. 2018, A&A, 615, A164

Wada, K., Schartmann, M., & Meijerink, R. 2016, ApJ, 828, L19

Waelkens, C., Waters, L. B. F. M., de Graauw, M. S., et al. 1996, A&A, 315, L245

Walsh, C., Juhász, A., Meeus, G., et al. 2016, ApJ, 831, 200

Wang, J. J., Graham, J. R., Dawson, R., et al. 2018, AJ, 156, 192

Wang, Z., Chakrabarty, D., & Kaplan, D. L. 2006, Nature, 440, 772

Wheelwright, H. E., Bjorkman, J. E., Oudmaijer, R. D., et al. 2012, MNRAS, 423, L11

Winn, J. N. & Fabrycky, D. C. 2015, ARA&A, 53, 409

Wirick, S., Flynn, G. J., Keller, L. P., et al. 2009, Meteoritics and Planetary Science, 44, 1611

Witzel, G., Eckart, A., Bremer, M., et al. 2012, ApJs, 203, 18

Witzel, G., Ghez, A. M., Morris, M. R., et al. 2014, ApJl, 796, L8

Witzel, G., Martinez, G., Hora, J., et al. 2018, ApJ, 863, 15

Woitke, P. 2006, A&A, 460, L9

Woitke, P., Kamp, I., & Thi, W.-F. 2009, A&A, 501, 383

Woitke, P., Min, M., Thi, W.-F., et al. 2018, A&A, 618 [[arXiv]1807.05784]

Wold, M., Lacy, M., Käufl, H. U., & Siebenmorgen, R. 2006, A&A, 460, 449

Wolszczan, A. & Frail, D. A. 1992, Nature, 355, 145

Wooden, D. H., Ishii, H. A., & Zolensky, M. E. 2017, Philosophical Transactions of the Royal Society of London Series A, 375, 20160260

Wyatt, M. C. 2008, ARA&A, 46, 339

Wyatt, M. C., Smith, R., Greaves, J. S., et al. 2007, ApJ, 658, 569

Yuan, F., Quataert, E., & Narayan, R. 2003, ApJ, 598, 301

Yuan, F., Quataert, E., & Narayan, R. 2004, ApJ, 606, 894

Yusef-Zadeh, F. & Morris, M. 1987, ApJ, 322, 721

Yusef-Zadeh, F., Morris, M., & Chance, D. 1984, Nature, 310, 557

Yusef-Zadeh, F., Wardle, M., Bushouse, H., Dowell, C. D., & Roberts, D. A. 2010, ApJl, 724, L9

Yvart, W., Cabrit, S., Pineau des Forêts, G., & Ferreira, J. 2016, A&A, 585, A74

Zajaček, M., Britzen, S., Eckart, A., et al. 2017, A&A, 602, A121

Zajaček, M., Eckart, A., Karas, V., et al. 2016, MNRAS, 455, 1257

Zajaček, M., Karas, V., & Eckart, A. 2014, A&A, 565, A17

Zhang, Q., Wang, K., Lu, X., & Jiménez-Serra, I. 2015, ApJ, 804, 141

Zhang, X., Liu, B., Lin, D. N. C., & Li, H. 2014, ApJ, 797, 20

Zhen, J., Castellanos, P., Paardekooper, D. M., et al. 2015, ApJ, 804, L7

Zhen, J., Castellanos, P., Paardekooper, D. M., Linnartz, H., & Tielens, A. G. G. M. 2014, ApJ, 797, L30

Zhu, Z. 2015, ApJ, 799, 16

Zhukovska, S., Dobbs, C., Jenkins, E. B., & Klessen, R. S. 2016, ApJ, 831, 147

Zinnecker, H. & Yorke, H. W. 2007, ARAA, 45, 481

Zurlo, A., Mesa, D., Desidera, S., et al. 2018, MNRAS, 480, 35